High-temperature interactions of molten Ti-Al, Ni-Al and Ni-B alloys with TiB_2 ceramic

Von der Fakultät Maschinenwesen der Technischen Universität Dresden

zur Erlangung des akademischen Grades

Doktoringenieur (Dr.-Ing.)

angenommene

DISSERTATION

von

Lixia Xi

geboren am 11. 05. 1987 in Shandong, China

TECHNISCHE UNIVERSITÄT DRESDEN

Leibniz-Institut für Festkörper- und Werkstoffforschung Dresden

Tag der Einreichung: 03 November, 2016

Tag der Verteidigung: 08 März, 2017

1. Gutachter: Prof. Dr. Jürgen Eckert

2. Gutachter: Prof. Rajiv Asthana

Abstract

Investigations of high-temperature wetting and interfacial interactions in liquid metal/transition-metal diboride systems are driven by technological demand in obtaining high-quality metal matrix composites and reliable joining of ultrahigh-temperature ceramics for aggressive chemical and/or thermal environments. The physical and chemical characteristics of metal/ceramic interface (e.g. wetting kinetics, interfacial reactions and phase formation) are indispensable for understanding the fundamental mechanisms, controlling technological parameters, and defining the properties and quality of final products.

The sessile drop method is the most commonly used for quantitative characterization of the wetting properties and direct investigations of the interfacial interactions between a liquid metal and a solid substrate with the help of microscopy. This thesis is focused on the high-temperature wetting and interfacial interactions of molten pure Al and Ti-Al, Ni-Al and Ni-B alloys with TiB_2 ultra-high-temperature ceramic. The metal/ceramic couples after the sessile drop tests are mainly characterized using scanning electron microscopy coupled with energy dispersive X-ray spectroscopy and X-ray diffraction.

The temperature- and time-dependent wetting between the liquid Al and TiB_2 ceramic over a wide temperature range was investigated using the classical sessile drop and dispensed drop techniques. The results showed that the wetting was significantly accelerated with increasing temperature. A difference of the wetting temperature by these two techniques was about 300 °C, due to the native oxide film present on the Al surface in the classical sessile drop tests. Starting from 1000 °C, liquid Al either filled the inter-grain pores or penetrated along the grain boundaries of the TiB_2 substrate but there was no reaction observed in the Al/TiB_2 system.

The interfacial interactions between Ti-Al melts and TiB_2 ceramic were studied by the classical sessile drop technique due to the absence of appropriate crucible for liquid Ti and Ti-containing melts. Pure Ti on TiB_2 exhibited an incipient melting at about 120 °C below its melting point in view of the shape and structure of the solidified Ti/TiB_2 couple. It was caused by the solid state diffusion of boron from the substrate into the Ti sample and a composition shift from pure Ti to a Ti-B alloy in the near-substrate region. In comparison to pure Ti, the role of Al in the penetration of Ti-Al melts along the grain boundaries in the ceramic seemed to be more important than that of temperature in this study.

The wetting and interfacial interactions between Ni-Al molten alloys and TiB_2 were investigated using the dispensed drop technique. Liquid Ni-Al alloys showed a strong dependence of the wetting behavior on the TiB_2 substrates, both on the alloy composition and testing conditions. It changed from a dissolutive, reactive wetting on the Ni-rich side to a non-reactive wetting on the Al-rich side. The results suggest that Ni content in Ni-Al alloys plays a major role in the changes of substrate dissolution and geometrical configuration at the metal/ceramic interface. To understand the effect of the Ni content on TiB_2 dissolution, the melting and wetting of $Ni_{83}B_{17}$ and $Ni_{50}B_{50}$ alloys on TiB_2 ceramic were investigated using the classical sessile drop technique in view of possible joining of TiB_2 ceramics. Based on the wetting tests, TiB_2 ceramics have been joined using $Ni_{50}B_{50}$ melt-spun ribbon as an interlayer.

The results obtained in this work provide a better understanding of the interaction mechanisms in between liquid Al, Ti-Al, Ni-Al and Ni-B alloys and TiB_2 ceramic and make basis for development of guidelines for the preparation of metal matrix composites and/or ceramic matrix composites and joining of TiB_2 ceramic parts for high-temperature structural applications.

Zusammenfassung

Untersuchungen der Hochtemperaturbenetzung und Grenzfächeninteraktionen in Flüssigmetall/Übergangsmetall-Diborid-Systemen werden durch die technologische Nachfrage nach qualitative hochwertigen Metall-Matrix-Kompositen und verläßlichen Verbindungen von Ultrahochtemperaturkeramiken für aggressive chemische und/oder thermische Umgebungen angetrieben. Die physikalischen und chemischen Charakteristika der Metall/Keramik-Grenzflächen (z.B. die Benetzungskinetik, Grenzflächenreaktionen und die Phasenbildung) sind unerläßlich um die fundamentalen Mechanismen, die kontrollierenden technologischen Parameter, sowie die definierenden Eigenschaften und die Qualität des Endprodukts zu verstehen.

Die Methode des liegenden Tropfens (engl. sessile drop method) ist die am häufigsten verwendete Verfahren für die quantitative Charakterisierung der Benetzungseigenschaften und für die direkte Untersuchung von Grenzflächeninteraktionen zwischen Flüssigmetall und festen Substraten unter Zuhilfenahme von Mikroskopie. Der Fokus dieser Arbeit liegt auf der Hochtemperaturbenetzung und den Grenzflächeninteraktionen von geschmolzenen reinem Al und Ti-Al, Ni-Al und Ni-B Schmelzen mit der TiB_2 Ultrahochtemperaturkeramik. Die über die Methode des liegenden Tropfens hergestellten Metall/Keramik Verbunde werden hauptsächlich mittels Rasterelektronenmikroskopie gekoppelt mit energiedispersiver Röntgenspektroskopie sowie Röntgenbeugung untersucht.

Die temperatur- und zeitabhängige Benetzung von flüssigem Al auf der TiB_2 Keramik wurde mittels der klassischen Technik des liegenden Tropfens und der sogenannten dispensed drop technique (engl.) über einen weiten Temperaturbereich untersucht. Die Ergebnisse zeigen, dass mit ansteigender Temperatur die Benetzung bedeutend schneller abläuft. Die beiden Methoden liefern einen Unterschied in der Benetzungstemperatur von etwa 300°C aufgrund der nativen Oxidschicht auf der Al-Oberfläche bei dem klassischen Sessile-drop Versuch. Beginnend bei 1000°C füllt das flüssige Al entweder die intergranularen Poren auf oder dringt entlang der Korngrenzen in das TiB_2 Substrat ein. Es wurde keine Reaktion im Al/TiB_2 System beobachtet.

Die Grenzflächeninteraktionen zwischen Ti-Al Schmelzen und der TiB_2 Keramik wurden mit der klassischen Technik des liegenden Tropfens untersucht, da ein passender Tiegel für flüssiges Ti und Ti-haltige Schmelzen nicht vorhanden war. Für reines Ti auf TiB_2 setzt das Schmelzen bei etwa 120 °C unter seinem Schmelzpunkt ein, wie aus Untersuchungen der Form und Struktur der erstarrten Ti/TiB_2 Proben hervorgeht. Dies wird durch Festkörperdiffusion von

B aus dem Substrat in die Ti Probe hinein und einer Verschiebung der Zusammensetzung von reinem Ti zu einer Ti-B Legierung in der substratnahen Region verursacht. Die Rolle von Al scheint für das Eindringen von Ti-Al Schmelzen entlang von Krongrenzen in das Keramiksubstrat von größerer Bedeutung zu sein als die Rolle der Temperatur.

Die Benetzung und Grenzflächeninteraktionen zwischen Ni-Al Schmelzen und TiB_2 wurden mit dem dispensed drop Verfahren untersucht. Flüssige Ni-Al Legierungen zeigen deutlich unterschiedliche Benetzungsverhalten auf dem TiB_2 Substrat in Abhängigkeit von Legierungszusammensetzung und Testbedingungen. Das Verhalten von Ni-Al Schmelzen auf TiB_2 Keramik verändert sich von einem auflösenden, reaktiven Benetzen (engl. dissolutive, reactive wetting) auf der Ni-reichen Seite zu einem nicht-reaktiven Benetzen auf der Al-reichen Seite. Die Ergebnisse deuten darauf hin, dass der Ni-Gehalt in Ni-Al Legierungen eine Hauptursache für die Veränderungen der Substratauflösung und der geometrischen Konfiguration an der Metall/Keramik Grenzfläche ist. Um den Einfluss des Ni-Gehalts auf die Auflösung von TiB_2 zu verstehen wurde das Schmelzen und Benetzen von $Ni_{83}B_{17}$ und $Ni_{50}B_{50}$ Legierungen auf der TiB_2 Keramik mittels der klassischen Technik des liegenden Tropfens im Hinblick auf mögliches fügen von TiB_2 Keramiken untersucht. Basierend auf den Benetzungstest wurden Zwischenschichten der $Ni_{50}B_{50}$ Legierung verwendet um TiB_2 Keramiken zu Verbinden.

In dieser Arbeit wurde die Technik des liegenden Tropfens erfolgreich angewandt um die Hochtemperaturbenetzung und die Grenzflächeninteraktionen zwischen flüssigen Al, Ti-Al, Ni-Al und Ni-B Legierungen und keramischem TiB_2 zu untersuchen. Die in dieser Arbeit erhaltenen Ergebnisse ermöglichen ein besseres Verständis der Interaktionsmechanismen zwischen flüssigen Al, Ti-Al, Ni-Al und Ni-B Legierungen und TiB_2 keramik in diesen Systemen ermöglichen und Erstellung von Richtlinien für die Herstellung von Metall-Matrix-Verbunden und/oder Keramik-Matrix-Verbunden sowie für die Verbindung von keramischen TiB_2 Teilen für strukturelle Hochtemperaturanwendungen dar.

Content

Chapter 1: Introduction

1.1 Motivation

Wetting behavior is of great scientific importance in a large number of practical fields involving metallurgy, composite fabrication, brazing, solidification, microelectronics, surface coating, liquid-phase sintering, painting, lubrication, adhesion or cleaning [1, 2]. Some applications need poor wetting or even non-wetting. The well-known "lotus effect" plays an important role in self-cleaning and super-hydrophobic properties [3, 4]. With this mechanism it is easy to clean off the contaminants from the surface of materials by rolling liquid droplets. Instead, there are applications that require good wetting of the solid surface by a liquid. For example, metal/ceramic composites processed via spontaneous infiltration significantly depend on the wetting between the porous ceramic and a molten metal. Wetting is also a fundamental factor in metal/metal and metal/ceramic joining.

Surface and heterophase boundaries can serve as the bonding surfaces as well as the sites for component interactions, and play a crucial role in processing and controlling the properties of structures and devices. Interfaces between metals and ceramics are the subject of extensive research, continuously driven by increasing interests in material processing such as composite fabrication [5, 6], selection of crucibles and moulds for molten metal casting [7, 8], surface coating [9, 10], joining of dissimilar materials [5, 11], etc. In comparison with 'chemically inert ambient temperature', high-temperature metal/ceramic interfaces possess their specific features, where self- or second-component diffusion occurs rapidly and reactivity between different phases can take place. These interactions may strongly modify the chemistry and microstructure of the contact region. The final equilibrium configuration of these systems cannot be accurately expressed only based on the concepts established for ambient temperature systems. Therefore, the physical and chemical characteristics of high-temperature metal/ceramic systems are indispensable for understanding fundamental mechanisms of the liquid/solid interaction, controlling technological parameters, and defining properties and quality of final products.

Metal matrix composites (MMCs) can be produced by a variety of routes including solid- and liquid-state techniques. The solid-state processes constitute hot pressing [12, 13], reaction sintering [14, 15], while the liquid-state fabrication techniques include casting [16-18], self-

propagating high temperature synthesis [18, 19], infiltration of porous ceramics by molten metals [20, 21] or laser melting [16, 22, 23]. In comparison with solid-state processes, liquid-state processes have great potentials to be economical, but a metallic matrix and a ceramic reinforcement must be compatible in the temperature range related to the fabrication process. For composites processed by molten metal infiltration, a contact angle as low as 60° is necessary to ensure spontaneous infiltration [24, 25]. If a liquid metal does not wet well a ceramic, the ceramic will detach spontaneously from the metal upon cooling [5]. From the structural viewpoint, the metal/ceramic interface controls the transfer of load between a metallic matrix and a ceramic reinforcement and thereby influences the mechanical properties of MMCs. An ideal interface should be a mechanical continuum, i.e., having coherent atomic bonds across the interface but a chemical dis-continuum indicating no inter-diffusion between the matrix and the ceramic reinforcement [26]. A chemical continuum occurs often due to compound formation at the interface, resulting in some loss in mechanical strength [27]. For example, the longitudinal tensile strength of titanium based matrix reinforced with SiC fiber is severely degraded if the reaction zone between fiber and matrix exceeds a thickness of 1.5-2 μm [28]. Thus, the wetting and interfacial interactions between molten metal and ceramic are crucial factors which help to evaluate the thermodynamic stability of the constituents and impose limits on fabrication methods. So far, it is still quite difficult or almost impossible to have straightforward investigations on the interfacial reaction and phase formation between a matrix and a ceramic reinforcement directly in composites. Therefore, investigations of the metal/ceramic interactions using the sessile drop method are of high technological interests.

Titanium diboride ceramic is extremely important for structural applications where high-temperature stability and damage tolerance are greatly required, e.g., aerospace, automotive and defense applications, due to its combination of exceptional physical and chemical properties, in particular a very high melting temperature, superior hardness, chemical inertness, and a low density [29-33]. Unfortunately, fabrication of large complex-shape TiB_2 parts is still challenging. Complex-shape structures can be created by joining of ceramic with diverse materials, either metals or ceramics (Fig. 1.1.1). This suggests that the performance of structural ceramic components essentially depends on the quality and reliability of the joint interface [34-39]. Therefore, the development of desired joints without defects with satisfactory strength is critical for successful integration of ceramic/metal parts into engineering applications. Among the

joining techniques, brazing which uses a filler metal between the adjoining materials is quite attractive. Properties of brazing material and chemical compatibility between the molten filler and the base material are important factors for obtaining a sound joint [40]. As reported in numerous theoretical and experimental studies, there is a direct correlation between the wetting behavior and interfacial bonding, which finally determines the joint functionality [41-52]. For design of ceramic joining via brazing, it is crucial to understand the wetting of liquid metal on ceramic surface and the liquid/ceramic interactions, and to control the brazing process.

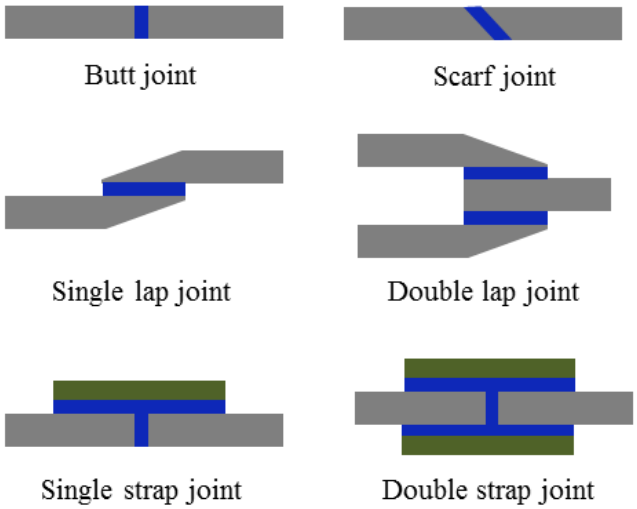

Fig. 1.1.1. Schematic of ceramic/metal joints: grey - ceramic material, blue - filler material, olive – ceramic material (drawn after Ref. [53]).

Studies of wetting and interfacial interactions of ceramic with liquid metals are required for improving the liquid phase-assisted processing, since it is the liquid/solid interface formed that finally determines the properties and quality of these metal/ceramic systems. Thermodynamic calculations can provide insights into the liquid/solid interactions at high temperatures and give basic guidelines for applications. However, empirical results are also needed to follow the development of interfaces when a liquid metal comes into contact with a ceramic surface at high temperatures.

A literature review shows that the investigations of wetting and interfacial interactions of low melting-temperature metals (e.g., In, Sn, Pb, Al) with oxide ceramics have been carried out rather extensively (see for example Refs. [54-58]). However, only limited reports can be found

on the high melting temperature metals with ultra-high temperature diboride ceramics such as HfB_2, ZrB_2 and TiB_2. In particular, TiB_2 with a melting temperature of about 3200 °C and a density of 4.52 g/cm^3 is interesting as an electrode material in the aluminum industry, as thermal barrier or wear resistant coatings or as a constituent of light-weight composites for aerospace, automotive and defense applications [31-33]. TiB_2 particles are also used for the microstructure refinement or reinforcement in Al-based cast alloys [59-62].

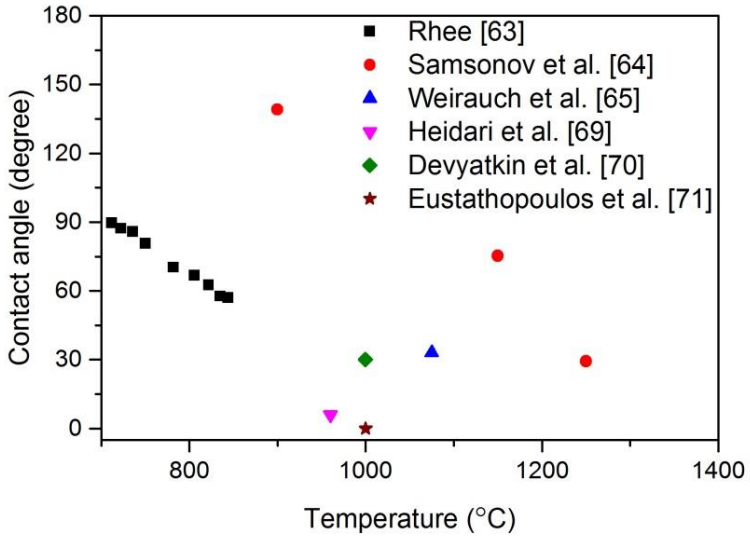

Fig. 1.1.2. Contact angle in Al/TiB_2 system reported in various studies.

The study on wetting and interfacial interactions between TiB_2 and pure liquid metals such as Al [63-71] and Ni [72-76] has been carried out in different laboratories. However, the published results are very scattered, as it can be seen from the temperature dependence of the contact angle in Fig. 1.1.2. For example, Rhee [63] studied the wetting of a dense TiB_2 (98.5 % of the theoretical density) by liquid Al under a vacuum better than 2.7×10^{-7} mbar by the sessile drop method. He has demonstrated that by holding the system isothermally for at least 30 min at a given temperature, the equilibrium contact angle reached about 90° at 710 °C and about 60° at 840 °C respectively [63]. However, Samsonov *et al.* [64] did not observe any wetting of TiB_2 substrates by liquid aluminum between 900 °C and 1000 °C under vacuum. The contact angle decreased to about 75° and 30° after 20 min of isothermal heating at 1150 °C and at 1250 °C, respectively. Weirauch *et al.* studied the wetting behavior of liquid Al on different TiB_2

substrates at a constant temperature of 1025 °C [65]. It was reported that the initial contact angle of about 120°-140° for liquid Al on a polished TiB_2 substrate (99.8 % of the theoretical density or better purity) decreased to 0° after prolonged holding for 17 h. The contact angle data on Ni/TiB_2 reported by Yasinskaya [72], Samsonov *et al.* [73], Kotsch [74] and Eremenko and Naidich [76] show a large scattering both for the contact angle and the wetting temperature as presented in Fig. 1.1.3. The high-temperature interactions between Ti and TiB_2 have been mainly studied for powdered materials [15, 77-81]. To our knowledge, there has been no reports on the wetting and interfacial interactions between binary Ti-Al, Ni-Al and Ni-B liquid alloys and TiB_2 ceramic, despite high technological interests in these systems.

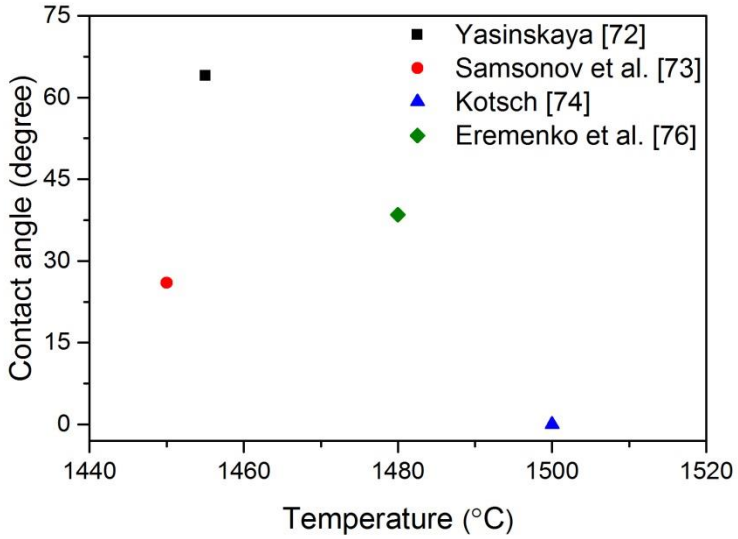

Fig. 1.1.3. Contact angle in Ni/TiB_2 system reported in different laborotories.

1.2 Objectives

In this thesis, the sessile drop method has been used to quantitatively characterize the wetting properties and to study the interfacial interactions in liquid metal/ceramic systems. The present study is focused on the systematic investigations of wetting and interfacial interactions of molten Al, Ti-Al, Ni-Al and Ni-B alloys with TiB_2 ceramic. This includes studies on the: (i) stability of TiB_2 ceramic in contact with a liquid metal; (ii) wetting, spreading and infiltration

behavior of the metallic melt in contact with TiB_2 ceramic; (iii) phase formation and diffusion studies at the drop/ceramic interface.

The obtained results provide information required for understanding the high-temperature interaction mechanisms in these systems and development of the guidelines for the fabrication of TiB_2 containing composites and joining of TiB_2 ceramic components.

1.3 Structure of the thesis

This PhD thesis is presented in seven chapters. The general introduction (Chapter 1) contains motivation, objectives as well as the structure of the thesis.

The fundamental knowledge available in the literature is presented in Chapter 2. This chapter discusses the following topics: a brief review about the ultra-high temperature ceramics, properties, synthesis and applications of TiB_2 ceramic. The final part of this chapter is dedicated to the basics of the wetting phenomenon with the focus on the contact angle, measurement of the contact angle, factors affecting the wetting, classification of the contact angles and different types of the wetting.

The experimental procedures are briefly presented in Chapter 3. This includes the details about the sample preparation (metallic alloys and TiB_2 substrates) and sessile drop method (classical sessile drop and dispensed drop techniques). The final section of this chapter describes the characterization of the metal drop/ceramic couples, including microstructure and phase identification.

The Chapters 4-6 form the core of the present thesis. These chapters present in details the results and discussion, and clearly exhibit the progress of this study towards its objectives.

Firstly, Chapter 4 deals with the temperature- and time-dependent wetting between the liquid Al and TiB_2 ceramic over a wide temperature range using both the classical sessile drop and the dispensed drop techniques. In this work, the wetting behavior of liquid Al on TiB_2 studied by these two different techniques is compared. The effects of temperature on wetting and interfacial microstructure are discussed in detail. The results reported in this chapter establish a basis for the further study of Al-containing binary alloys such as Ti-Al and Ni-Al.

Chapter 5 presents a systematic investigation on the interfacial reactions between Ti-Al melts and TiB_2 ceramic by classical sessile drop technique because of a severe reaction of pure Ti and Ti-containing melts with an alumina drop dispenser. The effects of alloy composition and

experimental temperature on the interfacial microstructure and phase formation are studied in details. Finally, the microscopic and macroscopic cracks formed in the Ti-Al/TiB_2 couples upon cooling and thermomechanical compatibility of the Ti-Al alloys and TiB_2 ceramic are discussed.

The wetting and interfacial interactions between Ni-Al molten alloys and TiB_2 ceramic are discussed in the first section of Chapter 6. The high-temperature measurements of the Ni-Al/TiB_2 system are carried out by the dispensed drop technique. It is established that the increase in Ni content in the Ni-Al melts causes a notable dissolution of the substrate and formation of a sigmoidal interface profile. Aiming to exploit the effect of Ni content on the substrate dissolution, high temperature studies of $Ni_{83}B_{17}$ and $Ni_{50}B_{50}$ melts on TiB_2 substrates are carried out. In view of possible joining of TiB_2 ceramics, the tests are performed using the classical sessile drop technique. Based on the wetting test, joining of TiB_2 ceramics by $Ni_{50}B_{50}$ melt-spun ribbon is studied. These results are presented in the second section of Chapter 6.

In Chapter 7, the results of this work are summarized and outlooks on further research works are presented.

Chapter 2: Fundamentals

This chapter provides background for a better understanding of this research carried in this work. It begins with an introduction to ultra-high temperature ceramics, followed by a description of the basic properties and synthesis of TiB_2 ceramic. An insight on its applications as high-temperature structural materials is addressed. The final section of this chapter describes the theoretical background of wetting with emphasis on the contact angle, measurements of the contact angle, the various factors affecting the wetting, classification of the contact angles and different types of the wetting.

2.1 Ultra-high temperature ceramics

Since the 1960s, aerospace industry has an increasing demand on materials that could withstand high-temperature aggressive environments. Ultra-high temperature ceramics (UHTCs) have emerged as material of choice, representing a family of materials that exhibit excellent stability at temperatures exceeding 2000 °C [82]. These materials are composed of borides, carbides, and nitrides of the transition metals. UHTCs are characterized by very high melting temperatures, high hardness, good chemical and thermal stability under certain conditions, and excellent wear and oxidation resistances. Therefore, UHTCs are promising for use under extremely aggressive environments, such as thermal protection materials on hypersonic aerospace vehicles or re-usable atmospheric re-entry vehicles, refractory crucibles, etc [30, 83, 84].

UHTCs exhibit good structural stability at high temperatures because of the presence of strong covalent bonds. Among the UHTCs, diborides (HfB_2, ZrB_2 and TiB_2) possess hexagonal close packed structure with alternating two-dimensional boron and metal sheets and have great potentials for applications, where high temperatures and thermal fluxes are involved. In this dissertation, titanium diboride is studied.

2.2 Titanium diboride

2.2.1 Phase diagram and crystal structure

According to the calculated phase diagram [85], three equilibrium boride phases - orthorhombic TiB, orthorhombic Ti_3B_4 and hexagonal TiB_2, exist in the binary Ti-B system (Fig. 2.2.1). TiB and Ti_3B_4 undergo peritectic reactions at 2107 °C and 2135 °C, respectively. TiB_2 melts congruently at 3200 °C.

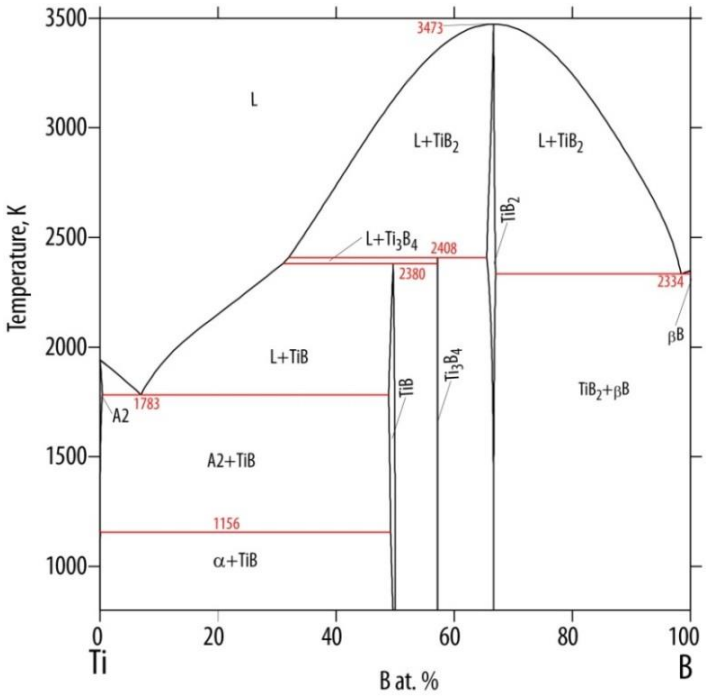

Fig. 2.2.1. Binary phase diagram for Ti-B system, calculated with Thermo-Calc software using the thermodynamic data from Ref. [85] (courtesy of Dr. V.T. Witusiewicz).

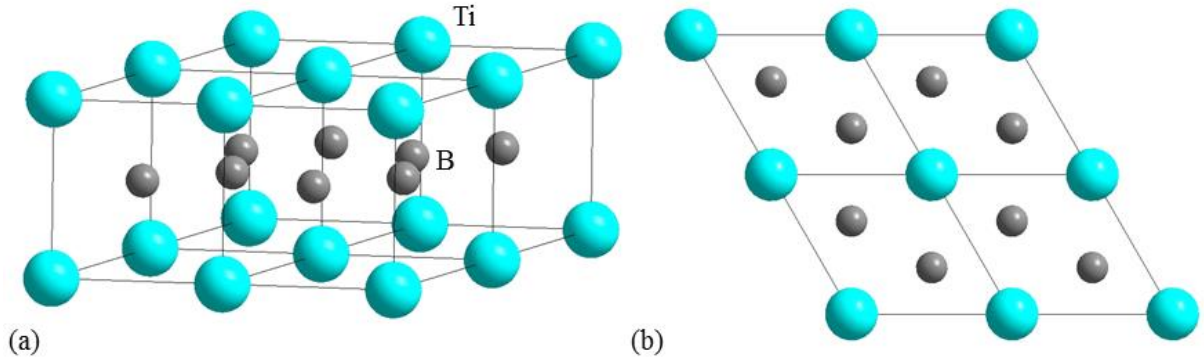

Fig. 2.2.2. The structure of TiB_2 (2×2×1 unit cell): (a) perspective view; (b) [001] projection. (calculated with Diamond programm using crystallographic data from Ref. [86]).

The crystal structure of TiB_2 is hexagonal, AlB_2-type with a *P*6/mmm space group (a = b = 0.3028 nm, c = 0.3228 nm; $\alpha = \beta = 90$, $\gamma = 120$) [86]. The hexagonal unit cell of TiB_2 crystal is shown in Fig. 2.2.2, where the Ti layers in a hexagonal close packed array are alternated with layers of B atoms in two-dimension graphite-like rings. In the boron layer, each boron atom has three boron neighbors in a trigonal planar arrangement in the form of two-dimensional network with a distance of 0.175 nm. According to the appropriate primitive lattice vectors, the atoms in the unit cell are positioned at Ti(0,0,0), B(1/3,2/3,1/2) and B(2/3,1/3,1/2) [86].

TiB_2 shows unique combination of superior properties including high melting point, high hardness, high electrical conductivity, good thermal conductivity and considerably good chemical stability (see Table 2.2.1).

Table 2.2.1. Properties of TiB_2 [29, 87, 88]

Properties	TiB_2
Crystal structure	hexagonal
Density (g/cm^3)	4.52
Melting point (°C)	3200
Hardness (GPa)	24
Compressive strength (GPa)	1.8
Wear coefficient (10^{-3})	1.7
Fracture toughness ($GPa \cdot m^{1/2}$)	6.2
Young's modulus (GPa)	575
Thermal expansion ($10^{-6} \cdot K^{-1}$)	6.7 – 8.2
Thermal conductivity ($W \cdot m^{-1}\ K^{-1}$)	96 (20 °C)
	81 (500 °C)
	78.1 (1000 °C)
Electrical resistivity (μΩ·cm)	9-15 (20 °C)
	60 (1000 °C)

2.2.2 Synthesis of TiB_2 ceramic

Production of TiB_2 powder

Electrochemical synthesis and solid-state reaction have been well developed to produce fine TiB_2 powder in large quantities. Borothermic reduction of titanium oxide by boron carbide and carbon is one typical example of a solid-state reaction, which produces a large quantity of TiB_2 on both laboratory and commercial scales. The borothermic reduction occurs via the following reaction [89]

$$2TiO_2\,(s) + B_4C\,(s) + 3C(s) \rightarrow 2TiB_2\,(s) + 4CO\,(g) \qquad (2.2.1)$$

Formation of TiB_2 is thermodynamically feasible at temperatures above 984 °C only, as ΔG for the reaction is positive at lower temperatures [90]. Alternatively, B_4C can be substituted by B_2O_3 as a source of boron. Impurities may arise from the borothermic reduction or subsequent processing.

Self-propagating high-temperature synthesis (SHS) can produce ultrafine TiB_2 powders on nanometer scale. This method can exploit the thermal energy generated by highly exothermic reaction to be self-sustaining. SHS offers advantages with respect to the fast reaction rates, low power consumption and environmental effect, relatively convenient process, low cost and high purity of the products. Various amounts of NaCl are generally added during the SHS process. As the amount of NaCl (diluents) increases, the particle size of TiB_2 powder decreases and even reaches a size of about 26 nm with 20 wt.% NaCl [91].

Sintering of TiB_2 ceramic

The properties of TiB_2 ceramic significantly depend on the microstructure (grain size, porosity, micro-crack, etc). The low diffusion rate and oxide layer formed on the surface of TiB_2 particles retard their sinterability [92]. However, high density TiB_2 ceramic can be produced at high temperatures with an appropriate pressure. Wang *et al.* produced high density TiB_2 at 1800°C and under 30 MPa pressure [93].

So far, TiB_2 has been produced by a variety of methods such as hot-pressing [92, 94, 95], pressureless sintering [96, 97], reactive electric discharge sintering [98], and spark plasma sintering [99, 100]. However, there are still some stumbling blocks (technical and/or economical) that restrict the fabrication of TiB_2 ceramic for industrial applications. Hot-pressing can produce

high density TiB_2 ceramic with application of both high temperatures and external pressure, while it is relatively expensive and leads to low productivity along with limitations in the final shape (restricted to relatively simple geometries) [92]. Pressureless sintering overcomes the deficiency in hot pressing with low cost, but it requires a relatively high sintering temperature (~ 2000 °C). Unfortunately, high processing temperatures can cause exaggerated grain growth and introduce deleterious internal stresses due to the anisotropy in hexagonal structure, resulting in the onset of spontaneous micro-cracking upon cooling [87].

In such view, appropriate sintering aids are used to increase the sinterability and obtain high densification and satisfactory structure at reasonable temperatures. The sintering aids segregate preferentially along the high-energy crystallographic planes, which decrease the crystalline anisotropy and provide a better control over the microstructure development [101]. Also, finely dispersed particles at the grain boundaries can effectively pin the grain boundaries and inhibit grain growth. However, sintering aids not only modify the ceramic structure, but also form new phases and/or grain-boundary precipitates [94, 95, 102]. As the sintering aids can change the character of bulk ceramic and its properties, this must be carefully considered in order to choose the right sintering aid, which is compatible with desired ceramic application [103].

2.2.3 Applications of TiB_2

TiB_2 ceramic covers a wide variety of applications in extreme environments. One such application, which has attracted attentions towards borides as high temperature structural materials, is thermal protection system of space vehicles [104-106]. The thermo-physical and thermo-mechanical properties of TiB_2 render it suitable for such application, while its relatively low density aids them to be used for aerospace applications. The combination of high electrical conductivity, low solubility in and high wettability by liquid aluminum has made TiB_2 ceramic attractive as electrode materials in the electrochemical reduction of alumina to aluminium metal in industry [103, 107]. Due to its low density and high impact strength, TiB_2 is favored for making armor components in military clothing and vehicles [31]. TiB_2-based materials are used as cutting tools and high-temperature wear-resistant parts. Sigl *et al.* [108] have demonstrated that the TiB_2 composites for continuous cutting operations match or surpass conventional tool materials in cutting aluminum and cast iron. Due to a good thermodynamic stability, high

hardness, low density as well as chemical inertness, TiB_2 particles are used as outstanding microstructural refiners for the fabrication of composites, improving their properties and extending their attractiveness in applications [59-62]. It comes to the conclusion that the applications of TiB_2 ceramic would develop more widely, if its fabrication and machinability are optimized in the future.

2.3 Wetting basics

2.3.1 Contact angle

Wetting is the ability of a liquid to maintain contact with a solid, resulting from intermolecular interactions, when these two phases are brought together. The extent of wetting is determined by a force balance between adhesive and cohesive forces. Contact angle is a unique characteristic of a solid-liquid-vapour system to describe the intrinsic degree of wetting, which is quantitatively defined as the angle formed by the tangent to a drop at the three-phase contact point.

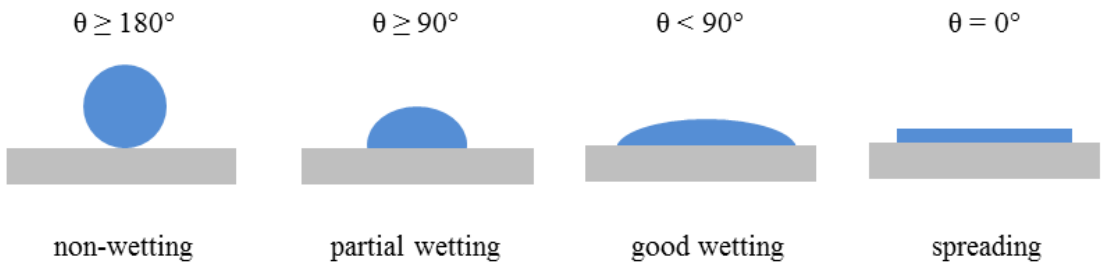

Fig. 2.3.1. Different wetting states of a liquid drop on a solid substrate.

The contact angle tends to decrease when a liquid drop spreads over a solid substrate. Therefore, the contact angle shows an inverse increase with the degree of wetting as it can be seen in Fig. 2.3.1. A contact angle less than 90° indicates that the liquid spreads to some extent and comes to rest on the substrate. This case is identified as good wetting. When a liquid spreads little or may not spread at all, a contact angle greater than 90° is obtained and is regarded as poor wetting or non-wetting. If a liquid covers the substrate completely as a thin film, the contact angle tends to be zero, which is considered as a perfect wetting.

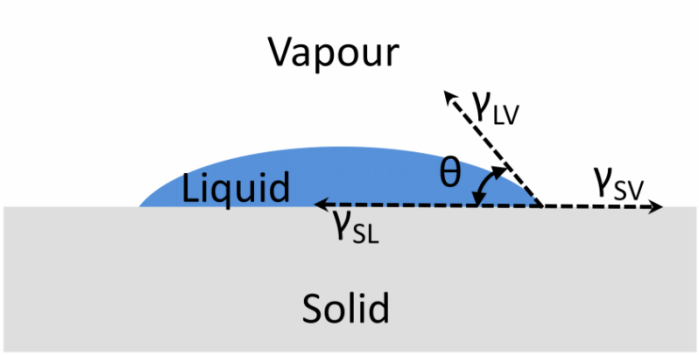

Fig. 2.3.2. Definition of an equilibrium contact angle θ.

If a non-reactive liquid is deposited on a perfectly smooth and chemically homogeneous solid surface, a new equilibrium will be set up. This equilibrium is mainly governed by the laws of thermodynamics, depending on the surface and interfacial energies involved at the liquid/solid/vapour interface. The contact angle θ can be quantified by Young's equation (Fig. 2.3.2). This equation is a thermodynamic tool to provide insights into the energies existing between the liquid/solid/vapor interfaces and has become a milestone in the wetting studies [109]. The equation is expressed as below

$$\cos \theta_Y = (\gamma_{sv} - \gamma_{sl}) / \gamma_{lv} , \qquad (2.3.1)$$

where θ_Y is the Young's contact angle at the triple line, γ_{sv}, γ_{lv} and γ_{sl} define the solid-vapour, liquid-vapour, solid-liquid interfacial tensions. The notion of interfacial tension γ_{ij} represents as the free energy necessary to increase the contact area between two different phases *i* and *j* by one unit [1]. This equation corresponds to the vector equilibrium obtained by the interfacial tensions of the three phases at the triple line, where Young's contact angle significantly depends on the interfacial tension γ. For a change of the contact angle, at least one of these interfacial tensions should be altered.

Young's equation describes the dependence of the contact angle on the nature of the materials involved in a true equilibrium condition [110]. It has to be pointed out that other external effects should not interfere with the liquid and its wetting behavior. This equation actually explicitly assumes the following conditions [110]:

(1) The solid surface has to be strictly rigid, i.e. flat, perfectly smooth and chemically homogeneous.
(2) The liquid and solid have to be 'perfect' and their physical and chemical properties must be determined before the wetting process.
(3) The solid-liquid-vapour system has to be in a true equilibrium condition.
(4) The liquid and solid phases would not undergo any transformation during the overall wetting process.
(5) There is not any chemical interaction between liquid, solid and wetting environment.
(6) No externally dynamic effects occur, which would alter the equilibrium condition between the solid-liquid-vapour system.

2.3.2 Measurement of contact angle

Due to its relative simplicity, the sessile drop method is widely used for examination of the wetting phenomena bot at room temperature and at elevated temperatures. This is due to its high adaptability and precision, theoretical soundness and possibility for obtaining maximum information about the objectives involved [42, 43]. In its classical form, a metallic piece is placed on a substrate at the beginning of sessile drop experiment and both substrate and sample are jointly heated from room temperature (Fig. 2.3.3a). This procedure is called as contact heating.

It should be noted that despite apparent simplicity of the sessile drop experiments, measurement of reliable angles, especially at high-temperature, is still a challenging issue. The testing equipment and procedures are greatly different in different research groups, leading to a large dispersion in contact angle for a given metal/ceramic system [111, 112].

The problems of the high-temperature wettability experiment are explained by the following aspects [42, 113-115]: (i) diversity of the sessile drop techniques and lack of standards for testing equipment and procedure; (ii) high sensitivity of the wetting tests to the experimental conditions, especially vacuum or inert gas quality; (iii) chemistry and morphology of the substrate surface; (iv) homogeneity of sizes of the thermal field, influencing thermodynamic equilibrium in a system under investigation.

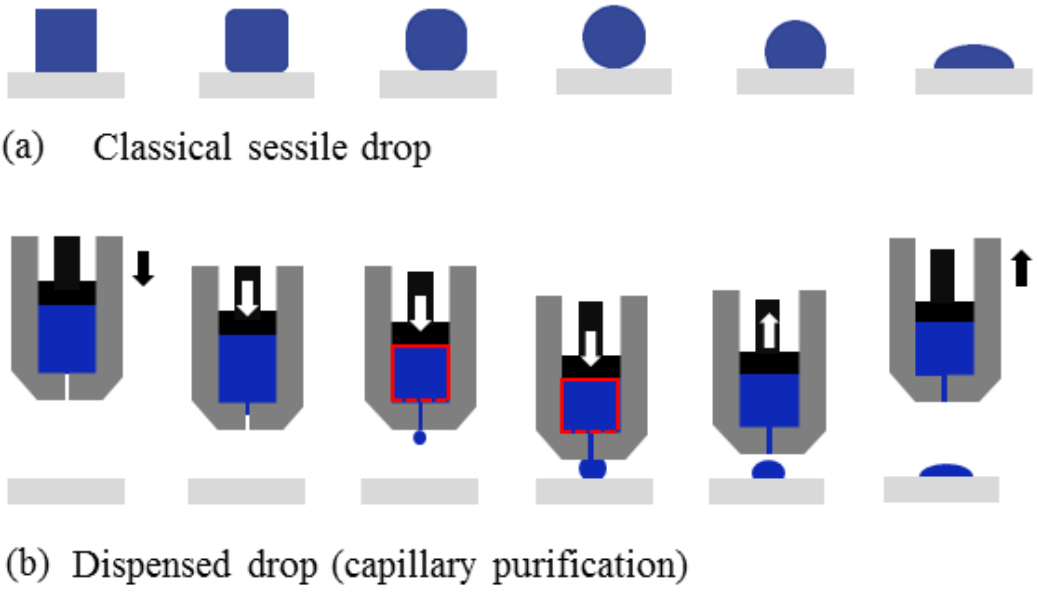

Fig. 2.3.3. Schematic illustrations of the two different sessile drop procedures: (a) Classical sessile drop technique; (b) Dispensed drop technique, showing a design of a drop dispenser to squeeze a drop and break the oxide film (drawn after Ref. [116]).

To obtain reliable results, negative effects of the above listed factors must be excluded or at least reduced as much as possible. The chamber atmosphere must be controlled carefully. High vacuum conditions ensure to avoid or minimize the contamination from residual gases in particular oxygen, but evaporation from the liquid and/or the solid surfaces can change the residual atmosphere. The evaporation can be suppressed or reduced in an inert gas atmosphere, but the inert gas must be of high purity. The heating method greatly affects the interaction of a metallic phase in contact with a solid surface at a solid state. Often, a metal/ceramic interaction occurs via elemental diffusion, when they are jointly heated up. This causes composition change at the interface and consequently the melting temperature, as will be seen also from our studies presented in the next chapters.

To exclude the effects of the contact heating, the melting and wetting tests should be processed separately. This can be realized by the dispensed drop technique [110]. In this technique, a metal is molten in a drop-dispenser placed above a substrate and a molten drop is squeezed out on the substrate by using a piston. In comparison to the classical sessile drop technique with contact heating, the dispensed drop technique enables mechanical removing of an

oxide layer from liquid metal by squeezing it through a hole in the drop dispenser, as schematically shown in Fig. 2.3.3b. This improved technique allows investigation of the wetting from the first moment contact of the liquid metal with the substrate.

In the last decades, great progress has been made in the scientific instruments used for high-temperature experiments. The wetting studies benefit from high-purity inert gases or ultra-high vacuum standards as well as high-resolution/high speed digital video imaging. A wide use of sophisticated sessile drop methods has also made great improvements in high-temperature experiments. Computer programs have been developed, which allow the data acquisition and automatic image analysis [5, 117, 118].

2.3.3 Factors affecting wetting

Wetting phenomenon is determined not only by the properties of a liquid/solid system under study; it is also very sensitive to the experimental conditions. It is therefore necessary to consider possible factors, which could turn up in a wetting test. Among them, drop size, substrate surface quality, test chamber which can provide a well-controlled vacuum or inert gaseous atmosphere, temperature control, and means to measure drop geometry and dimensions.

Properties of spreading liquid

Viscosity, density and surface tension are all important properties that affect spreading of the liquid over a solid surface. The independent study on each of these factors is extremely difficult, as the evolution of contact angle is governed by these factors simultaneously [2].

For non-reactive wetting, spreading rate depends on the viscosity of the liquid. A high-viscous liquid spreads less than low-viscous one under the same conditions. This is due to the fact that high viscous dissipation reduces the spreading rate. The effect of gravity is generally not taken into account in wetting studies, if the liquid drops used in sessile drop experiments are too small to affect the spreading. Also, the gravity force will not affect the liquid spreading when the drop radius is less than the capillary length (the square root of the ratio of liquid surface tension to the mass of liquid drop). According to Young's equation, a small contact angle is obtained when the liquid/vapour interfacial tension, usually called surface tension, is relatively low. This

suggests that the wettability of a solid by a liquid can be improved by lowering the liquid surface tension.

The wetting can also be improved by reducing or removing the oxide film from the liquid surface [119] or by reducing the solid/liquid interfacial tension γ_{sl} [120]. The latter one works through adsorption of active additions, which segregate or even form an intermediate phase at the interface. For example, Ag alloyed with Ti (or Zr, Hf) wets ZrB_2 ceramic more readily in comparison to pure Ag [120]. For non-reactive metals, concentration of alloying elements must be higher than 10 at.% in order to improve wetting, but this often results in an undesired change in the properties [111].

Substrate properties

a. Surface roughness

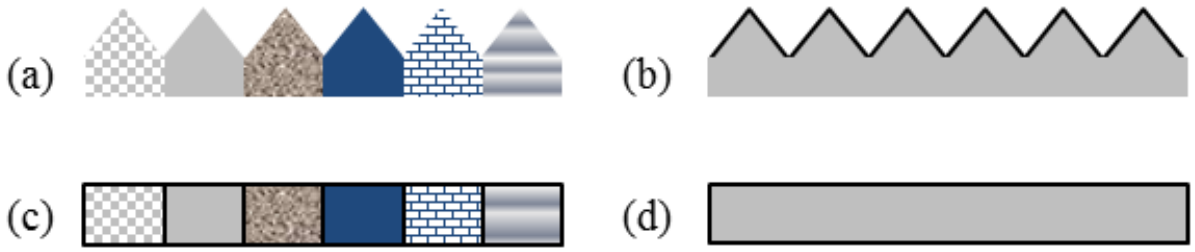

Fig. 2.3.4. Possible morphologies of solid surfaces under real conditions: (a) regularly rough, chemically inhomogeneous; (b) regularly rough, chemically homogeneous (Wenzel state); (c) flat, chemically inhomogeneous (Cassie-Baxter); (d) flat, chemically homogeneous (YE) (drawn after Ref. [110]).

The substrate surfaces are not “flat and homogeneous” in real experimental conditions as schematically shown in Fig. 2.3.4. For example, residual pores (larger or smaller) are always present in the ceramics produced by sintering. It is generally accepted that the substrates with a random roughness no higher than 100 nm should be used to obtain reproducible results with a good accuracy [121]. Therefore, characterization of the substrate surfaces have to be performed at a microscopic scale before and after the wetting tests in order to identify pores in the sintered material, possible localized defects such as holes caused by decohesion of grains during

polishing, or even scratches. All these defects can pin the triple line and affect the spreading of the melt. For a regularly rough but homogeneous surface (Fig. 2.3.4b), Wenzel [122] has been proposed the following relationship for the contact angle

$$\cos \theta_w = r \cos \theta_Y \,, \tag{2.3.2}$$

where θ_w is the apparent contact angle which corresponds to a stable equilibrium state. θ_Y is the Young's contact angle as defined for an ideal surface. The roughness factor, r, is defined as the ratio of the true area of solid surface to the planar area ($r > 1$). The roughness factor is a measure of how surface roughness affects a homogeneous surface.

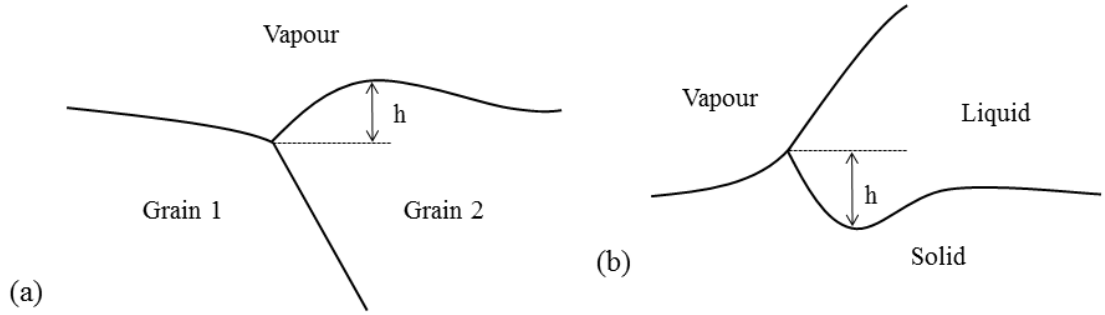

Fig. 2.3.5. Grain-boundary groove (a) and wetting ridge at the triple line (b) (drawn after Refs. [123, 124]).

For a high-temperature liquid metal/ceramic system, the initially smooth substrate is often secondary-roughed with time. The secondary roughness would pin the triple line at a position far from the equilibrium, i.e. at a contact angle markedly different from θ_Y [5]. This phenomenon may be caused either by local diffusion or dissolution/precipitation of the solid or by formation of a rough reaction layer ahead of the triple line, which possesses a different wetting property compared to the original substrate. The dissolution/precipitation processes appear in the form of grain-boundary grooves or wetting ridges at the junction (Fig. 2.3.5) for metallic melts exposuring temperatures typically higher than (0.2-0.5)T_m (T_m being the subtrate melting point) [123]. As reported by Eustathopoulos *et al.* [112], a wetting ridge with a height larger than 10 nm can affect the spreading rate during the wetting test. As an example, for pure Ni on Al_2O_3, the time t_r needed for a wetting ridge to attain the height h = 10 nm, is about 0.5 s [112]. Therefore, much longer spreading time in this system would contribute to wetting

hysteresis.

b. Chemical heterogeneity

Chemically heterogeneous surfaces are commonly observed due to impurities present on the surface. As for sintered ceramics, they initially contain impurities or additives in the sintering powder. The sintering additives would exist as secondary inter-granular phases. In the case of heterogeneous surface formed by two different materials, the contact angle can be expressed by Cassie equation [125]:

$$\cos\theta_c = f_1 \cos\theta_1 + f_2 \cos\theta_2 , \qquad (2.3.3)$$

where f_1 and f_2 are the surface fractions of phase 1 and 2. θ_1 and θ_2 represent the contact angles on phase 1 and 2, respectively. For a porous solid, the θ_2 is taken as 180°.

c. Surface modification

Local modification of the structure and/or the chemistry of the substrate surface can essentially change the wetting behavior and interfacial bonding in a metal/ceramic couple [111]. One way for this purpose is to perform surface treatment, e.g. preheating in air or in vacuum. A better wetting by liquid Cu can be achieved through a modification of the AlN surface to form Al_2O_3 [126]. Another way to promote wetting is surface coating, where the substrate surface is protected against the aggressive melt [113]. Sobczak *et al*. has reported that the wetting between liquid Al and the ceramic deposited with metallic coating of more than 1 μm thickness is similar to that on a monolithic metal, while the final contact angle only depends on the original ceramic [127, 128].

Atmosphere

The high-temperature wetting experiments are usually carried out under high vacuum or inert gas atmosphere. Reactive impurity, especially oxygen in a specific environment has a strong impact on the surface tensions of the liquid and the substrate. Also, a thin oxide layer on the substrate surface can have influence on the apparent contact angle and the wetting hysteresis. For example, the role of aluminium oxidation in the wetting of oxide ceramics (Al_2O_3, TiO_2, ZrO_2, SiO_2) has been reported by Sobczak and Asthana [52]. Similar effects were also observed

in our study of liquid Al on TiB_2 [129].]. Hence, preventing of oxidation or removing of existing oxide films is essential to evaluate true wetting properties.

Temperature

Wetting of a liquid on a solid substrate is very sensitive to the temperature, which influences the properties like viscosity, surface tension, oxidation behavior, and reactivity of the liquid with a substrate. The viscosity and surface tension of a liquid generally decrease by increasing the temperature. Hence, wetting can be improved in most systems by increasing the temperature. Even in a reactive wetting system, increasing temperature can increase the diffusion rate and as a consequence speed up the wetting process [2].

Device design and testing procedure

The fair reliability and repeatability of contact angle measurements are main challenges in the sessile drop tests, which significantly depend on the level of instruments, test approaches and experience of the operators. It is, therefore, necessary to understand the influence of the following issues [130]:

a. Drop evaporation

Drop evaporation may lead to modification of the drop composition, drop size, substrate surface and chamber atmosphere along with blurring of the recorded images due to deposition of a metal on the observation window. In such cases, it is difficult or even impossible to determine properly the drop profile and a substrate surface position (consequently the contact point) and to draw the tangent line and determine the contact angle. In a case of severe drop evaporation, the apparent decreasing of the contact angle can be caused by decreasing drop height at a constant drop diameter, and not due to improving of the wetting. Continuous video recording of a liquid drop on a substrate might help to reveal the effect of evaporation by measuring the drop height and diameter. Additionally, it is useful to measure the mass of the substrate and the sample before and after a high-temperature test.

b. Drop movement

Drop oscillation on the horizontal plane due to external factors (such as building vibration, improper connection of the working components and the chamber, etc.) can make it difficult to determine the contact point with sufficient precision. Drop migration may cause part of the drop/substrate system hidden behind a chamber component and result in imaging of the off-centered drop.

c. Imaging of the drop

In the sessile drop method, the wetting behavior (contact angle) is quantitatively evaluated by analysis of the digital photographs of a sessile drop. In order to extract a reliable and reproducible information, the image of the drop should be axisymmetric with well-demarcated boundaries. Improper analysis of the sessile drop images may also lead to scattering in the data.

2.3.4 Classification of contact angle

The measurement of contact angles is extremely sensitive to different factors involved in a test as explained above. Therefore, a variety of contact angles has been defined to address various cases [131].

Equilibrium/Young's contact angle, contact angle obtained by a non-reactive liquid spreading on an ideal solid under thermodynamic equilibrium conditions. The Young's equation (Eq. 2.3.1) determines a single value for the equilibrium contact angle $\theta = \cos^{-1}((\gamma_{sv} - \gamma_{sl})/\gamma_{lv})$ (the substrate as shown in Fig. 2.3.4d).

Intrinsic contact angle, equilibrium contact angle formed under the conditions when there is no oxide or film/contaminant covering the substrate surface or spreading liquid. θ_i is seen in Fig. 2.3.6.

Apparent contact angle, contact angle formed on a real solid substrate, θ in Fig. 2.3.6. For an ideal solid surface, the apparent contact angle equates to the intrinsic contact angle. For a homogeneous rough surface, the apparent contact angle is the difference between the intrinsic contact angle and the local angle of inclination of the solid surface [2].

Wenzel angle, apparent contact angle obtained on a topologically heterogeneous surface caused by surface roughness or porosity (the substrate as shown in Fig. 2.3.4b).

Cassie angle, contact angle formed on a chemically heterogeneous surface owing to surface contaminants, segregation phases or secondary inclusions (the substrate as shown in Fig. 2.3.4c).

Dynamic angle, time-dependent contact angle which is measured before an equilibrium is reached between a liquid on a solid.

Advancing/receding angle, contact angle determined when the liquid front spreads on the surface/when the liquid retreats from the vapour phase, with $\theta_r < \theta_Y < \theta_a$ (Fig. 2.3.7).

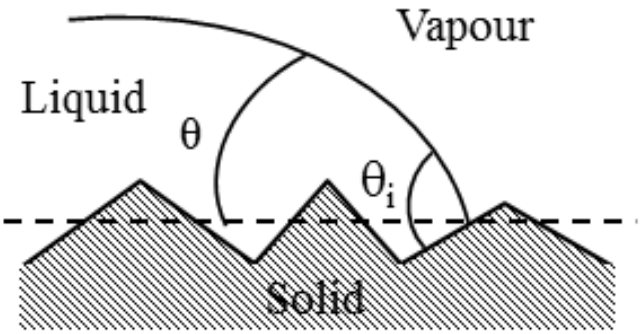

Fig. 2.3.6. Scheme of apparent and intrinsic contact angle on a real surface (drawn after Ref. [132]).

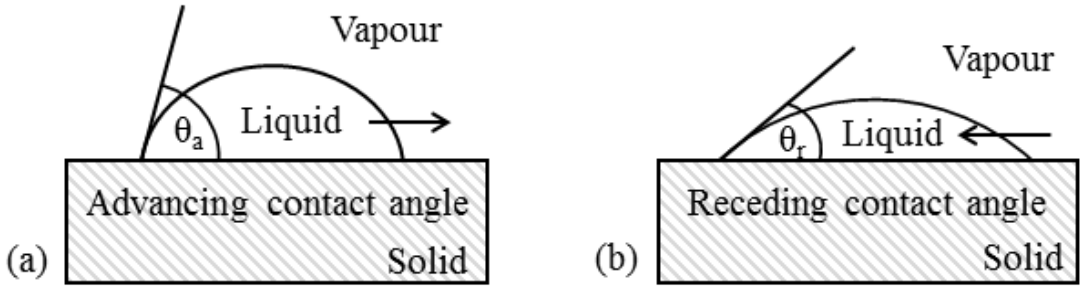

Fig. 2.3.7. Advancing(a) and receding (b) contact angles (drawn after Ref. [133]).

2.3.5 Different types of wetting

Wetting phenomenon can be classified into two categories: non-reactive and reactive wetting. During non-reactive wetting, the liquid spreads over a substrate without any reaction/absorption with the solid substrate or mass transfer through the liquid/solid interface is

too limited to affect the interfacial interactions. In contrast, reactive wetting involves an interaction between the liquid and the solid substrate. The liquid/solid interactions such as diffusion or chemical reaction not only modify the spreading rate but also affects the extent of wetting [2].

Non-reactive wetting

The spreading of some non-metallic liquids on inert solid surfaces is identified as non-reactive wetting, e.g. water or polymeric liquids on glass or metallic substrates. If the mass transfer through the interface is absent or limited, the interfacial energies in the liquid/solid system remain constant over time [112]. In such cases, the wetting process occurs by a displacement of the triple line as a function of time and the triple-line friction is a main factor governing the wetting kinetics in isothermal studies [134].

Due to a low viscosity of liquid metals at high temperatures, the lateral movement of the triple line is quite fast on a flat, unreacted surface. The spreading time for a millimeter-size low-viscous droplet it takes 10^{-2} – 10^{-1} s or even less to reach an equilibrium contact angle $\theta_Y > 20°$ [112]. In general, reliable determination of the contact angle is extremely difficult in view of such high spreading rates. However, development of high-speed high-resolution CCD cameras enables getting plausible information on the fast wetting kinetics at present.

Reactive wetting

For reactive wetting, the spreading time for a millimeter-size droplet to attain its equilibrium, is quite different ranging from a few seconds to several hours. The spreading in a reactive system is a two-stage process and can be divided into two limiting cases depending on the rate of local reaction at the triple line and the rate of diffusive supply of reactive elements from the bulk drop to the triple line, respectively. The kinetics at the triple line is rate-limited when diffusion within the droplet is comparatively rapid and the transport (diffusion and convection) is also rate-limited as the local reaction rate is comparatively rapid [2, 135]. It means that the spreading rate of reactive wetting is not only limited by viscous dissipation but also by the rate of interfacial interactions at the triple line [136, 137]. This explains why the spreading time in reactive wetting is several orders magnitude larger than that in non-reactive wetting.

Reactive wetting can be split into substrate dissolution in the liquid and formation of a continuous layer of new products [112].

a. Substrate dissolution

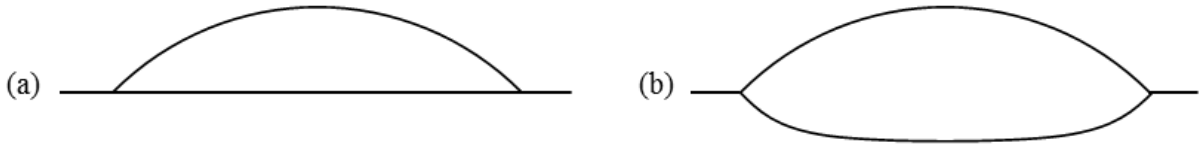

Fig. 2.3.8. Two extreme cases of dissolutive wetting: (a) solid solution modifies interfacial energies while liquid/solid interface remains flat; (b) solid dissolution only modifies the geometry at the triple line (drawn after Ref. [112]).

As the atomic mobility is significantly increasing at high temperatures, the dissolution of a solid substrate into a melt is a phenomenon occurring in some metal/ceramic systems such as AuNi/ZrB_2 [138] and Ni/HfB_2 [139]. Even if no chemical reaction occurs, the composition of liquid phase changes with time so that a new dynamic condition is built [110]. Dissolutive wetting works through two extreme cases [112]. Firstly, the surface and interfacial energies are modified by dissolution of a small quantity of tension-active components from the solid. In this case, the liquid/solid interface is supposed to lie on a horizontal plane as it is observed in Fig. 2.3.8a. It means that the equilibrium contact angle can still be determined by Young's equation. Secondly, the dissolution process greatly changes the geometry of the solid substrate at the triple line, while the surface and interfacial energies are not sensitive to substrate dissolution (Fig. 2.3.8b). In this view, the changes in the substrate geometry at the triple line can affect the measurement of contact angle, where the "apparent" contact angle obtained is only the part "above" the substrate plane ($(\pi\text{-}\theta_v)$ in Fig. 2.3.9), lower than the true angle θ_l formed at the solid/liquid/vapour junction [110]. The attaining equilibrium at the junction can be expressed by the relations given below [123]

$$\frac{\gamma_{sl}}{\sin\theta_v} = \frac{\gamma_{sv}}{\sin\theta_l} = \frac{\gamma_{lv}}{\sin\theta_s} \quad , \tag{2.3.4}$$

where θ_s, θ_l and θ_v are the equilibrium dihedral angles in the solid, liquid and vapour phases, respectively.

According to the calculation of Warren *et al.* [140], three stages with different time scales can be distinguished in dissolutive wetting: (i) non-reactive spreading ($t_1 \sim 10^{-2}$ s); (ii) substrate dissolution in the liquid ($t_2 \sim 10^2$ s); (iii) total equilibrium ($t_3 \sim 10^8$ s).

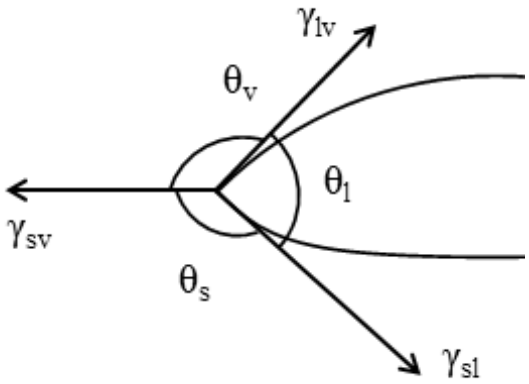

Fig. 2.3.9. Equilibrium configuration by dissolutive wetting with the change of substrate geometry (drawn after Ref. [110]).

b. Formation of a new compound at the interface

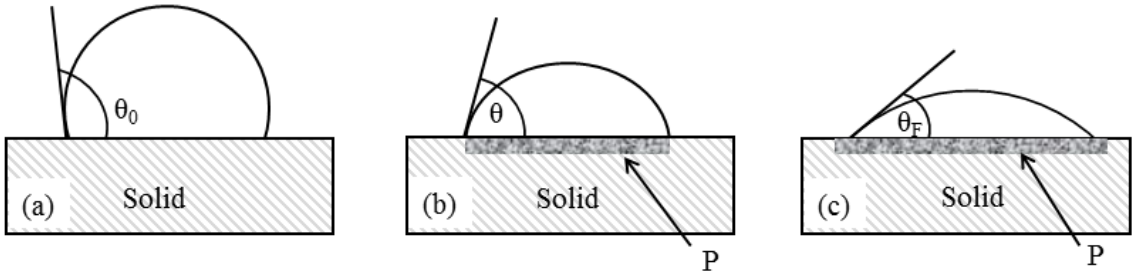

Fig. 2.3.10. Schematic illustrations of the RPC model: (a) initial contact angle θ_0; (b) quasi-state configuration; (c) final contact angle θ_F (drawn after Refs. [136, 141]).

Frequently, molten metal can react with ceramic to form a new compound layer, which then affects the wetting properties. The thermodynamics of reactive wetting with formation of a

new compound is described by the reaction product control (RPC) model [136]. According to this model, the initial contact angle θ_0 is the contact angle on the surface of unreacted substrate (Fig. 2.3.10a), which is formed in a few milliseconds. After a transient stage, a quasi-state configuration is established at the triple junction, since the advancement of liquid front is impeded by the presence of a non-wettable substrate at the triple line [2, 135] (Fig. 2.3.10b). Thus, lateral growth of the wettable reaction product *P* is the only way to make the liquid front move ahead until the macroscopic contact angle reaches a final value ($\theta_F \approx \theta_P$) (Fig. 2.3.10c). It has to be mentioned that in RPC model it supposes that the thickness of the reaction product layer is much smaller than the size of the drop used in the wetting experiments so that the layer does not affect the measurements of the apparent contact angle [112].

For reactive wetting with formation of a new compound at the interface, two cases should be considered depending on the wetting properties of the reaction product *P* and the original substrate *S*. In the first case, the reaction product formed at the interface is more wettable than the original substrate. Consequently, the contact angle on the reaction product θ_P is lower than that of the liquid on the original substrate θ_S ($\theta_S \approx \theta_0$) (Fig. 2.3.11). This has been verified by the sessile drop experiments in the Si/C system [142]. Liquid Si does not wet an unreacted carbon surface, but a good wetting is obtained due to formation of a continuous SiC layer at the interface [142]. In the second case, an opposite wetting situation occurs, where the reaction product acts as a barrier to liquid spreading, i.e. $\theta_P > \theta_S$. For example, in the Ag/SiC system, the reaction product (graphite) formed at the liquid/solid interface leads to a higher contact angle than that on the original SiC substrate [143]. It has to be mentioned that the new compounds formed at the interface play a major role in wetting behavior while the contact angle varies between two characteristic contact angles, i.e. the contact angle θ_0 formed on the initial unreacted substrate, and the final contact angle θ_F ($\theta_F \approx \theta_P$).

Figure 2.3.12 shows schematically contact angle kinetics of reactive wetting with formation of a new compound at the interface. The A-B and B-C stages represent the non-reactive wetting and formation of a new compound, respectively. The C-D stage corresponds to an equilibrium state when the liquid reaches a final contact angle on the reaction product. In some special cases, a C-D′ stage takes place at a long time. Such a drift in C-D′ stage might result either from modification of liquid composition (e.g. by evaporation or inter-diffusion with the solid at the interface) or from modification of the solid surface (e.g. by grain-boundary

grooving or wetting ridges via substrate dissolution). In some cases, θ_0 is much higher than θ_F, so that the A-B and B-C stages can be easily distinguished from the time scales (e.g. $t_0 \approx 10^{-2}$ s and $t_F \approx 10^2$-10^4 s) [112].

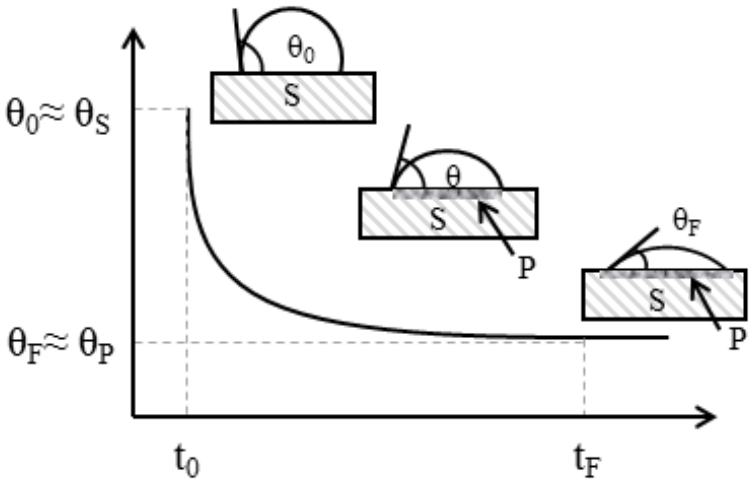

Fig. 2.3.11. Initial and final contact angles obtained in reactive wetting for the case $\theta_S > \theta_P$ (drawn after Refs. [143, 144]).

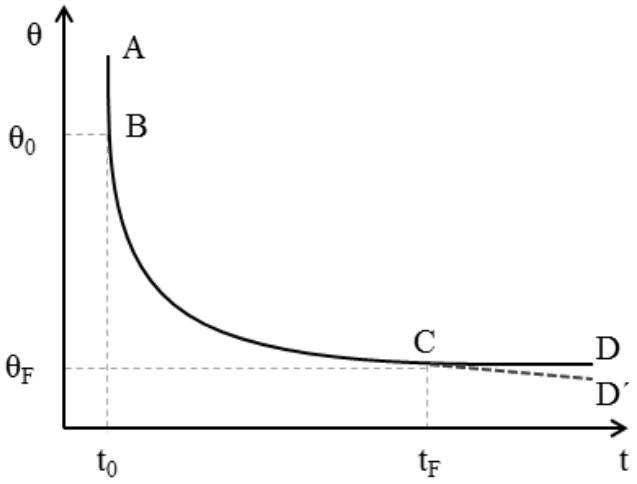

Fig. 2.3.12. Schematic contact angle versus time in reactive wetting with formation of a new compound at the interface (drawn after Ref. [112]).

Chapter 3: Materials and methods

3.1 Sample preparation

3.1.1 Alloys

The Ti-Al, Ni-Al and Ni-B samples used in this thesis were fabricated in various shapes such as ingots, rods and ribbons, depending on the experiments. The master alloys were prepared on a water-cooled copper substrate by arc-melting (Edmund Bühler GmbH) from proper quantities of high-purity elements (Table 3.1.1). Before heating, the chamber was evacuated to a vacuum level of about 10^{-4}-10^{-5} mbar and then it was constantly flushed with argon at a pressure slightly below 1 bar. The ingots were turned over and re-melted for three times to ensure their homogeneity. The rods with a diameter of 5.0 mm and a length of 75 mm were prepared by centrifugally casting (Linn High Therm GmbH) in a graphite mold from the master alloys.

Table 3.1.1. Elements used for sample preparation in this work

Elements	Al	Ti	Ni	B
Purity (%)	99.999	99.99	99.97	99.5

It is known that preparation and liquid state investigations of the alloys containing Al and refractory metals such as Ti-Al and Ni-Al alloys is difficult due to a large difference in the melting temperature of the constituents and evaporation of Al above 1000 °C [145-149]. Therefore, we have determined the concentration of the as-prepared binary samples. However, it was not possible to measure the compositions of the alloys after the high-temperature wetting tests since they spread over the substrates. Instead, we have estimated the alloy concentrations from the sample weight loss assuming that only the evaporation of Al occurred. The exact alloy compositions studied in this work are listed in the corresponding chapters, where the experimental results are presented.

3.1.2 TiB_2 substrates

TiB_2 substrates used for the sessile drop tests were cut in form of rectangular plates (12 mm × 10-12 mm) with a thickness of × 1-2.5 mm by electric discharge machining. The density was measured by the Archimedes method using dodecane as the immersing medium at room temperature. The measure density is about 4.46±0.02 g/cm^3, which is ~ 98.7% of the theoretical density [29]. The X-ray diffraction patterns of TiB_2 ceramic are shown in Fig. 3.1.1. The XRD patterns correspond to a typical hexagonal unit cell with a space group *P*6/mmm.

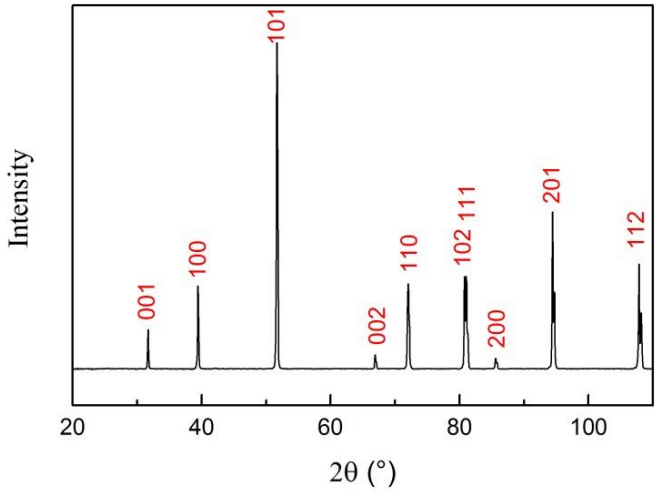

Fig. 3.1.1. X-ray patterns of TiB_2 ceramic.

A scanning electron microscopy (SEM) image of a dense microstructure with a grain size of 10-20 μm is well seen, which was taken at the fracture surface of a broken TiB_2 plate, as shown in Fig. 3.1.2a. Only a few TiC_x particles (white phase) found between the grains presumably originate from carbon or boron carbide commonly used for synthesis of TiB_2 ceramic [29, 89]. As TiB_2 is very hard and abrasive in nature, the pressure on the disks and polishing time during grinding and polishing should be moderate to avoid cracks or release of the weak bonded grains. The TiB_2 substrates were grounded and polished using MD-system disks from Struers A/S (Ballerup, Denmark) and suspensions from Buehler (IL, USA). The final polishing has been successfully achieved with colloidal silicon dioxide of fine grit of 0.04 μm on a synthetic leather cloth. This suspension can also act as a weak etchant. The final roughness of the polished TiB_2, measured using scanning probe microscopy (SPM), was about 0.1 μm. The morphology of the surface of a polished TiB_2 examined by SEM is shown in Fig. 3.1.2b.

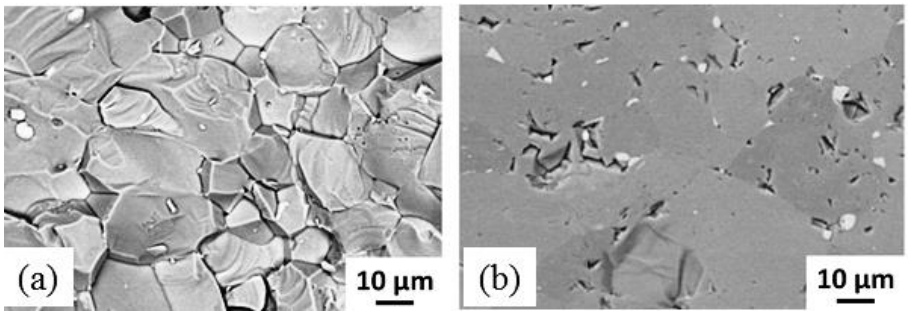

Fig. 3.1.2. SEM images of a fracture surface for a broken TiB_2 ceramic (a), the surface of a polished TiB_2 plate (b). The polished TiB_2 surface show pores and holes due to detachment of grains during mechanically polishing.

3.2 The sessile drop method

In this work, the wetting experiments were carried out using two different techniques: (i) classical sessile drop; (ii) dispensed drop.

3.2.1 Classical sessile drop technique

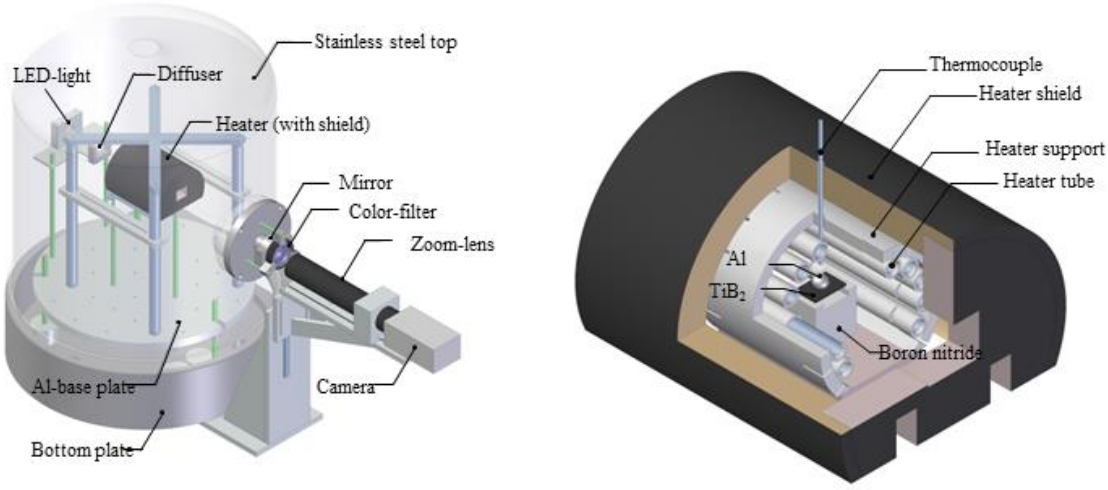

Fig. 3.2.1. Schematic illustrations of experimental instrument used for the classical sessile drop test [150].

The classical sessile drop tests with contact heating up to the temperature of 1250 °C were carried out at the IFW Dresden in the device described in detail in Ref. [150]. The

experimental setup schematically shown in Fig. 3.2.1 consisted of a horizontal resistance furnace inside a stainless steel water-cooled wall chamber with illumination and observation windows, sample illumination and an optical system with a charge-coupled device (CCD) camera. The sample/substrate couple was placed on a boron nitride support which was situated in the middle of a molybdenum resistance furnace in a horizontal position. Before heating, the chamber was evacuated to about 2.0×10^{-4} mbar. The sample/substrate couple was heated together from room temperature up to a set temperature with a rate of 10 K min^{-1}. The experimental temperature was measured by a thermocouple located directly above the sample. Digital photographs of the drop/substrate couple were taken in steps of 10 K during heating and cooling processes.

3.2.2 Dispensed drop technique

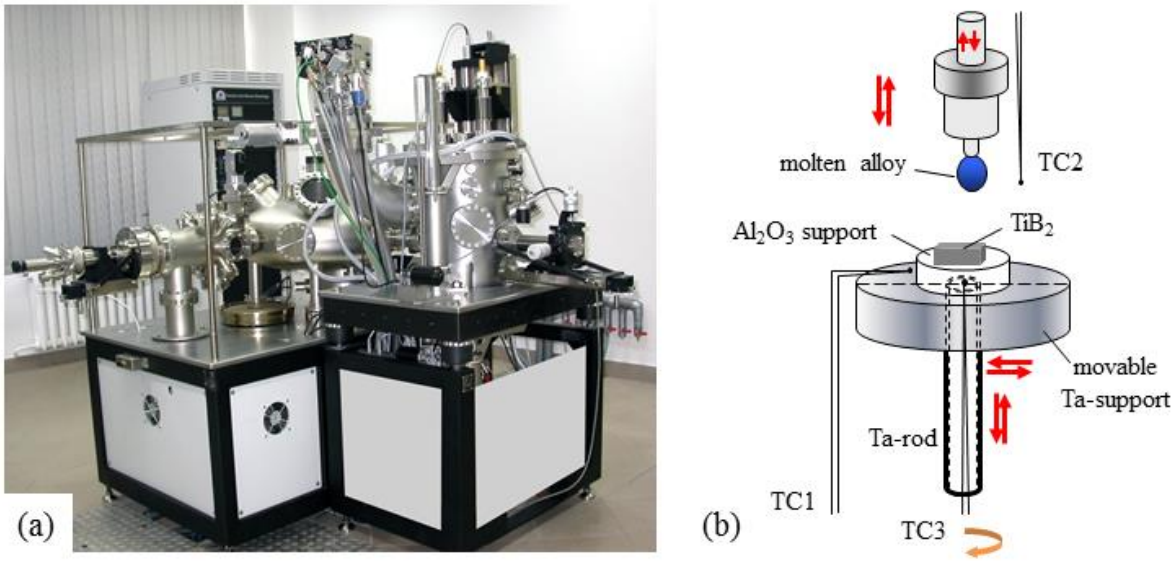

Fig. 3.2.2. Experimental complex for high-temperature studies (a) and schematic view of the movable elements allowing the test by the dispensed drop technique (b) (courtesy of Prof. N. Sobczak [116]).

The sessile drop experiments with dispensed drop technique were performed using the experimental complex at the Foundry Research Institute in Cracow (FRI Cracow), described in Ref. [151] and shown in Fig. 3.2.2. The following parts are included [116, 151]:

(1) Vacuum chamber for the first stage of sample preparation by preheating under vacuum at the temperature of up to 200 °C in order to remove the adsorbed gases on the surface of samples;

(2) UHV chamber for transferring the samples between the chambers by a manipulator which allows moving the samples of different sizes and shapes;

(3) Analytical chamber involves:

(a) Auger spectroscope for characterizing the surfaces of examined materials before and after high-temperature processing,

(b) Ion beam for etching/cleaning samples and for removal of surface films from examined samples;

(4) Portable vacuum chamber for collecting samples after testing;

(5) Experimental chamber for high-temperature studies of materials in different states.

The high-temperature chamber is main part of the experimental complex. It consists of a stainless-steel vessel equipped with a tantalum resistance furnace, illumination and observation windows, and an optical system with a sample illumination as well as a charge-coupled device (CCD) camera. Here, a high speed camera (up to 2000 frames per second) was used for direct visualization of the spreading of liquid metal on the substrate. It was also equipped with a quadrupole residual gas analyzer to allow recording the chemical composition of chamber atmosphere, as well as special manipulators built for an up- and down- movement of both a ceramic support and a drop-dispenser filled with molten metal. The wetting tests can be done in a wide temperature range (up to 2100 °C) to examine high-melting temperature materials under high vacuum or in protective atmosphere where static or flowing gas at a controlled rate and pressure level can be operated. High vacuum (10^{-7}-10^{-10} mbar) of the chamber can be reached by turbo-molecular and ionic pumps. The real-time control of temperature was regulated with three thermocouples located close to and below the substrate (TC1 and TC3), and close to the drop dispenser (TC2), respectively (Fig. 3.2.2b).

The experimental complex offers advantages with respect to traditional sessile drop technique [116, 151]. The complex is possible to fully computerize controlling and recording system to work on each unit independently. This experimental complex combines several apparatuses for high-temperature investigations of complex materials by various testing

procedures to record high-temperature wetting phenomena and estimate different characteristics in one test simultaneously.

Before the wetting experiments, the metal sample was inserted into an alumina drop dispenser, which was situated above a TiB_2 substrate sitting on an alumina support. This assembly was situated in the middle of a vertical tantalum resistance furnace placed in a stainless steel chamber. Before heating, the chamber was evacuated to a vacuum level of about 10^{-7} mbar. After heating to 500 °C, it was filled with high-purity argon (99.999 %). The flowing gas pressure was always kept in the range of 850–900 mbar during the experiments. After the temperature was stabilized at a given value, a metal drop was squeezed out of the alumina drop dispenser from a small hole ($\psi \approx 2.9$ mm) onto the substrate and thus the sessile drop test was started. Manipulation with the substrate and drop dispenser as well as the wetting behavior of drop on the substrate either at isothermal or time-dependent heating at a constant rate was registered by a high-speed/high-resolution CCD camera connected to a computer. In this way, the processes of melting and spreading were separated. The wetting tests with Ti-Al and Ni-B alloys were carried out in the contact heating mode using the experimental complex at the FRI Cracow due to the high experimental temperature.

After the sessile drop experiments, the digital images of the sessile drop were analyzed using DROP [150] and ASTRA-View [117] software to determine the contact angles. Contact angles were determined at the left and the right sides of the drop and acquired with an accuracy of about ±2°. The total uncertainty of the mean contact angle was estimated to be less than ±5°.

3.3 Characterization: microstructure and phase identification

The microstructure of primary alloys and solidified metal/ceramic couples after wetting tests was characterized using optical microscopy (OM) and to a larger extent scanning electron microscopy (SEM). Furthermore, X-ray computed tomography (X-ray CT) was used for acquiring a 3D image of a metal/ceramic couple. The composition and phase analysis of these samples were determined using energy dispersive X-ray spectroscopy (EDX) and X-ray diffraction (XRD).

3.3.1 Scanning electron microscopy (SEM/EDX)

In this thesis, microstructure characterization was carried out using a high-resolution scanning electron microscope (Gemini 1530, Zeiss). In order to well distinguish from different phases, backscattered electron (BSE) SEM images were obtained based on the atomic number of various phases appearing in different contrasts. Secondary electron (SE) mode was used to take advantage of the large depth of focus. The SEM was equipped with an energy-dispersive X-ray spectrometer (Bruker XFlash Detector 4010) to determine the chemical composition and phases of the measured samples. The EDX analysis was performed at the voltage of 5 keV for a better detection of the light elements, i.e. boron, carbon and oxygen, as well as at 20 keV for metallic elements. For this purpose, metal/ceramic couples were cross-sectioned by an automatic cutting machine using a Buehler Diamond Wafering Blade and embedded into epoxy resin. The cross sections were grounded and polished using successively different MD-system discs from Struers A/S and suspensions from Buehler. It has to be mentioned that the inherent difficulties in grinding and polishing multiphase structures with greatly different properties demand high attention to the preparation of cross sections.

3.3.2 Optical microscopy (OM)

For a better characterization of the microstructure, an optical microscope (Epiphot 300) was also employed for low-magnification observation. The microscope enables to observe the samples using different objective lenses from 5 X until 100 X and is connected to a computer program so that the images can be simultaneously recorded.

3.3.3 X-ray computed tomography (CT)

X-ray CT can reconstruct a 3D image of a scanned object from a large number of 2D projections recorded from different angles and provide non-destructive visualization and characterization of the object. After processing the acquired data the maximum image quality is obtained and the total volume is reconstructed. In this thesis, X-ray CT (Phoenix nanotom m, GE) was used to examine the morphology of a solidified metal/ceramic couple in order to have a better understanding of the wetting and high-temperature interactions.

3.3.4 X-ray diffraction (XRD)

X-ray diffraction is one of the most commonly used technique to characterize the structure of materials via non-destructive testing [152]. Each crystalline solid generates a unique diffraction pattern that comprises sharp peaks at the angles which satisfy the Bragg condition. In this thesis, X-ray diffraction was used to identify the phases for the master alloys as well as for the solidified metal/ceramic couples after the sessile drop tests. XRD was carried out using a D3290 Panalytical X'pert PRO diffractometer with Co-K_α radiation. It was operated at a voltage of 40 kV and a current of 40 mA in a continuous scan mode over a range of diffraction angles 2θ = 20-110°. The measured XRD patterns were analyzed using PANalytical's HighScore Plus software [153] and ICDD PDF-4+ database [154].

3.4 Characterization of physical and mechanical properties

Before the sessile drop tests, the liquidus and/or melting temperatures of primary alloys were measured by differential scanning calorimetry (DSC) in order to set the experimental temperatures for the wetting tests. The coefficients of thermal expansion of primary alloys were experimentally measured in order to discuss the thermomechanical compatibility of the metals and TiB_2 ceramic.

3.4.1 Differential scanning calorimetry

The liquidus and/or melting temperatures of primary alloys were determined using a differential scanning calorimeter (NETZSCH 404C) in flowing argon atmosphere. The DSC measurements were performed using an Al_2O_3 crucible. Small amount of Y_2O_3 powder was put at the bottom of the crucible to avoid chemical reactions between liquid alloy and Al_2O_3 crucible, particularly for high-temperature measurements of Ti-containing alloys. Determined by the experimental conditions, the upper temperature limit was 1490 °C for all the alloys. The alloy with a weight of 10-15 mg was heated up to a given temperature and cooled to room temperature with a rate of 20 K min^{-1}.

3.4.2 Dilatometry

Dilatometry is a method which precisely measures the dimension changes of a sample at a programmed temperature change and with a negligible load. The coefficients of thermal expansion (CTEs) were determined by measuring the displacement induced when strain-gauge instrumented samples were heated in a temperature range from room temperature to a set temperature.

The CTEs measurements were carried out using a NETZSCH DIL 402C dilatometer. Before the measurements, the as-cast rods were cut to a length of about 25 mm and both the top and bottom of the rod specimens were carefully polished to guarantee plane-parallel surfaces. The CTE measurements were carried out at a constant heating and cooling rate of 10 K min^{-1} in argon atmosphere. Determined by the experimental conditions, the upper temperature limit was 500 °C for the Al-rich alloys and 800 °C for the Ti- and Ni-rich alloys. For elimination of systematic errors, calibration was done using a silica standard under the same conditions.

Chapter 4: High-temperature wetting and interfacial interactions in Al/TiB_2 system

This chapter presents the study of wetting behavior and interfacial interactions between liquid Al and TiB_2, published in Journal of Materials Science [129]. As available literature data on the Al/TiB_2 system is rather scattered due to measurements either at a limited temperature range or even at one temperature, the high-temperature wetting of TiB_2 ceramic by molten Al at different temperatures was systematically investigated in this work. For the first time we have carried out the sessile drop measurements up to very high temperature (1400 °C) and established temperature-time dependent wetting behavior in the Al/TiB_2 system. The results of Al/TiB_2 system are important for further investigations of the high-temperature interactions of molten Al-containing metallic alloys such as Ti-Al and Ni-Al with TiB_2 ceramic in a view of grain refining or matrix reinforcing.

4.1 Introduction

High-temperature interaction in the Al/TiB_2 system has been investigated in various works so far. A good wetting of TiB_2 by liquid aluminum has been generally reported but the contact angle values as well as the temperatures are very scattered. Infiltration of liquid Al into TiB_2 ceramic materials and its reaction with impurities or additives have been studied in dependence on contact time for the temperature between 960 and 980 °C [66-69]. It has been reported in [66] that porous TiB_2 (90 % theoretical density) is rather fast penetrated by liquid Al (> 1 mm/day) at 970 °C, while dense TiB_2 (96 % density) is penetrated at a much slower rate (> 0.1 mm/day). Depending on time as well as the quality of TiB_2 or TiB_2-based materials, liquid Al penetrates either pores or pore-free grain boundaries (edges as well as faces) as it is established in [67-69].

The aim of the present work is to have a systematic study of the temperature- and time-dependent wetting phenomena between liquid Al and TiB_2 ceramic over a wide temperature range using the sessile drop method. Application of the drop dispenser technique enables essential minimization of the effects associated with oxidation of molten Al. Knowledge of the wetting and interfacial interactions in the Al/TiB_2 system at high temperatures is important for

the development/optimization of the Al-base lightweight alloys casting using TiB_2 grain refining. The high-temperature data on wetting, penetration and phase formation at the Al/TiB_2 interface are also required for the successful development of TiB_2-reinforced Al matrix composites by liquid infiltration processing.

4.2 Experimental results and discussion

4.2.1 Wetting upon constant heating

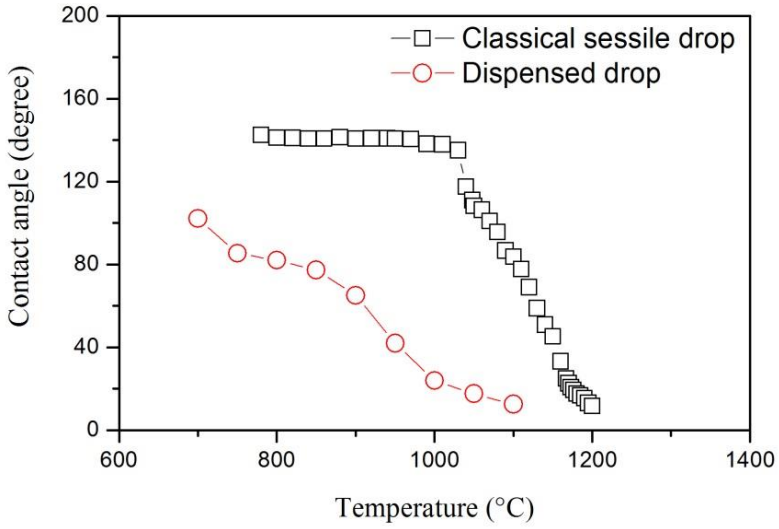

Fig. 4.2.1. Temperature dependence of the contact angle for liquid Al on TiB_2 ceramic measured by classical sessile drop (*black rectangles*) and dispensed drop (*red circles*) techniques.

Figure 4.2.1 shows the wetting behavior for liquid Al on TiB_2 ceramic upon constant heating rate of 10 K min^{-1}. In the classical sessile drop experiment (black rectangles in Fig. 4.2.1), a liquid drop is observed to be formed when the temperature reaches about 780 °C (Fig. 4.2.2a), which is significantly above the melting temperature of pure Al (660 °C). The apparent contact angle at the Al/TiB_2 interface of about 140° remains virtually unchanged up to about 1000 °C. Then it starts to decrease slightly and exhibits a steep decrease from 135° to 12° in the temperature range between 1030 and 1200 °C. On the contrary, liquid Al squeezed out from the alumina drop dispenser at 700 °C (i.e. capillary-purified) exhibits a significantly better wetting of

TiB_2 ceramic (red circles in Fig. 4.2.1). The contact angle reaches about 85° at 750 °C and decreases to 24° upon heating to 1000 °C, followed by continuous decrease to 12° at 1100 °C (Fig. 4.2.2b).

It is well known that Al has a very strong affinity to oxygen. It oxidizes very fast in the solid state at room temperature and the oxidation rate significantly increases with heating and time [155, 156]. However, upon melting and heating to about 1000 °C, the oxide layer has been reported to disappear due to the formation of gaseous Al_2O by a chemical reaction between liquid Al and solid Al_2O_3 [70]. This explains the behavior of the Al sample in the classical sessile drop experiment. Although oxides were mechanically removed from Al sample just before inserting it into the chamber, there was enough time to form a surface oxide afterwards. The onset of wetting of TiB_2 is observed at about 1030 °C (Figs. 4.2.1 and 4.2.2) after the ‘‘self-cleaning’’ of the liquid Al surface. A similar effect has been reported for the Al/Al_2O_3 system in Ref. [157].

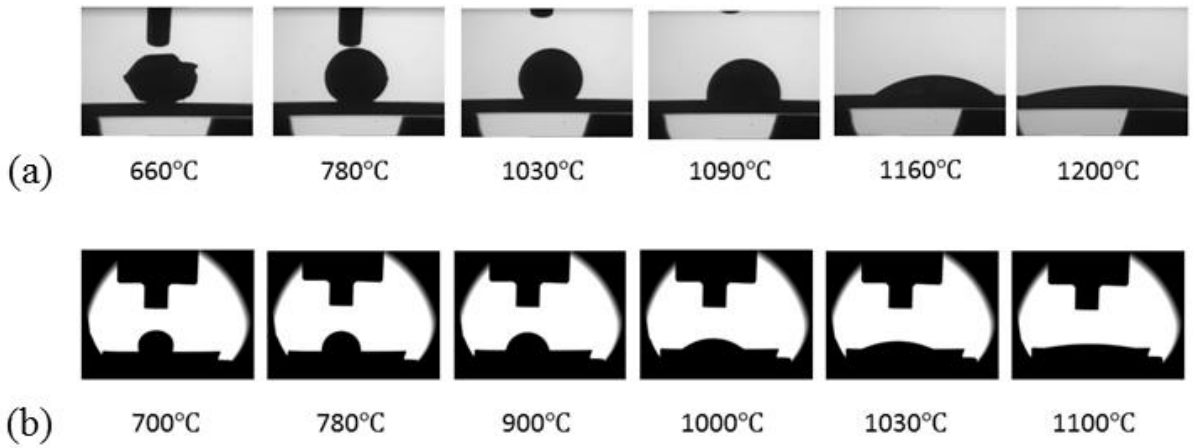

Fig. 4.2.2. Visualization of the wetting behavior of Al drop on TiB_2 ceramic during the sessile drop tests measured by classical sessile drop (a) and dispensed drop (b) techniques.

As the oxidation rate of liquid Al strongly depends on the oxygen partial pressure [158], it can be assumed that the Al drop squeezed out of the drop dispenser is free of oxides at least at the moment of the sessile drop test in the chamber evacuated to about 10^{-7} residual air pressure. This explains the essentially different wetting behavior for the ‘‘capillary-purified’’ liquid Al on TiB_2 ceramic (Fig. 4.2.1) and demonstrates the advantage of this technique. Mechanical removal of surface oxide(s) coupled with using well-purified inert atmosphere enables the wetting of

liquid Al on TiB_2 to start at a significantly lower temperature. A similar behavior has been reported for liquid Al on the Al_2O_3 substrates [52], where initial contact angles of ~ 130° and of ~ 94° were observed in a classical sessile drop test and in a dispensed drop test at 700 °C, respectively.

4.2.2 Wetting upon isothermal heating

The isothermal wetting kinetics of liquid Al dispensed on the TiB_2 substrates at different temperatures is presented by the time dependence of the contact angle in Fig. 4.2.3a. Liquid Al shows rather poor wetting of the TiB_2 substrate at a relatively low temperature. For example, the average contact angle reached about 90° after 2 h of isothermal annealing at 710 °C (Fig. 4.2.4a). The wetting is slightly improved at 800 °C, i.e. the mean contact angle decreased from the initial value of θ_0 = 128° measured immediately after the drop dispensing to a final contact angle of θ_F = 77° after 2 h of isothermal holding (Fig. 4.2.3a). However, with further increasing temperature, capillary-purified aluminum exhibits a very good wetting of TiB_2 ceramic followed by a spreading over the substrate within about 20 min at 900 °C, 1 min at 1100 °C, and 20 sec at 1300 °C (Figs. 4.2.3a and 4.2.4b).

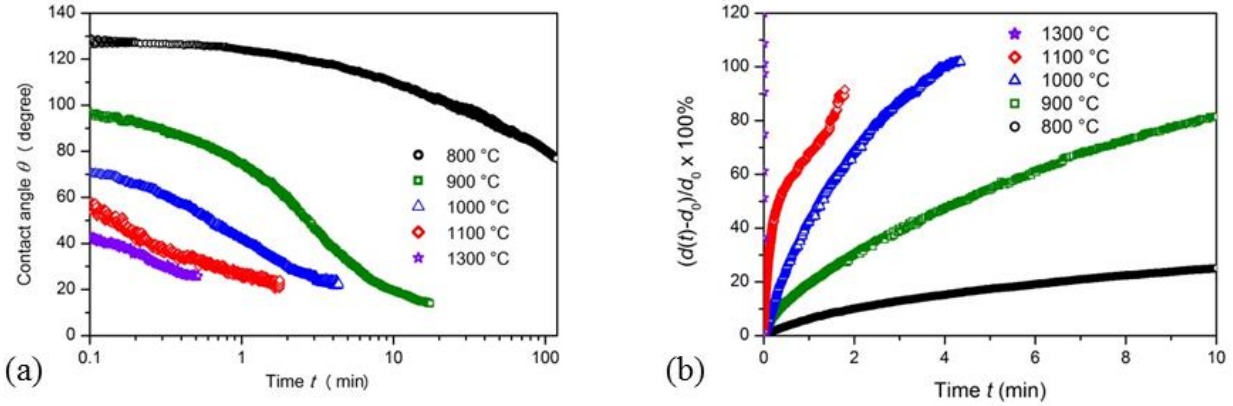

Fig. 4.2.3. Isothermal wetting kinetics for the dispensed Al drop on the TiB_2 substrates at different temperatures: (a) in situ measured contact angle θ versus time; (b) relative change of the drop base diameter d with time t at different temperatures (d_0 is the drop base diameter just after the drop deposition).

Images of the Al/TiB_2 couples after the isothermal holding at 800 °C and at 1000 °C are shown in Fig. 4.2.5. Starting at 1000 °C, the Al melt perfectly wets, spreads and streams down along the substrate walls and penetrates a gap between the TiB_2 plate and the Al_2O_3 support, which indicates that both ceramics are completely wetted by liquid Al at a high temperature. The cross sections of the Al/TiB_2 couples after the isothermal sessile drop tests carried out at 800, 900 and 1400 °C are presented in Fig. 4.2.6. On these SEM images, the contact angles correspond to the solidified drops and they are somewhat smaller than the contact angles measured in the sessile drop tests (plotted in Fig. 4.2.3a). This is due to the shrinkage of the adhered Al drop upon cooling and solidification. Fig. 4.2.6c also show that due to a relatively large volume of Al remaining on the TiB_2 substrates the apparent contact angle is much larger than zero, although liquid Al completely wets the ceramic.

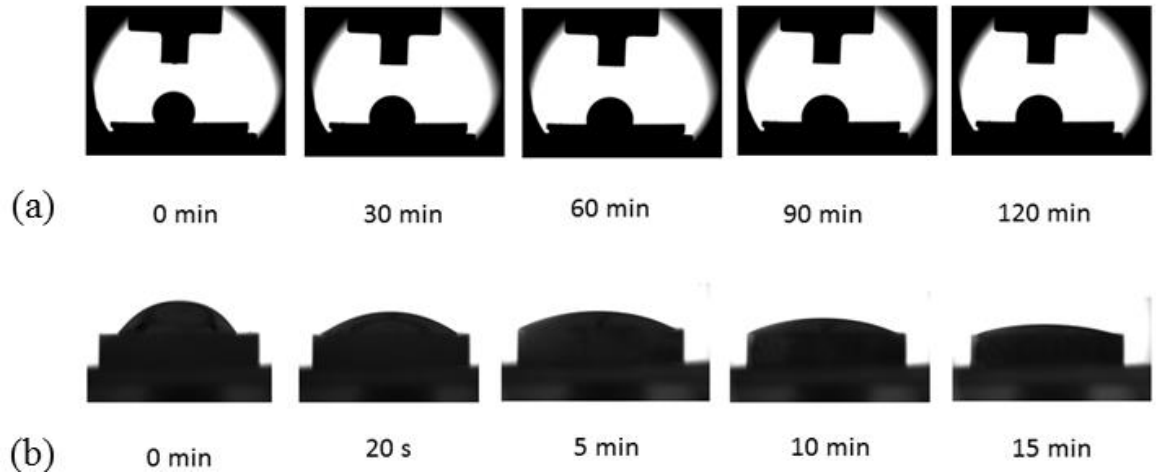

Fig. 4.2.4. Visualization of the wetting behavior of Al drop on TiB_2 ceramics during the sessile drop tests measured by dispensed drop technique at 710 °C (a) and 1300 °C (b), respectively.

The dynamics of molten Al spreading on the TiB_2 substrate is presented in Fig. 4.2.3b by the relative change of the drop base diameter d with time t at different experimental temperatures $(d(t) - d_0)/d_0$ (d_0 is the drop base diameter just after the drop deposition). For clarity of presentation, only the data for the first 10 min are shown here. There is a change in the spreading behavior when the temperature increases up to 1100 °C. After the initial rapid spreading within the first 10 sec, the spreading rate reduces. A similar transition from the fast to a relatively slow spreading rate is also observed at higher temperatures, but in much shorter time interval, e.g.

about 2 sec after the drop deposition at 1300 °C. This phenomenon is supposed to be caused by pinning of the triple line due to the penetration of molten aluminum into the TiB_2 substrate at the temperature above 1000 °C, discussed below.

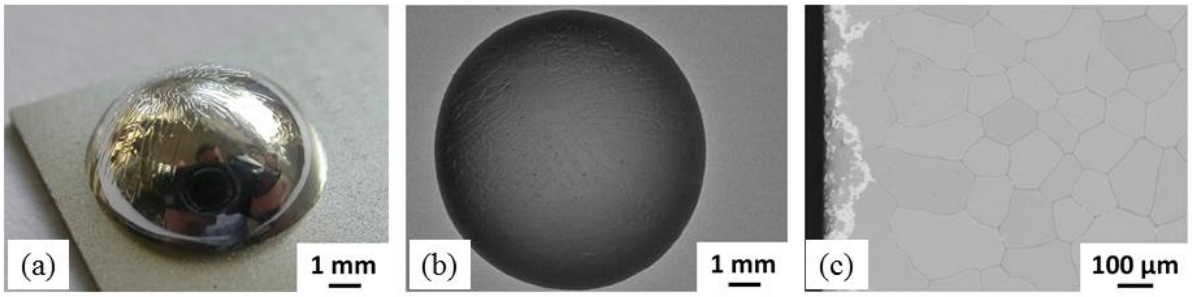

Fig. 4.2.5. Al/TiB_2 couples after isothermal sessile drop tests carried out for 2 h at 800 °C (a, b) and for 15 min at 1000 °C (c): a general-view photograph; b, c top-view SEM images.

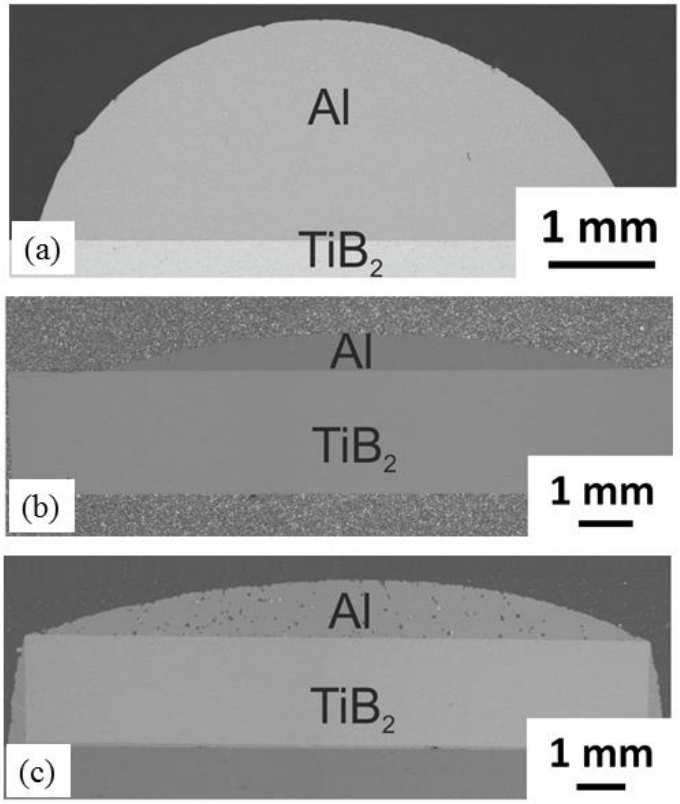

Fig. 4.2.6. SEM images of the cross-sectioned Al/TiB_2 couples after isothermal sessile drop tests carried out at different temperatures for different time: (a) 800 °C, 2 h; (b) 900 °C, 1 h; (c) 1400 °C, 15 min.

It is known that TiO_2 forms rather easily on the surface of monolithic TiB_2 at room temperature [29] and it can grow upon heating due to residual oxygen in the experimental chamber [159]. In this view, it is interesting to recall the works, where the wetting behavior of liquid Al on TiO_2 has been studied. For example, Avraham and Kaplan [160] reported the contact angle of about 150° for liquid Al on TiO_2 at 700 °C, which decreased to about 85° by heating up to 1000 °C. Sobczak *et al*. [161] found that the contact angle for capillary-purified molten Al on the TiO_2 substrate equals to 80° at 900 °C. In our study, liquid Al on the TiB_2 substrates exhibits a much better wetting (Figs. 4.2.1 and 4.2.3) and the final contact angles well agree with the results reported by Rhee [63]. This suggests that either the amount of Ti oxides on the surface of TiB_2 substrate was negligible or it is reduced by liquid Al. The latter is supposedly to be evidenced by appearance of the Al_2O_3 and Al_xTi particles at the Al/TiB_2 interface after the sessile drop tests carried out at temperatures from 710 to 1400 °C.

4.2.3 Penetration and interfacial reactions

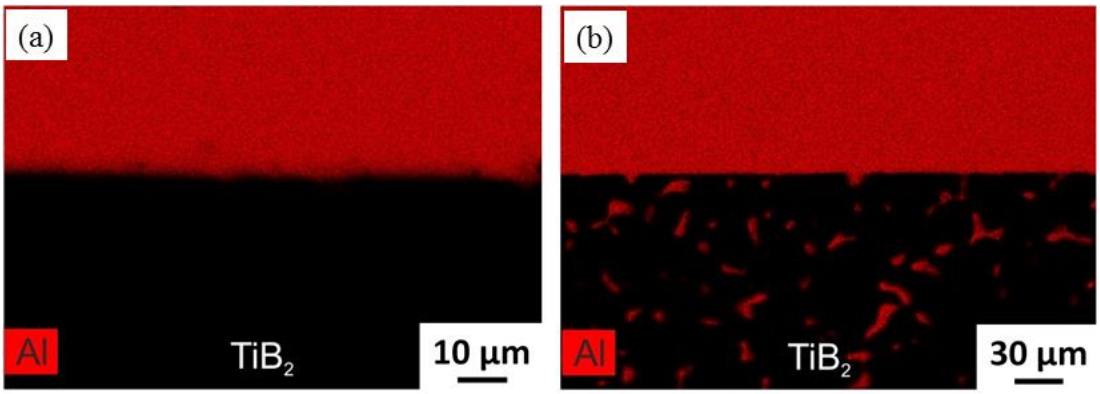

Fig. 4.2.7. SEM/EDX images of the Al/TiB_2 interface after isothermal sessile drop tests carried out for 2 h at 800 °C (a) and for 15 min at 1000 °C (b).

Magnified SEM images of the Al/TiB_2 interface are shown in Figs. 4.2.7, 4.2.8 and 4.2.9. The interfacial area between the TiB_2 substrate and the Al_2O_3 support filled by liquid Al at 1000, 1300, and 1400 °C is shown in Fig. 4.2.10. The Al/TiB_2 interface is smooth and planar for all solidified couples. Aluminum and TiB_2 phases are distinctly separated in the couples kept at 710 °C, 800 °C and 900 °C. A sharp interface is also observed for the Al/TiB_2 couples tested at 1000 °C (Fig. 4.2.7b) and even at 1400 °C (Fig. 4.2.8). However, in these cases, Al is found in

the TiB_2 ceramic either in the pores, as it can be seen in Fig. 4.2.7b (1000 °C), or at the grain boundaries, as seen in Fig. 4.2.8 (1400 °C). In general, these observations correlate with investigations performed at 960-980 °C [66-69] and show that the penetration rate rapidly increases with increasing temperature. The average penetration depth extends up to about 250 μm after the sessile test carried out for 15 min at 1400 °C.

TiB_2 ceramic and Al are characterized by quite different coefficients of thermal expansion: $\alpha_{TiB2} = (6.7 – 8.2) \times 10^{-6}$ K^{-1} in the temperature range between 20 °C and 1000 °C given by ESK Ceramics [88], while $\alpha_{A1} = (20.9 – 33.7) \times 10^{-6}$ K^{-1} between 20 °C and 500 °C (own measurements). Because of this, cracking of TiB_2 grains has been observed in the near interfacial area of the substrates penetrated by liquid aluminum, as it is depicted in Fig. 4.2.8b.

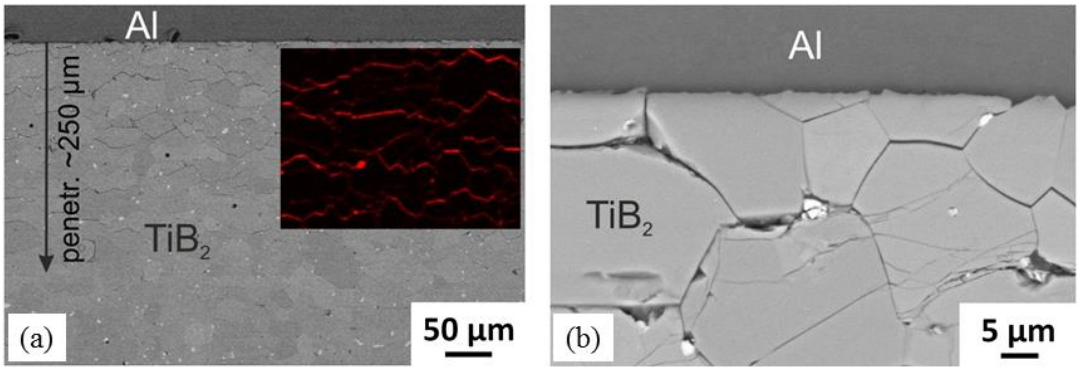

Fig. 4.2.8. Aluminum penetration along the TiB_2 grain boundaries at 1400 °C: SEM images of the Al/TiB_2 interface. *Inset* in panel (a) shows an enlarged SEM/EDX map of Al distribution in a near interface area. Panel (b) illustrates micro-cracks in TiB_2 grains.

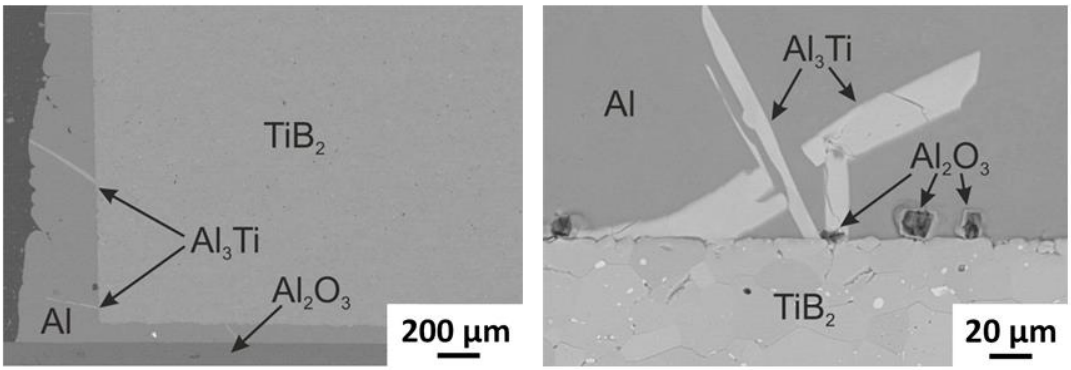

Fig. 4.2.9. SEM images of the Al/TiB_2 interface after isothermal sessile drop tests carried out for 15 min at 1400 °C. Al_3Ti and Al_2O_3 phases are marked.

As it has been mentioned, Al-rich Al_xTi particles were observed by SEM/EDX at the Al/TiB_2 interface after the sessile drop tests carried between 710 and 1300 °C. The composition of these particles is very uncertain for low temperatures, whereas after testing at 1400 °C the stoichiometric Al_3Ti phase (melting temperature T_m = 1396 °C [85]) with needle-like structure has been found to precipitate at the Al/TiB_2 interface and to grow into the molten aluminum (Figs. 4.2.9 and 4.2.10). At the same time, SEM analysis suggests that TiB_2 grains remain undissolved in all experiments, in agreement with a very low solubility of TiB_2 in liquid Al [85]. Therefore, it can be supposed that the Al_xTi particles are formed due to the chemical reaction of liquid Al with TiO_2 existing on the surface of the TiB_2 substrate or with TiC_x particles found in the TiB_2 ceramic. We have also observed Al_2O_3 particles at the Al/TiB_2 interface in the samples after the tests carried out at 710–1400 °C, as it can be seen in Fig. 4.2.9 for the temperature of 1400 °C. This is in line with the reports on high-temperature interactions between liquid Al and TiO_2 [160-165] and formation of Al_2O_3 particles and Ti dissolved in Al by the reduction reaction:

$$4Al + 3TiO_2 = 2Al_2O_3 + 3Ti, \quad (4.2.1)$$

Hence, the reaction mechanism in our study can be described as follows. Liquid Al placed on the TiB_2 substrate initially interacts with TiO_2 surface oxide. Al_2O_3 crystals nucleate at the drop/substrate interface and grow inside the drop, whereas pure Ti is released into the molten Al, similar to that observed in the Al/TiO_2 couples at 900, 1000 and 1100 °C in work [161]. Upon cooling, Al_3Ti phase precipitates at the Al/TiB_2 interface.

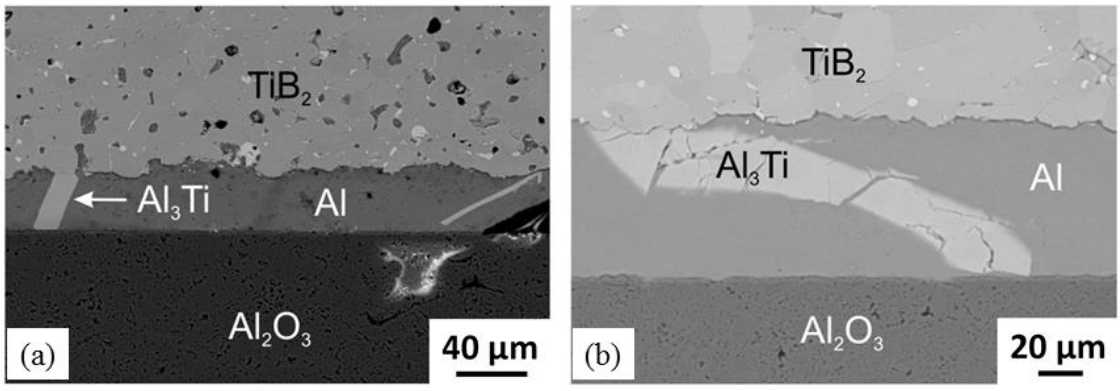

Fig. 4.2.10. Aluminum-filled gap between the TiB_2 substrate and the Al_2O_3 support after the sessile drop tests carried out for 15 min at (a) 1000 °C and (b) 1400 °C.

The very few Al_4C_3 and $(Al,Ti)_xC$ particles detected at the Al/TiB_2 interface after the sessile drop tests carried out at 710–1400 °C (not shown) as well as the very few Al_xTi particles found in the pores of the TiB_2 substrates are supposed to be formed due to reaction of molten Al with TiC_x impurities. This is in a good accordance with the Al–Ti–C phase diagram [166] and the high-temperature interaction between liquid Al and TiC ceramic [167]. It means that no reaction between liquid Al and TiB_2 has occurred. XRD patterns (Fig. 4.2.11) also prove the absence of any reaction product in all couples. It is interesting that Al_3Ti plate-like crystals were found in the Al-filled gap between the TiB_2 substrate and Al_2O_3 support already in the experiments conducted starting from 1000 °C (Fig. 4.2.10). Probably, this is due to an enhanced oxidation of the TiB_2 surface contacting Al_2O_3 support upon heating and subsequent dissolution of TiO_2 in the liquid Al. The presence of Al_3Ti in the Al-filled gap at 1000 °C in our experiments correlates with the results reported in [163], where Al_3Ti plate-like crystals were formed in the Al–TiO_2 system after the tests carried out at 950 °C and higher temperatures.

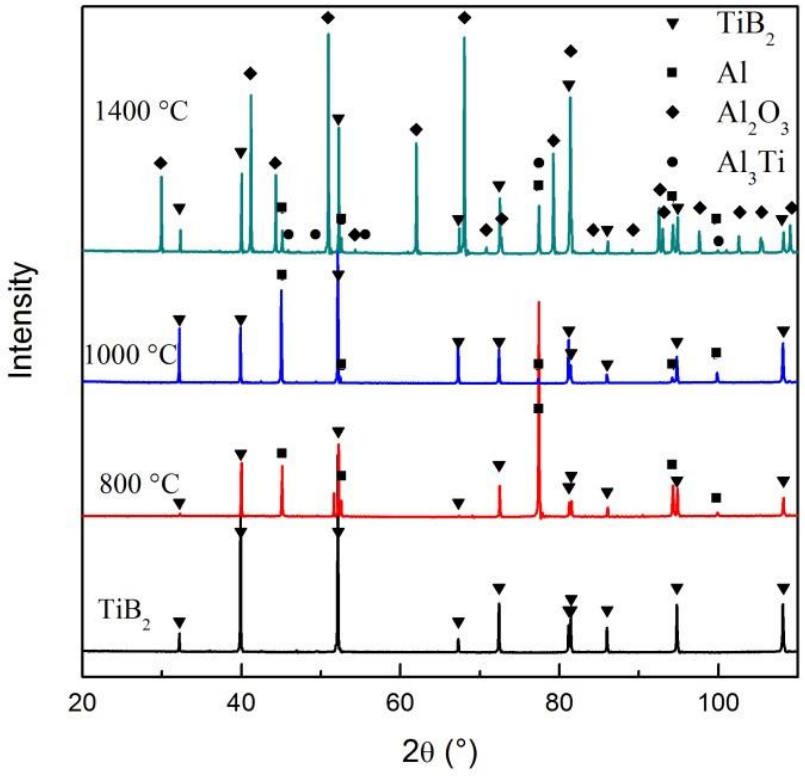

Fig. 4.2.11. XRD patterns for the polished TiB_2 substrate before the test and for the cross-sectioned Al/TiB_2 couples after the sessile drop tests.

4.3 Conclusions

The wetting behavior and interfacial interactions between liquid Al and TiB_2 ceramic have been studied by the sessile drop method in the temperature range from 700 to 1400 °C. For the classical sessile drop technique, the onset of wetting of TiB_2 by liquid Al is observed at a rather high temperature (1030 °C) after deoxidizing the surface of Al drop. Capillary-purified aluminum by the dispensed drop technique starts wetting of TiB_2 ceramic at about 750 °C. The wetting is notably improved by continuous heating. Complete wetting is observed after isothermal annealing at 1000 °C for about 8 min and is significantly accelerated with increasing temperature. The nature of the wetting in these systems may be attributed to the "metallic-like" character of TiB_2.

No reaction between liquid Al and TiB_2 has occurred. However, beginning from 1000 °C, liquid Al penetrates the TiB_2 substrates by filling the inter-grain pores as well as the grain boundaries at higher temperature. It extends up to about 250 μm after the sessile drop test carried out for 15 min at 1400 °C. Titanium aluminide Al_xTi, aluminum carbide Al_4C_3 and Al_2O_3 particles found at the Al/TiB_2 interface are supposed to originate from the reaction of liquid Al with TiO_2 and TiC_x impurities existing on the surface and in the bulk of TiB_2 ceramic.

Chapter 5: Interfacial interactions between liquid Ti, Ti-Al alloys and TiB_2 ceramic

High-temperature interactions of pure liquid Ti and Ti-Al melts with TiB_2 ceramic have been investigated by the classical sessile drop technique. This study which was reported in Journal of Materials Science [168], establishes a basic knowledge for preparation of Ti-Al based composite materials reinforced with TiB_2 particles.

5.1 Introduction

Titanium aluminides are characterized by a low density, notable high-temperature strength, high oxidation and corrosion resistance and are, therefore, very interesting for aerospace, automotive and other applications [169-182]. However, their properties, in particular their mechanical behavior, still require improvement. For example, Ti-Al intermetallics are brittle and have relatively low fracture toughness at room temperature, they show rapid grain coarsening at elevated temperatures, and their strength is relatively low at temperatures above 700 °C. To overcome the drawbacks, the development of TiAl-based composite materials, exploiting the combined potential of metallic alloys and ceramics with desirable balance of properties, has become one of the up-to-date trends.

Titanium aluminide intermetallic-matrix composites (IMCs) are a new class of engineering materials for high-temperature structural applications in aggressive environments [28, 183]. TiAl or Ti_3Al IMCs reinforced with ceramic particles possess even higher specific strength and specific stiffness, increased creep strength, improved toughness, and high-temperature strength retention over the monolithic intermetallic counterparts [28]. TiB_2 ceramic particles are often used as grain refiners or reinforcement in both aluminum and titanium alloys [59, 60, 77, 78, 184-186]. TiB_2 particles are especially interesting as grain reinforcements in TiAl alloys due to its high strength and comparable density [14, 187, 188]. Different routes for fabrication of TiAl-TiB_2 composites via liquid-state processing such as casting or laser melting, or via solid-state treatment such as hot pressing or spark plasma sintering are used. Chemical compatibility and interfacial bonding between a metallic matrix and ceramic inclusions play a crucial role in determining appropriate fabrication methods and mechanical properties of IMCs.

Therefore, wetting properties and interfacial interactions between liquid alloys and TiB_2 ceramic have to be studied in detail.

The wetting behavior of liquid Ti-Al alloys on oxide, nitride and carbide ceramics, such as ZrO_2 [189-191], Y_2O_3 [191], Al_2O_3, SiO_2, TiO_2, AlN, Si_3N_4, SiC [192], has been extensively investigated and reported. However, we are not aware about any report on the wetting behavior and interfacial interactions between Ti-Al melts and TiB_2 bulk ceramic, which are the focus of the present study.

5.2 Ti-Al alloy

The compositions of as-prepared alloys were $Ti_{74.3}Al_{25.7}$, $Ti_{49.3}Al_{50.7}$ and $Ti_{26.5}Al_{73.5}$ (at.%) as determined by EDX analysis (Table 5.2.1). The fourth studied alloy $Ti_{3.5}Al_{96.5}$ (at.%) was an extruded rod from KBM Master Alloys B.V. (Delfzijl, The Netherlands). For convenience, we denote the alloys as Ti-25Al, Ti-50Al, Ti-73Al and Ti-96Al in the following text.

Table 5.2.1. Concentration of Ti and Al in the studied Ti-Al alloys (at.%).

Alloy	T_{test}	As-cast samples		After sessile drop test	
	°C	Ti	Al	Ti	Al
Ti	1550	99.99	–	–	–
Ti-25Al	1650	74.3 ± 1.3	25.7 ± 0.8	76.3 ± 1.31	23.7 ± 0.81
Ti-50Al	1470	49.3 ± 1.5	50.7 ± 1.3	50.5 ± 1.51	49.5 ± 1.31
Ti-73Al	1385	26.5 ± 1.1	73.5 ± 1.7	27.0 ± 1.12	73.0 ± 1.72
Ti-96Al	1250	3.5 ± 1.5	96.5 ± 1.4	3.6 ± 1.51	96.4 ± 1.42

As-cast samples – measured by EDX, after sessile drop tests – estimated from the mass loss under assumption that only Al evaporates, T_{test} – temperature of the wetting test.

The microstructures of as-prepared alloys are characterized by SEM (Fig. 5.2.1). For the alloy Ti-25Al, it is consisted of α_2-Ti_3Al and Ti but it is quite difficult to be identified on the BSE SEM image. The alloy Ti-50Al contains γ-TiAl and α_2-Ti_3Al. For the alloy Ti-73Al, the main phases are $TiAl_3$ and pure Al, where Al is located at the boundaries of $TiAl_3$ while in the

case of extruded alloy Ti-96Al, spherical $TiAl_3$ phases are homogeneously distributed in the overall Al matrix.

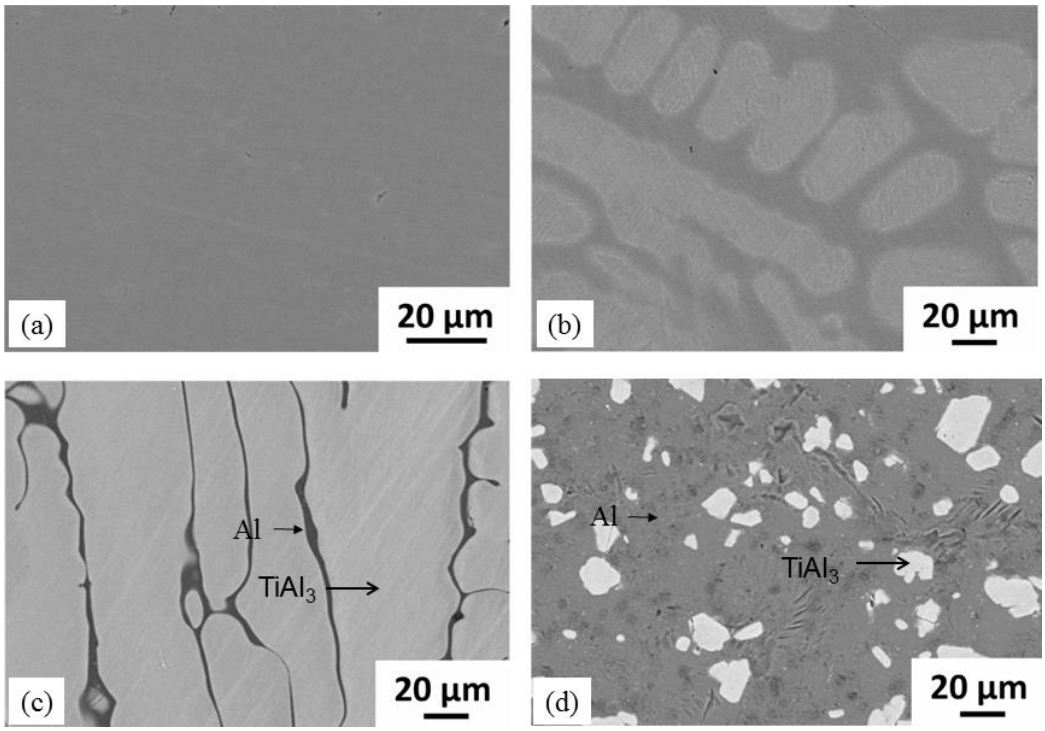

Fig. 5.2.1. SEM micrographs of the Ti-Al alloys used in the sessile drop experiments: (a) Ti-25Al; (b) Ti-50Al (*light grey*: Ti_3Al, *dark grey*: TiAl); (c) Ti-73Al (*grey*: $TiAl_3$, *black*: Al); (d) Ti-96Al (white: $TiAl_3$, grey: Al).

5.3 Results and discussion

5.3.1 Pure Ti/TiB_2 system

The high-temperature interaction between pure Ti and TiB_2 ceramic is clearly reflected in the shape and structure of the solidified Ti/TiB_2 couple (Fig. 5.3.1). A rectangular-shaped crater with a depth of about 200 µm is formed by melting of a cube-shaped Ti sample. It is well distinguished from a circle-shaped spread liquid drop on the top-view photograph and three-dimensional X-ray tomography image in Fig. 5.3.1a, b. An image taken from the cross-sectioned Ti/TiB_2 couple (Fig. 5.3.1c) further elucidates the crater as well as a complete wetting of the TiB_2 substrate by the liquid, which occurs within about 30 sec after incipient melting.

It is noteworthy that a solid Ti sample heated on a TiB_2 substrate showed an incipient melting at about 120 °C below the melting point of Ti of 1668 °C [148]. A similar apparent decrease in the melting temperature of Ni revealed for the Ni/HfB_2 and Ni/TiB_2 couples in the sessile drop tests was explained by the solid state diffusion of B into Ni resulting in the formation of a Ni-B alloy with a lower melting temperature [193]. It is reasonable to suppose that the observed incipient melting of Ti at ~1550 °C in the present study is caused by the solid state diffusion of boron from the TiB_2 substrate into the Ti sample and a composition shift in the near-substrate region from pure Ti to a Ti-B alloy.

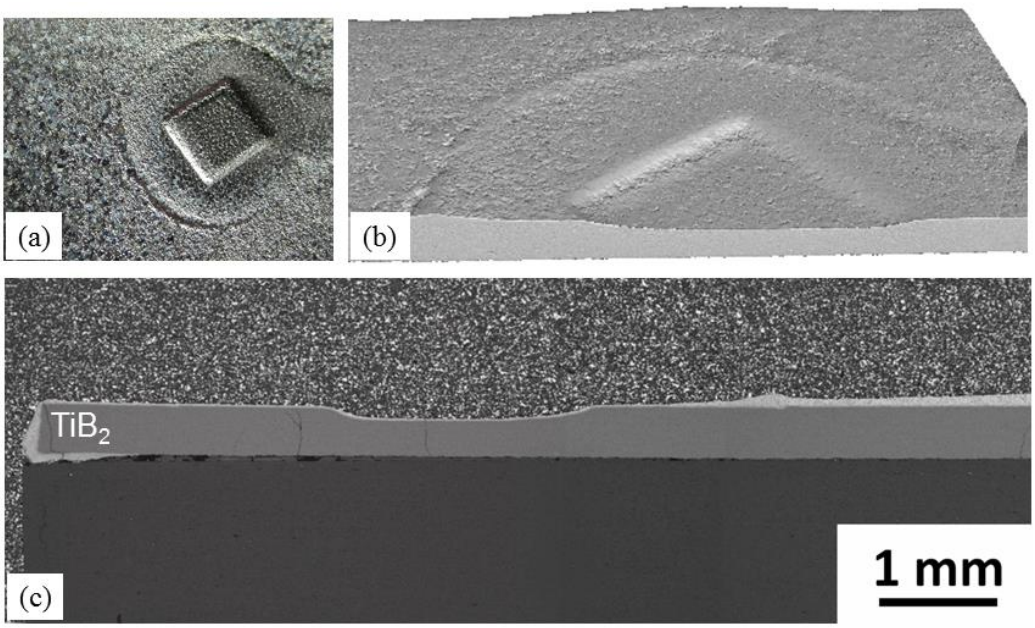

Fig. 5.3.1. Ti/TiB_2 couple after a high-temperature test carried out at 1550 °C: (a) top-view photograph, (b) three-dimensional X-ray computed tomography image, (c) SEM image taken from the cross-sectioned couple.

According to the thermodynamic calculations [85, 194, 195], the Ti-B eutectic contains around 7 at.% B and melts at about 1500 °C [195] – 1540 °C [85, 194]. In work [79], Ti has been suggested to be a major diffusing atom in a solid Ti/TiB_2 couple upon heating. However, other studies demonstrated that an interstitial diffusion mechanism of boron was dominant at the Ti/TiB interface [78, 196]. Also, we did not find any sign of Ti at the grain boundaries of TiB_2 near the Ti/TiB_2 interface. Instead, there was a lot of B (in the form of TiB) in the solidified drop.

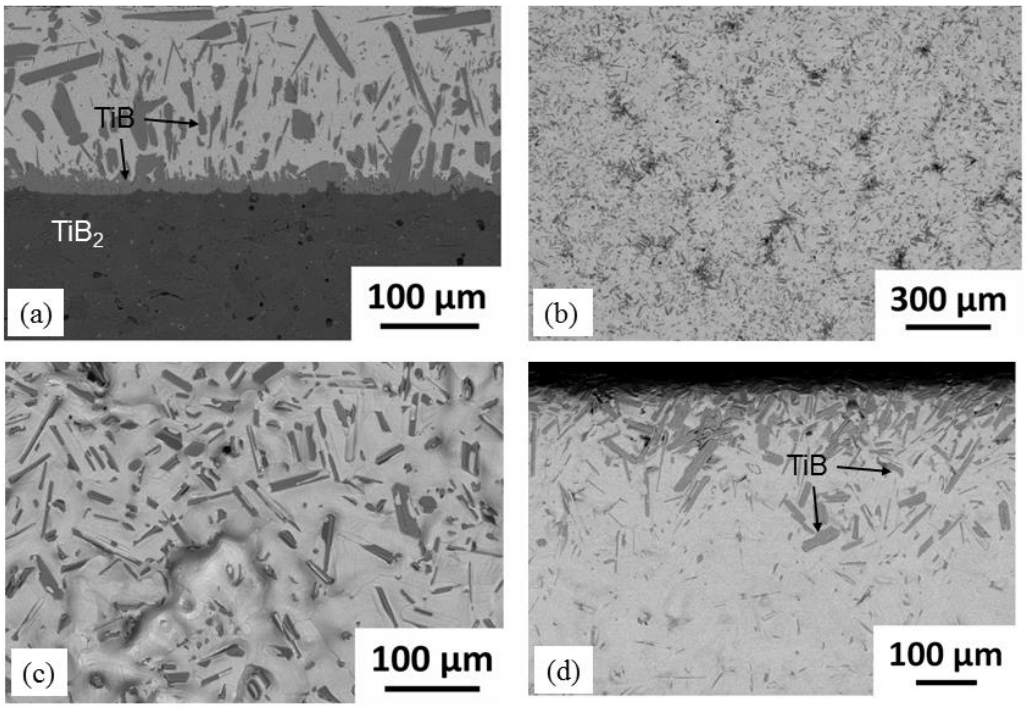

Fig. 5.3.2. SEM images taken from the cross section (a) and from the surface of solidified Ti/TiB_2 couple (b)-(d) after a high-temperature test carried out at 1550 °C: (b) in the middle of the Ti sample, (c) on the spread liquid, (d) at the periphery of the substrate. Light grey – Ti; *dark grey* – TiB.

A homogeneous TiB layer with a thickness of about 20 µm is formed overall at the interface, while TiB whiskers are observed in the Ti matrix as well as on the surface of the solidified sample (Fig. 5.3.2). X-ray diffraction analysis (Fig. 5.3.3a) also proves the presence of titanium monoboride in the Ti phase, whereas no peaks of TiB_2 are detected. In the crater, i.e. at the place of initial Ti sample, TiB needles are rather short (10–20 µm in length) and mainly colonize along the grain boundaries of TiB_2 ceramic (Fig. 5.3.2b). In the area covered by the liquid drop due to the liquid spreading, TiB whiskers with an average length of 80 µm and thickness of about 5 µm are homogeneously distributed in Ti matrix (Fig. 5.3.2c). Slightly shorter (~60 µm) and thicker (~7 µm) whiskers are collected at the periphery of the drop (Fig. 5.3.2d). Similar microstructure and morphology features of the TiB phases have been reported for Ti-TiB composites in works [16, 81, 196, 197]. The orthorhombic TiB phase exhibits a whisker morphology due to a preferential growth in [010] direction [77, 81]. Density functional

theory (DFT) calculations [78] showed that the interfacial energy of the (100) plane of TiB with α-Ti is about 3 times smaller as compared to the interfacial energy for the TiB (101)/α-Ti interface. This explains the experimentally observed longer (100) facet as compared the (101) and $(10\bar{1})$ facets.

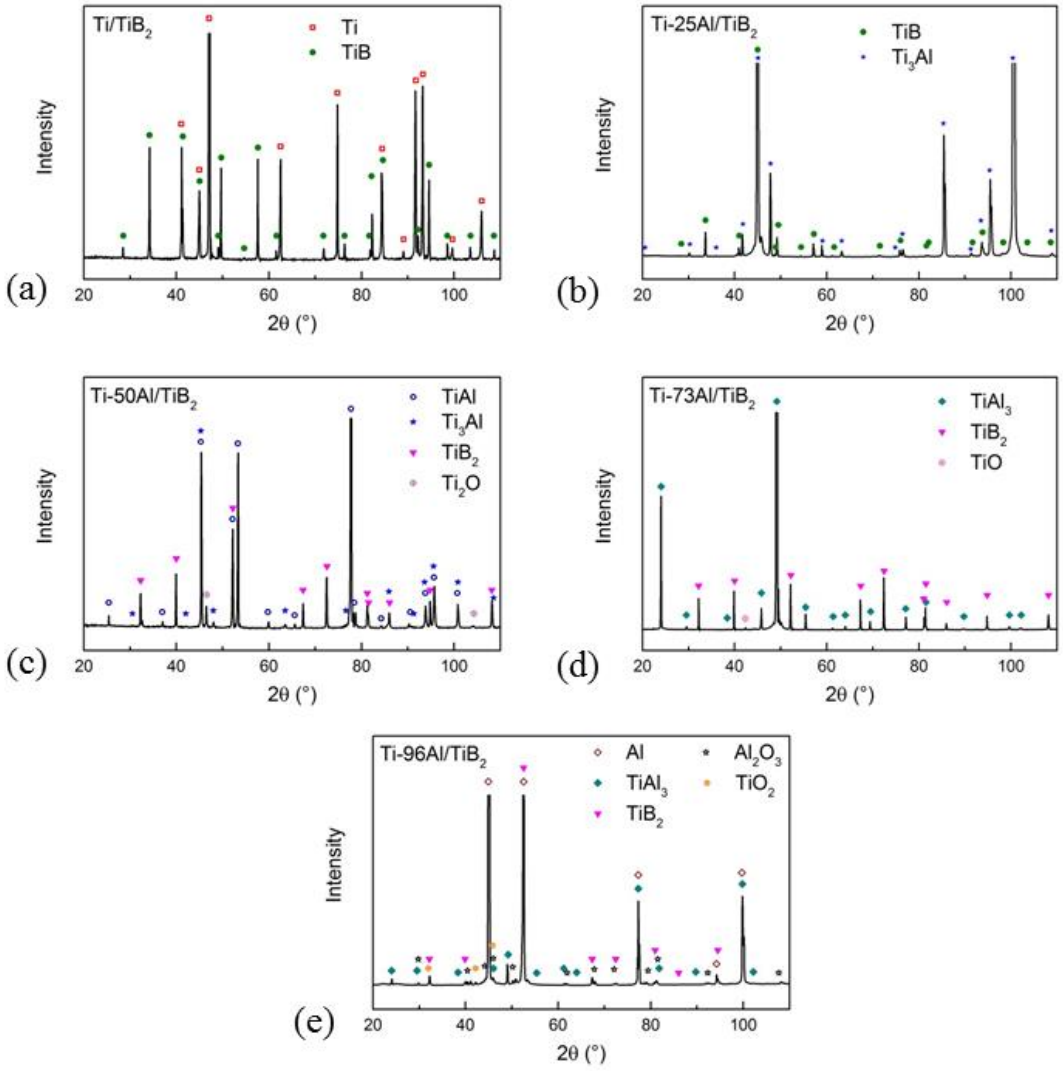

Fig. 5.3.3. XRD patterns measured from the drop surface of the Ti-Al/TiB_2 couples after the wetting tests: (a) pure Ti; (b) Ti-25Al ($Ti_{74.3}Al_{25.7}$); (c) Ti-50Al ($Ti_{49.3}Al_{50.7}$); (d) Ti-73Al ($Ti_{26.5}Al_{73.5}$); (e) Ti-96Al ($Ti_{3.5}Al_{96.5}$).

5.3.2 Ti-Al/TiB_2 system

Similar to pure titanium, the Ti-25Al, Ti-50Al, and Ti-73Al alloys also showed a very good wetting of TiB_2 ceramic just after melting, which has been observed at 1650 °C, 1470 °C and 1385 °C, respectively. These temperatures agree rather well with the reported thermodynamic data and the phase diagram for the Ti-Al system [147]. The somewhat lower melting temperatures measured in this study can be explained by diffusion of boron from the TiB_2 substrate similar to that just discussed in Ti/TiB_2 case as well as by the experimental uncertainty to some extent. The Ti-25Al and Ti-73Al melts completely wetted the substrates reaching a contact angle of 0°, while the Ti-50Al melt showed a final contact angle of about 20°. This is well seen on the SEM images taken from the cross-sectioned Ti-Al/TiB_2 couples in Fig. 5.3.4a, b.

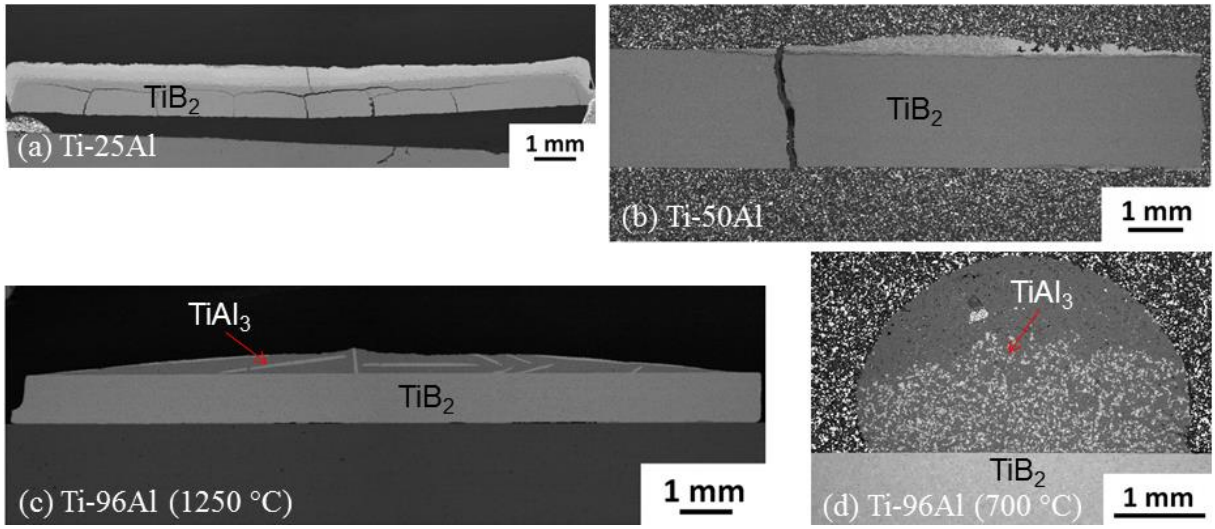

Fig. 5.3.4. SEM images taken from the cross-sectioned Ti-Al/TiB_2 couples after the high-temperature tests.

The Ti-96Al alloy melts over a wide temperature range between 666 °C and 1124 °C [147]. Its contact angle on a TiB_2 substrate continuously decreased from ~150° at 680 °C to ~55° at the liquidus temperature and further decreased to the value of ~13° upon heating to 1250 °C (Fig. 5.3.5). The non-wetting at low temperature can be attributed to the oxide layer present on the drop surface similar as it has been reported for liquid aluminum [52, 70, 129]. The cross-sections of the Ti-96Al/TiB_2 couples after heating to 1250 °C and 700 °C are presented in Fig. 5.3.4c, d, respectively. It has to be noted that the contact angle between Ti-96Al and TiB_2

ceramic is always somewhat larger than the contact angle for pure Al on TiB_2 measured recently by the same technique [129]. A similar behavior was also observed for the same liquid alloy on Al_2O_3 ceramic [50, 192]. The apparent worse wetting, compared to pure Al, is supposedly due to the semi-solid state of the Ti-96Al alloy between the solidus and the liquidus and the sedimentation of the $TiAl_3$ phase. The latter is well illustrated in Fig. 5.3.4d, where the sphere-like $TiAl_3$ particles, shaped by extrusion of the Ti-96Al alloy, keep their initial form after heating to 700 °C compared to the SEM image in Fig. 5.2.2d. On the other hand, SEM images taken from the cross-section of the Ti-96Al/TiB_2 couple after constant heating to 1250 °C reveal coarse $TiAl_3$ needles precipitated from the liquid.

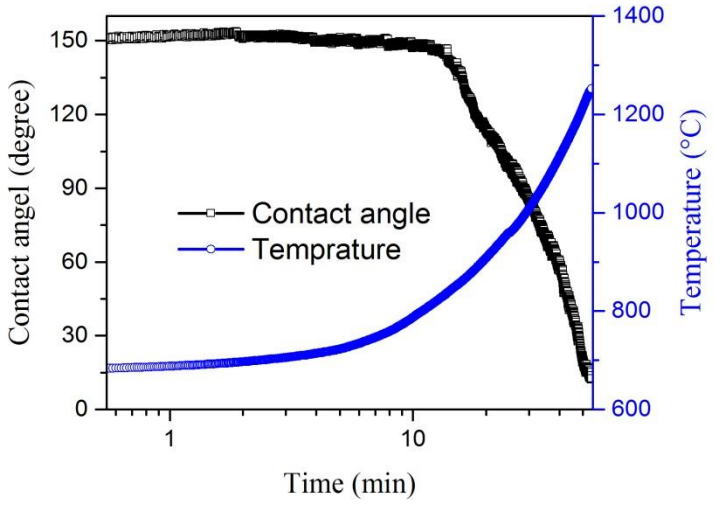

Fig. 5.3.5. Time dependence of the contact angle (*black rectangles*) and temperature (*blue circles*) for liquid Ti-96Al on TiB_2 ceramic by constant heating to 1250 °C.

Similar to the Ti/TiB_2 case, TiB is found at the Ti-25Al/TiB_2 interface as well as in the Ti_3Al matrix after the sessile drop test at 1650 °C (Fig. 5.3.6a). The presence of the TiB phase is also verified by XRD analysis (Fig. 5.3.3b). In contrast to the Ti/TiB_2 interface, the TiB phase does not form a single layer in the Ti-25Al/TiB_2 couple; it is rather a stack of densely packed whiskers extending up to about 200 μm in the vertical direction (Fig. 5.3.6a). Another remarkable feature of the Ti-25Al/TiB_2 interface is the penetration of the Ti-Al liquid along the grain boundaries in the TiB_2 ceramic and detachment of the grains. At first glance, this effect can be explained by a higher experimental temperature in the test with the Ti-25Al alloy (1650 °C vs

1550 °C for Ti/TiB_2). However, as the penetration depth increases with increasing Al concentration, the role of Al in grain boundary penetration seems to be more important than the temperature. This is well seen from the SEM images taken from the cross-sections of the Ti-50Al/TiB_2 (experimental temperature: 1470 °C) and Ti-73Al/TiB_2 (experimental temperature: 1385 °C) in Fig. 5.3.6b, c, respectively.

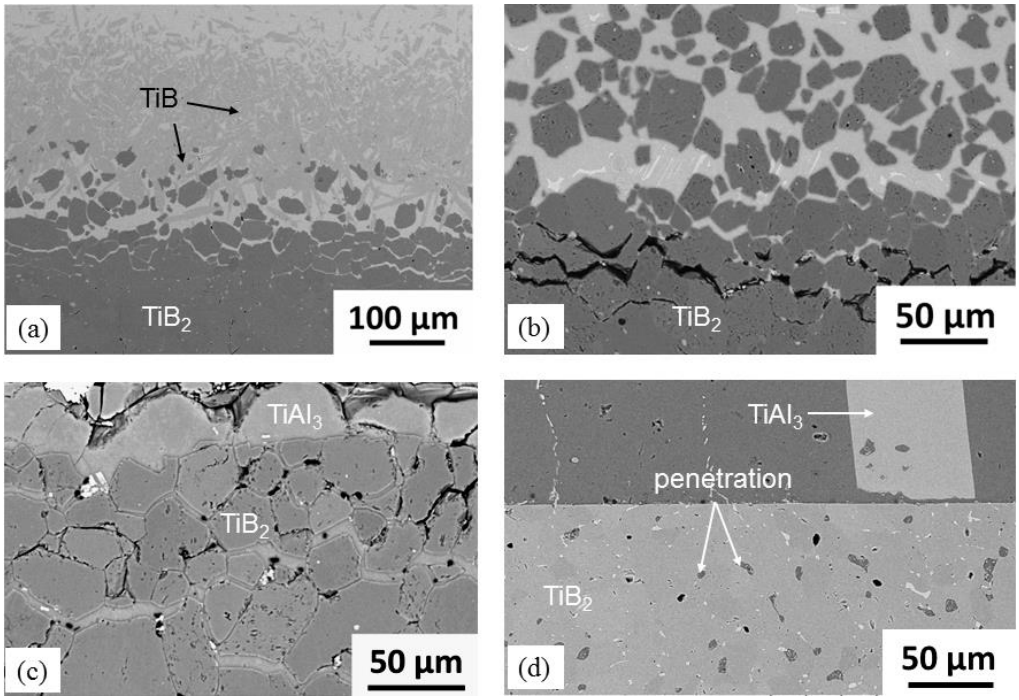

Fig. 5.3.6. SEM images taken from the interfacial area of the cross-sectioned Ti-Al/TiB_2 couples: (a) Ti-25Al alloy (1650 °C, 5 min): *dark grey* – TiB_2, *grey* – TiB, *light grey* – Ti-Al matrix; (b) Ti-50Al (1470 °C, 5 min): *dark grey* – TiB_2, *light grey* – Ti-Al matrix; (c) Ti-73Al (1385 °C, 5 min) showing grain boundary penetration of Ti-Al in the TiB_2 substrate; (d) Ti-96Al (1250 °C) showing alloy filling the pores in the TiB_2 ceramic.

In the Ti-50Al/TiB_2 couple, the detachment of TiB_2 grains is so intensive that they are found not only close to the interface (Fig. 5.3.6b) but also on the top of the drop (Fig. 5.3.7a, b). It should be mentioned that the XRD pattern of the solidified Ti-50Al/TiB_2 couple (Fig. 5.3.3c) does not identify any reaction product except oxides. In the Ti-73Al/TiB_2 couple, the grain boundary penetration depth reaches ~300 µm, although the sessile drop test was carried out at a much lower temperature compared to the previous Al/TiB_2 cases.

Similar to Ti-73Al and pure Al [129], the Ti-96Al melt does not dissolve TiB_2 ceramic. After heating the Ti-96Al/TiB_2 couple to 1250 °C the alloy/ceramic interface remains flat, as it can be seen from Fig. 5.3.4c. Moreover, liquid Ti-96Al does not really penetrate the grain boundaries but just fills the existing pores in the TiB_2 substrate.

For the Al-rich alloys Ti-73Al and Ti-96Al, $TiAl_3$ precipitates with a coarse needle-like structure are distributed in the Al matrix (Fig. 5.3.4c) as well as on the TiB_2 substrate (Fig. 5.3.7c, d). The XRD patterns taken from the surface of the solidified Ti-Al/TiB_2 couples after the sessile drop test do not reveal any reaction product. The reflections corresponding to the $TiAl_3$, TiB_2 and oxide phases are observed for the Ti-73Al/TiB_2 couple (Fig. 5.3.3d). The diffraction peaks measured from the Ti-96Al/TiB_2 couple can be assigned to the TiB_2, Al, $TiAl_3$ phases as well as TiO_2 and Al_2O_3 oxides (Fig. 5.3.3e).

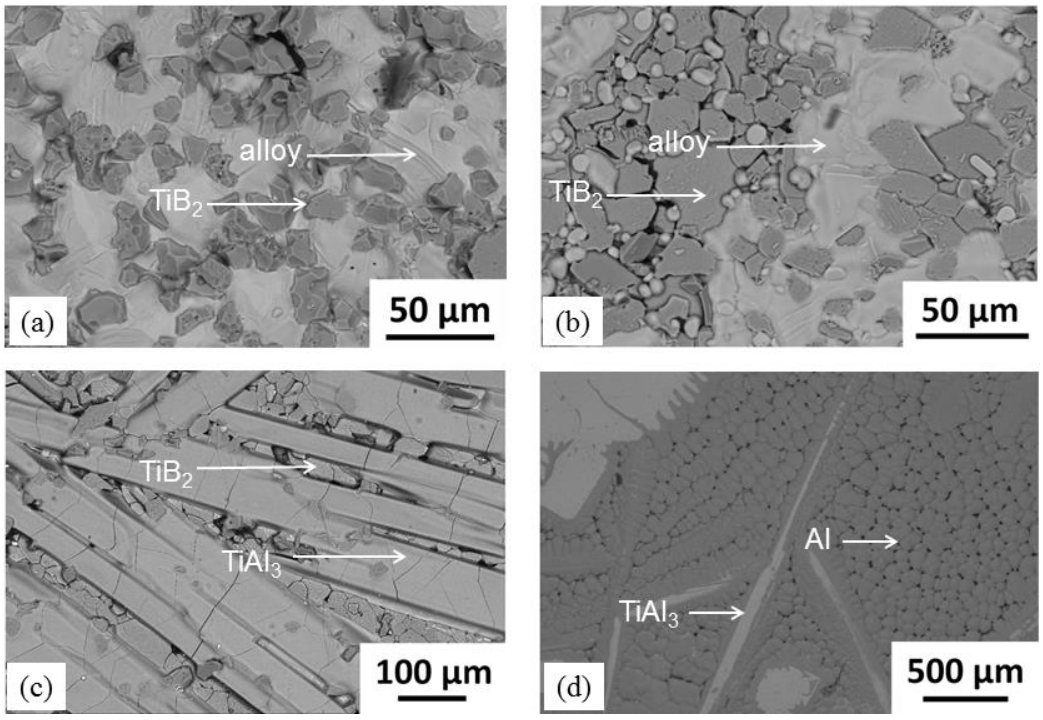

Fig. 5.3.7. SEM micrographs of the solidified Ti-Al/TiB_2 specimens (top-view) after the sessile-drop tests: (a) and (b) TiB_2 particles on the surface and at the outer edge of Ti-50Al drop (test temperature 1470 °C); (b) Ti-73Al, 1385 °C; (c) Ti-96Al, 1250 °C.

5.4 Thermomechanical compatibility of Ti-Al alloys and TiB_2

Along with the wetting and bonding behavior, the mechanical compatibility of dissimilar materials is also crucial for the fabrication of composite materials or joints. Due to the different mechanical and thermal properties of metallic alloys and ceramics, residual thermal stresses are generated at the metal/ceramic interfaces upon cooling from the processing temperatures [51, 198, 199]. Under assumption of fully elastic conditions, the residual thermal stress σ produced in a metal/ceramic joint can be estimated using the following equation [198]:

$$\sigma = \frac{E_{\mathrm{M}} \cdot E_{\mathrm{C}}}{E_{\mathrm{M}} + E_{\mathrm{C}}} \, \Delta\alpha \, \Delta T \quad , \tag{5.4.1}$$

where E_{M} and E_{C} are the Young's moduli of the metal and the ceramic, $\Delta\alpha = \alpha_{\mathrm{M}} - \alpha_{\mathrm{C}}$ is the difference of their thermal expansion coefficients and ΔT is the difference between the temperature at which the interface is free of stress and room temperature.

The coefficients of thermal expansion and the elastic moduli for the TiB_2 ceramic and the Ti-Al alloys (present work and literature data [88, 200-205]) are listed in Table 5.4.1. At room temperature, the CTE of pure Ti [200] ($8.6 \cdot 10^{-6}\,K^{-1}$) is about 28% larger than that for TiB_2 ($6.7 \cdot 10^{-6}\,K^{-1}$) [88]. It is slightly larger for the Ti-25Al alloy ($8.8 \cdot 10^{-6}\,K^{-1}$) and increases almost exponentially with further addition of Al (see Table 5.4.1). The Young's modulus shows a linear growth from 115 GPa for Ti [179] to 216 GPa for the $TiAl_3$ compound [202] and a linear decrease along with decreasing volume fraction of the $TiAl_3$ phase [203, 204] to 69 GPa for Al [205] (all values given at room temperature).

The third parameter determining the residual thermal stress is the temperature difference ΔT (Eq. 5.4.1). As a first approximation, it can be assumed that the interface is stress-free until the solidification is completed. The solidus temperatures for the equilibrium and non-equilibrium solidification of Ti-Al melts $T_{\mathrm{sol.eq.}}$ and $T_{\mathrm{sol.n\text{-}eq.}}$ calculated using the thermodynamic database given by Witusiewicz *et al.* [147] are listed in Table 5.4.1. Both $T_{\mathrm{sol.eq.}}$ and $T_{\mathrm{sol.n\text{-}eq.}}$ vary rather weakly (up to ~16%) between pure Ti and the $TiAl_3$ compound. However, there is an extremely large difference for the Ti-73Al alloy with $T_{\mathrm{sol.eq.}}$ =1395 °C and $T_{\mathrm{sol.n\text{-}eq.}}$ = 660 °C. The latter value is the same as the non-equilibrium solidification temperature for the Ti-96Al alloy.

The values of the residual thermal stress for the Ti-Al/TiB_2 couples estimated with Eq. 5.4.1 are presented in Table 5.4.1. The calculations are carried out using Young's moduli at room temperature while the thermal expansion coefficients are averaged at the given temperature

intervals (see Table 5.4.1). Both $\sigma_{eq.}$ and $\sigma_{n\text{-}eq.}$ increase virtually linearly from 288 MPa for the Ti/TiB_2 couple to about 830 MPa for the Ti-50Al/TiB_2 couple. However, σ can become either larger or smaller for the Ti-73Al/TiB_2 couple, depending on the solidification route ($\sigma_{eq.}$ of 1391 MPa vs. $\sigma_{n\text{-}eq.}$ of 658 MPa). The residual thermal stress is around 775 MPa for the Ti-96Al/TiB_2 couple.

Table 5.4.1. Mechanical and thermal characteristics of the Ti-Al alloys and TiB_2 ceramic.

Alloy	Solidification temperature		Coefficient of thermal expansion		Young's modulus	Residual thermal stress	
	$T_{sol.eq.}$ °C	$T_{sol.n\text{-}eq.}$ °C	Temperature range °C	α 10^{-6} K^{-1}	E GPa	$\sigma_{eq.}$ MPa	$\sigma_{n\text{-}eq.}$ MPa
TiB_2	–	–	20 – 1000	6.7 – 8.2 [88]	575 [88]	–	
Ti	1668	–	0 – 816	8.6 – 9.9 [200]	115 [179]	288	
Ti-25Al	1657	1636	50 – 800	8.8 – 14.1	147 [201] (for Ti_3Al)	776/766	
Ti-50Al	1461	1434	50 – 800	9.6 – 13.9	173 [201] (for TiAl)	835/820	
Ti-73Al	1395	660	50 – 800	12.0 – 15.6	216 [202] (for $TiAl_3$)	1391/658	
Ti-96Al	666	660	50 – 500	20.2 – 26.6	84 [203]	779/772	

α – coefficient of thermal expansion, E – Young's modulus at room temperature, $T_{sol.eq.}$ and $T_{sol.n\text{-}eq.}$ – equilibrium and non-equilibrium solidification temperature, respectively, $\sigma_{eq.}$ and $\sigma_{n\text{-}eq.}$ – estimated residual thermal stress at the Ti-Al/TiB_2 interface for the equilibrium and non-equilibrium solidification of the Ti-Al alloys, respectively.

In general, the SEM images taken from the cross-sections of the Ti-Al/TiB_2 couples after the high-temperature wetting tests (Figs. 5.3.1, 5.3.2, 5.3.4 and 5.3.6) confirm the above considerations. The number and the size of the cracks formed in the ceramic increase by alloying Ti with Al and decrease for the Al-rich alloys. However, it has to be noted that the metal/ceramic couples here are not suitable for a proper analysis of the residual thermal stress effects. Neither the quantity of the Ti-Al alloys nor the size of the substrates, particularly the thickness of TiB_2 plates, was prepared for such investigations. For example, in the Ti-50Al/TiB_2 couple, the

ceramic substrate remained macroscopically intact (Fig. 5.3.4b), although the estimated residual thermal stress is about 15% larger than that at the Ti-25Al/TiB_2 interface, which was severely damaged (Fig. 5.3.4a). (The breaking of the ceramic in the Ti-50Al/TiB_2 couple seen in Fig. 5.3.4b occurred during machining of the solidified couple). Hence, the apparent stability of the ceramic in the Ti-50Al/TiB_2 couple is likely due to its larger thickness. Similar stability of the ceramic in the Ti-73Al/TiB_2 couple can be explained by large TiB_2 volume compared to that of the Ti-Al alloy, unless it followed a non-equilibrium solidification path. The latter would result in a much smaller residual thermal stress upon cooling (Table 5.4.1).

5.5 Conclusions

1. Liquid Ti shows a complete wetting of the TiB_2 substrate at 1550 °C, i.e. at a temperature significantly lower than the melting point of pure Ti. This effect is related to the solid state diffusion of boron from the TiB_2 substrate into the Ti sample and a composition shift to a Ti-B alloy melting at a lower temperature. A homogeneous TiB layer with a thickness of about 20 μm is formed at the cross-sectioned Ti/TiB_2 couple.

2. Liquid $Ti_{74.3}Al_{25.7}$, $Ti_{49.3}Al_{50.7}$, $Ti_{26.5}Al_{73.5}$ and $Ti_{3.5}Al_{96.5}$ alloys wet very well the TiB_2 substrates just after incipient melting.

3. A layer of TiB whiskers with a thickness of about 200 μm is formed at the interface in the $Ti_{74.3}Al_{25.7}$/TiB_2 couple, whereas TiB_2 crystals are found inside as well as on the top of the $Ti_{49.3}Al_{50.7}$ drop.

4. No signs of TiB_2 dissolution or reaction with the TiB_2 substrates are found for the $Ti_{26.5}Al_{73.5}$/TiB_2 and $Ti_{3.5}Al_{96.5}$/TiB_2 couples. The liquid $Ti_{26.5}Al_{73.5}$ alloy penetrates along the TiB_2 grain boundaries, reaching a depth of about 300 μm, without detachment of TiB_2 grains from the substrate in the interfacial area. Liquid $Ti_{3.5}Al_{96.5}$ alloy just fills the inter-grain pores in the TiB_2 ceramic after constant heating to 1250 °C.

5. Micro- and macroscopic cracks are formed in Ti-Al/TiB_2 couples after the wettability tests due to a thermal expansion mismatch and high solidification temperatures of the Ti-Al alloys.

Chapter 6: Wettability and interfacial interactions of Ni-Al/TiB_2 and Ni-B/TiB_2 systems

This chapter at first presents a systematic study of the high-temperature wetting and interfacial interactions of liquid Ni-Al alloys with TiB_2. A gradual appearance of a sigmoidal profile was established to occur at the interface by increasing the Ni content in the Ni-Al alloys due to substrate dissolution in the melts. In this view, investigations of melting and wetting of Ni-B alloys on TiB_2 ceramic have been performed in order to understand the effects of boron in Ni-B alloys on the substrate dissolution and contribute to possible joining of TiB_2 ceramics. These results are presented in the second half of this chapter.

6.1 The Ni-Al/TiB_2 system

6.1.1 Introduction

Investigations of the Ni-Al/TiB_2 system are particularly interesting for the development of light-weight metal-matrix composites (MMC) as high-temperature structural materials [17, 62, 206-208]. Ni_3Al intermetallic is characterized by very good properties at elevated temperature, such as a tensile and compressive yield strength, fatigue and oxidation resistances, but it is brittle at room temperature [209]. NiAl compound melts at a high temperature and shows excellent oxidation properties, but it has a low yield strength at elevated temperature and is brittle at room temperature [206, 210]. It is reasonable to expect that the drawbacks of the Ni-Al alloys can be overcome and major advantages can be exploited by the development of Ni-Al/TiB_2 composites with appropriate ceramic particles and microstructures.

So far, numerous studies related to the synthesis of Ni-Al composites reinforced with TiB_2 phase have been carried out (see for example Refs. [17, 62, 206-208]). The composites were prepared by different techniques such as for example hot pressing [207, 208], casting [17] or laser melting [16, 22, 23]. If the investigations of the composition and microstructure of the as-prepared composites are rather straightforward with the help of diffraction and microscopy techniques, it is quite difficult or almost impossible to study the interfaces and phases formed

between the metallic matrix and the ceramic reinforcement in the composites due to a small particle size. Therefore, direct investigations of the interfacial phenomena are of high importance.

Interfacial interactions between liquid Al and TiB_2 ceramic have been studied in many laboratories. An overview of earlier works as well as the results of our study can be found in the chapters 1 and 4. There are several reports on the high-temperature wetting and reactivity in liquid Ni/TiB_2 system [72-76]. However, we are not aware about any study of liquid Ni-Al alloys with TiB_2 ceramic.

6.1.2 Materials

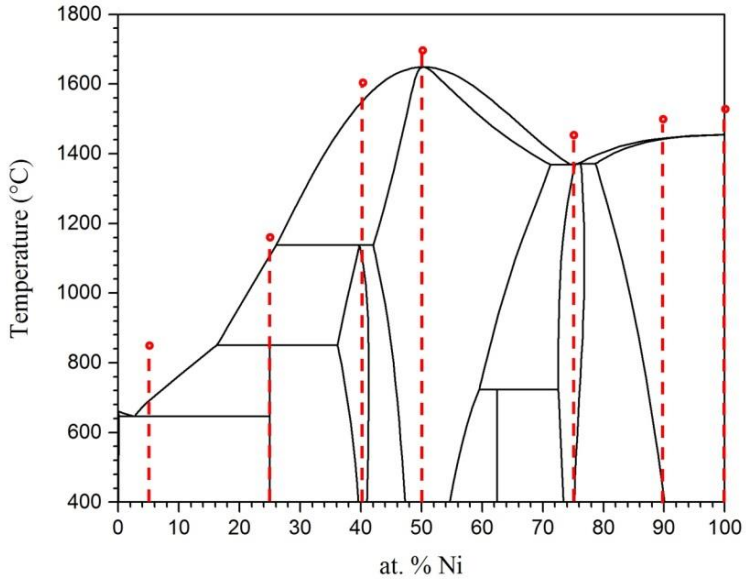

Fig. 6.1.1. Al-Ni binary phase diagram calculated with Pandat software using thermodynamic data from Ref. [149]. The vertical *dashed lines* indicate the composition of the alloys studied in this work, whereas *open circles* denote the experimental temperatures.

The compositions of Ni-Al alloys studied in the sessile drop experiments are marked on the calculated phase diagram in Fig. 6.1.1. The density of the alloys in the solid state (room temperature) and in the liquid state (temperature of the isothermal wetting tests) is given in Table 6.1.1. The room temperature density was calculated using the Archimedes method by weighting the samples in air and in dodecane. The liquid state density was calculated under assumption of ideal solution using densities of pure Al and Ni from Ref. [211].

Table 6.1.1. Properties of pure Al and Ni, and Ni-Al alloys.

Composition (at.%)	Density at r.t. (experimental) (g/cm^3)	Density at $T_{wetting}$ (calculated) (g/cm^3)	$T_{wetting}$ (°C)
Al	2.7	2.36	710*
Ni_5Al_{95}	2.96	2.50	857
$Ni_{25}Al_{75}$	3.77	3.19	1147
$Ni_{40}Al_{60}$	4.58	3.63	1606
$Ni_{50}Al_{50}$	5.76	4.07	1688
$Ni_{75}Al_{25}$	6.90	5.79	1450
$Ni_{90}Al_{10}$	7.58	6.96	1488
Ni	8.74	7.85	1500

*studied in Ref. [129].

6.1.3 Results and discussion

Pure metals on TiB_2

The wetting behavior and interfacial interactions between liquid Al and TiB_2 ceramic at the temperature between 700 °C and 1400 °C [129] are described in Chapter 4.

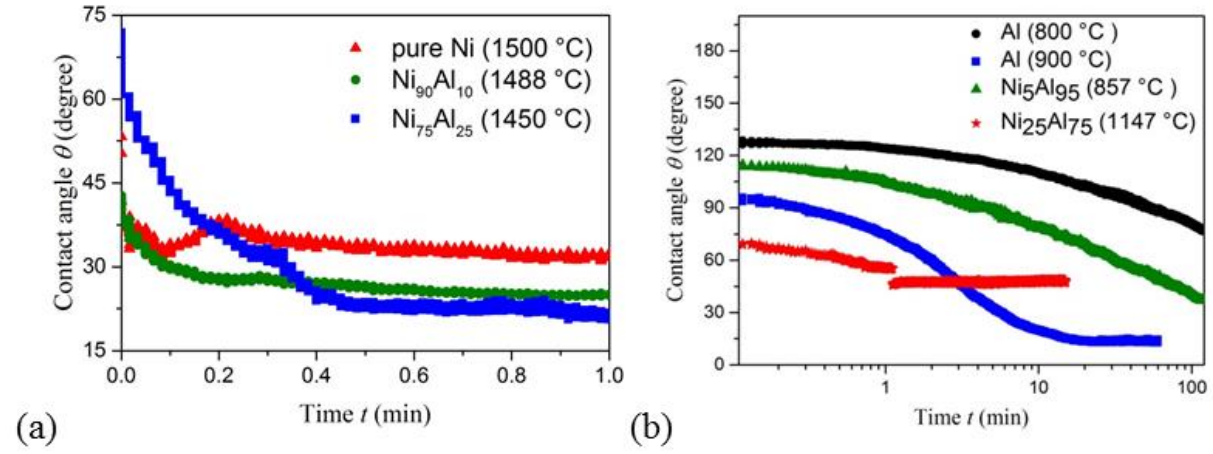

Fig. 6.1.2. Isothermal wetting kinetics for liquid on TiB_2 ceramic at different temperatures: (a) molten Ni and Ni-rich alloys; (b) molten Al [129] and Al-rich alloys.

In the present study, the wetting behavior of molten Ni on TiB_2 ceramic has been studied at a constant temperature of 1500 °C. Nickel melt wetted the TiB_2 substrate immediately after coming into a contact with it. The contact angle of about 50° formed during the first second can be considered as a true contact angle for liquid Ni on TiB_2 ceramic. Within the next 15 min, the contact angle decreased to an equilibrium value of 30.5° and then remained virtually unchanged (Fig. 6.1.2a). Principally the same behavior of the contact angle was reported for Ni/TiB_2 at 1450 by Samsonov *et al.* [73].

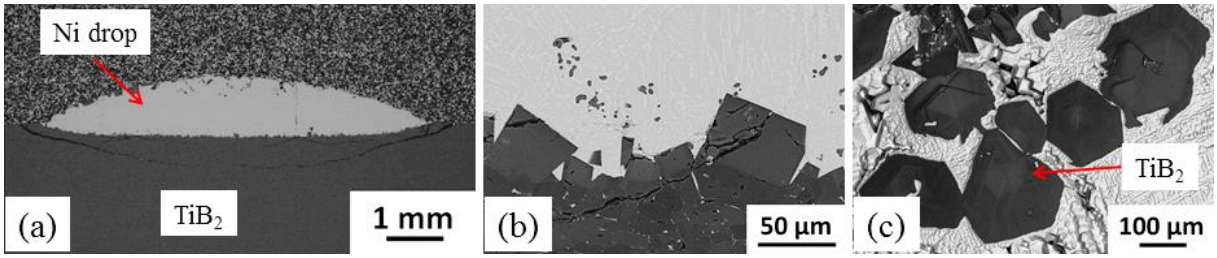

Fig. 6.1.3. Ni/TiB_2 couple after the sessile drop test carried out at 1500 °C for 15 min: (a) sigmoid interface profile; (b) magnified SEM image taken at the interface, showing a eutectic structure and penetration of Ni along TiB_2 grain boundaries; (c) TiB_2 precipitates observed on the surface of the drop.

The Ni/TiB_2 interface in a solidified sample is characterized by a sigmoidal profile (Fig. 6.1.3a), similar to that in the case of Ni/HfB_2 interaction [139]. This kind of interface profile is due to a more intensive dissolution of the central part of the substrate in an alloy drop compared to its periphery [212]. As determined by SEM/EDX and XRD analysis, $Ti_2Ni_{21}B_6$ ternary compound is a main phase of the solidified drop along with a minor α-Ni(Ti) solid solution (Fig. 6.1.3b)

A SEM image taken at the Ni/TiB_2 interface (Fig. 6.1.3b) shows that the liquid phase penetrated and spread along the grain boundaries in the ceramic. As reported by Passerone *et al.* [139], liquid Ni similarly penetrated a polycrystalline HfB_2 ceramic via grain boundaries. A continuous layer of newly grown TiB_2 crystals is observed at the Ni/TiB_2 interface (Fig. 6.1.3b). These crystals, several times larger than the grains of the original TiB_2 ceramic, nucleated and grew along the solid-liquid interface during Ni/TiB_2 interaction by a dissolution-precipitation mechanism. Also, rather large TiB_2 crystals with a typical hexagonal plate-like morphology [213,

214] are found on the surface of the drop (Fig. 6.1.3c). There are a small number of small TiC_x particles inside the drop close to the interface (Fig. 6.1.3b). It is reasonable to suppose that they are also formed by the dissolution-precipitation mechanism and originate from the TiC_x particles found in the sintered TiB_2 ceramic, as reported earlier [129].

A quite large wetting crater of the depth up to about 230 μm has developed under the Ni drop. The wetting crater formed after the fast spreading of the Ni melts would pin the advancing of the triple line. Therefore, the apparent contact angle (i.e. the angle between the liquid surface and the substrate's surface plane) remained then unchanged till the end of the high temperature test.

Al-rich alloys

The variation of the contact angle θ with time t for the Al-rich alloys on the TiB_2 substrates is show in Fig. 6.1.2b. At 857 °C, liquid Ni_5Al_{95} exhibits a continuous decrease of the contact angle from an initial value of about 114° to 36° after 2-hour isothermal heating. The shape of the $\theta(t)$ curve is quite similar to that for liquid Al at 800 °C [129], suggesting that the addition of 5 at.% Ni to Al does not essentially influence the wetting behaviour. The situation is different in the case of the $Ni_{25}Al_{75}$ melt. At 1147 °C, the wetting angle decreases from 70° to 55° within the first minute of the contact, and then suddenly drops to 48°, remaining constant until the end of the sessile drop experiment. The discontinuous decrease of the contact angle and increase of the drop base diameter (not shown) after 1 min contact with the TiB_2 substrate is obviously resulting from de-pinning of the triple line.

The top-view photos of the solidified samples are shown in Fig. 6.1.4a-b. Compared to the Ni_5Al_{95} composition, the solidified $Ni_{25}Al_{75}$ drop is rather asymmetrical, indicating an asynchronous advancing of the triple line on the substrate surface. Due to the intensive grain boundary diffusion (spreading of liquid alloy through the open microgrooves [215]), the area adjacent to the triple line in $Ni_{25}Al_{75}/TiB_2$ couple is covered by a spreading halo (Fig. 6.1.4c-e), which is also asymmetrical. Probably this is explained by the orientation anisotropy of TiB_2 grains, some of which are slightly elongated. However this issue has not been studied in details. The region I of the spreading halo contains a large amount of coarse dendrites, while remarkably less, separated dendrites are observed in the region II. Most probably, the coarse dendrites pin

the drop spreading, and this explains the wetting behaviour of liquid $Ni_{25}Al_{75}$ on the TiB_2 substrate during the first minute.

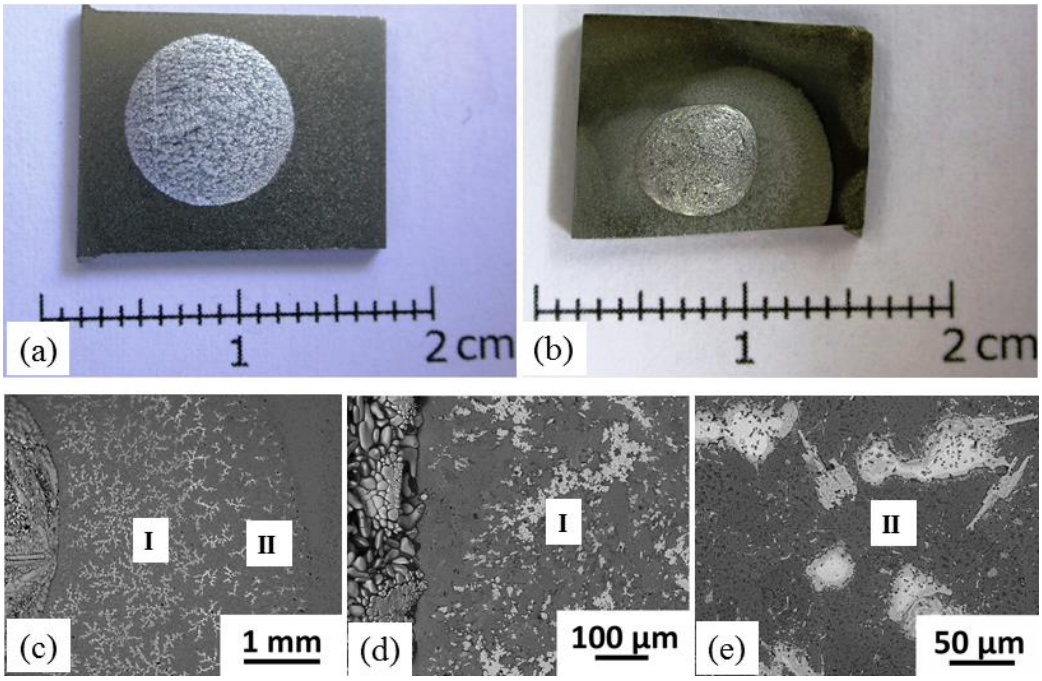

Fig. 6.1.4. Al-rich alloys on the TiB_2 substrates after the sessile drop tests: (a) and (b) digital photographs of Ni_5Al_{95}/TiB_2 couple (857 °C, 2 h) and $Ni_{25}Al_{75}/TiB_2$ couple (1147 °C, 15 min), respectively; (c)-(e) SEM images showing the drop front in the $Ni_{25}Al_{75}/TiB_2$ couple.

The SEM/EDX and XRD analysis of the Ni_5Al_{95}/TiB_2 and $Ni_{25}Al_{75}/TiB_2$ interfaces did not reveal any reaction product or substrate dissolution (Figs. 6.1.5 and 6.1.6). The interfaces remained macroscopically smooth and planar in both samples. Compared with the previous study of Al/TiB_2 [129], there is no clear evidence for formation of new reaction products (e.g. titanium aluminide, aluminium carbide) and substrate penetration along the grain boundaries in the Al-rich Ni-Al/TiB_2 couples, except for minor Al_2O_3 particles at the interface. Probably, the experimental temperatures were not suitable for the reaction and penetration to occur in these couples, in contrast to the Al/TiB_2 system.

In agreement with the Ni-Al phase diagram (Fig. 6.1.1), the solidified Ni_5Al_{95} drop is constituted by oval-shaped $NiAl_3$ intermetallic phase homogeneously dispersed in the (Al+$NiAl_3$) eutectic (Fig. 6.1.5a). The $Ni_{25}Al_{75}$ alloy exhibits a cored multi-phase microstructure (Fig.

6.1.5b). The main phase is $NiAl_3$, formed by peritectic reaction L + Ni_2Al_3 → $NiAl_3$. These reactions are rather slow as the product phase will form at the boundary between the two reacting phases thus separating them, and slowing down any further reaction. However, as the peritectic reaction was not completed upon non-equilibrium cooling, Ni_2Al_3 particles are observed in the centre of the $NiAl_3$ grains, while remaining Al phase, containing less than 1 at.% dissolved Ni (measured by EDX), fills the $NiAl_3$ inter-grain space.

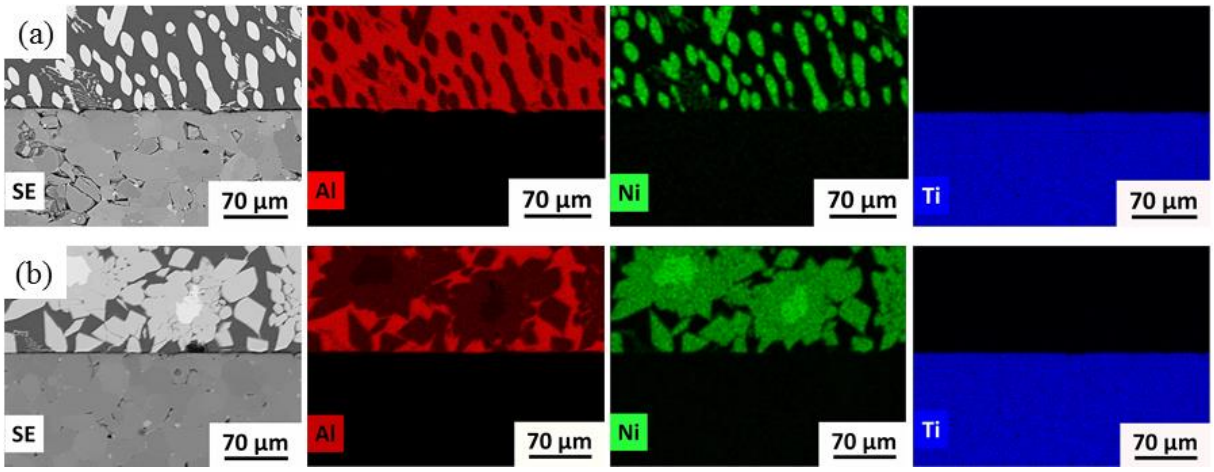

Fig. 6.1.5. SEM/EDX images of the cross-sectioned couples after isothermal sessile drop tests: (a) Ni_5Al_{95}/TiB_2 (857 °C, 2 h): *white* –$NiAl_3$, *dark grey* – Al matrix; (b) $Ni_{25}Al_{75}/TiB_2$ (1147 °C, 15 min): *white* –Ni_2Al_3, *light grey* –$NiAl_3$, *dark grey* – Al matrix.

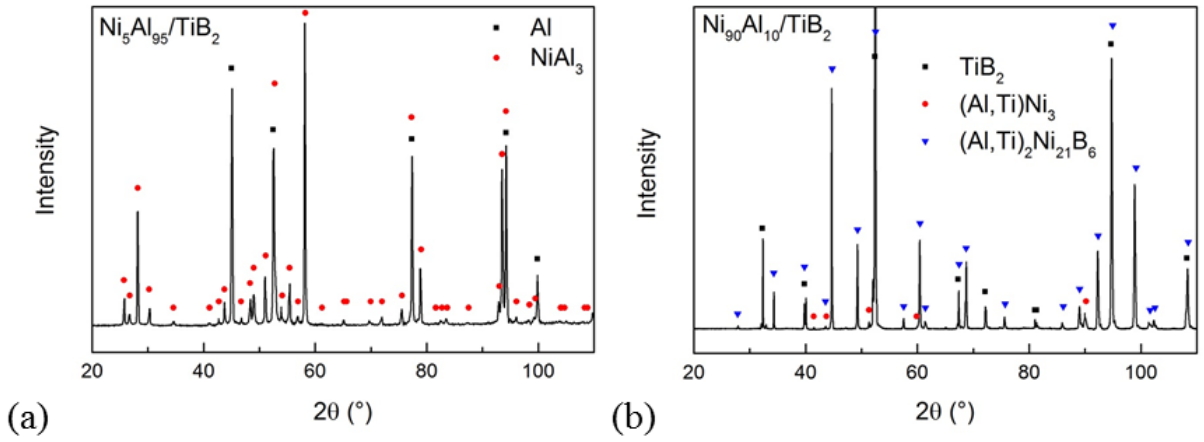

Fig. 6.1.6. XRD patterns taken from the surface of solidified drops after the interaction with TiB_2 substrates: (a) Ni_5Al_{95}; (b) $Ni_{90}Al_{10}$.

$Ni_{40}Al_{60}$ and $Ni_{50}Al_{50}$

Drops of liquid $Ni_{40}Al_{60}$ and $Ni_{50}Al_{50}$ alloys were dispensed at the temperature of 1606 °C and 1688 °C, respectively, and instantaneously spread over the TiB_2 substrates. Furthermore, the spreading melts streamed down along the substrates walls and filled the gaps between the TiB_2 substrates and Al_2O_3 support. An example for $Ni_{50}Al_{50}/TiB_2$ alloy is shown in Fig. 6.1.7a. This indicates that both ceramics are completely wetted under conditions of this study. Moreover, both liquid $Ni_{40}Al_{60}$ and $Ni_{50}Al_{50}$ were found in the ceramic, either filled pores at the triple junctions or penetrated along the grain boundaries (Fig. 6.1.7). The precipitates of TiB_2 phase (composition was determined by EDX analysis) were found to form inside the $Ni_{50}Al_{50}$ alloy (Fig. 6.1.7a) by a dissolution- precipitation mechanism, as seen in the $Ni_{50}Al_{50}$ alloy layer between TiB_2 and Al_2O_3 ceramics. This is in line with the crystallization and growth of TiB_2 in the NiAl liquid matrix by combustion synthesis reported by Lau *et al.* [216]. It is interesting that TiB_2 precipitation did not really happen in the case of $Ni_{40}Al_{60}$ drop. This can be explained by a decreasing dissolution of TiB_2 with decreasing Ni content in the Ni-Al melt and high solubility limit of Ti in liquid Al.

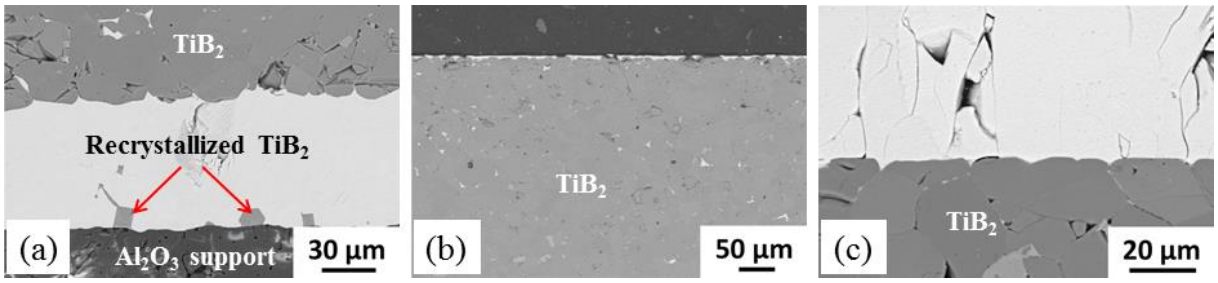

Fig. 6.1.7. SEM Images of the $Ni_{40}Al_{60}/TiB_2$ and $Ni_{50}Al_{50}/TiB_2$ couples after the sessile drop tests performed for 15 min at 1688 °C and 1606 °C respectively: (a) $Ni_{50}Al_{50}$ alloy layer between TiB_2 plate and Al_2O_3 support of cross-sectioned $Ni_{50}Al_{50}/TiB_2/Al_2O_3$ assembly; (b) close to interface showing alloy penetration in the ceramic; (c) grain boundary grooves at the interface.

During the high-temperature melt-substrate interaction, the grain boundary grooves with a depth up to about 5 μm were formed due to a minor TiB_2 dissolution, as it can be seen from a SEM image taken at the cross section of the solidified couples (Fig. 6.1.7c). Supposedly, the liquid metal tended to penetrate along the grain boundaries into the ceramic, and either dissolved

the weaker bonded 'remainders' of the grains, which may appear due to the cutting of the substrate, or released and moved them into the droplet for the further dissolution. The grain boundary grooves essentially roughen the substrate surface, which in general may reduce the drop spreading rate [130]. However, this seems to produce little effect in the present cases.

Ni-rich alloys

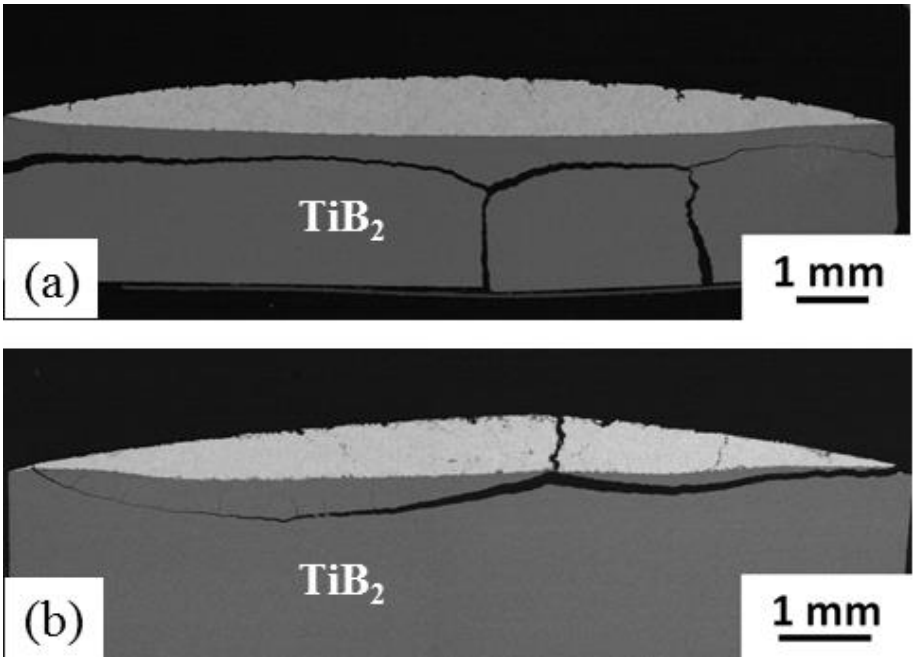

Fig. 6.1.8. Cross-sectioned samples after the sessile drop tests: (a) $Ni_{75}Al_{25}/TiB_2$ (1450 °C, 15 min); (b) $Ni_{90}Al_{10}/TiB_2$ (1488 °C, 15 min).

For $Ni_{75}Al_{25}$ and $Ni_{90}Al_{10}$ alloys, the apparent contact angle decreased from the initial value of about 72° and 41° measured immediately after the drop dispensing at 1450 °C and 1488 °C (Fig. 6.1.2a) to an equilibrium angle of about 18° and 17° with 15-min isothermal heating, respectively. Similar to Ni/TiB_2, sigmoidal interface profiles are developed at the $Ni_{75}Al_{25}/TiB_2$ and $Ni_{90}Al_{10}/TiB_2$ interfaces (Fig. 6.1.8). However, the interfaces in these two systems are less curved than that of Ni/TiB_2. This suggests that the dissolution rate is essentially reduced upon addition of Al, whereas the spreading remains comparable to that for pure Ni. Since the experimental temperature has been decreased by just 50 K and 12 K for the alloys with

25 at.% and 10 at.% Al, compared to the test with pure Ni, it is reasonable to suppose that the change of composition plays more important role than the temperature (Fig. 6.1.2a).

The Ni-rich Ni-Al melts are found to spread along the grain boundaries on the ceramic surface leaving a spreading halo around the solidified drops. A closer examination of the spreading halo shows the surface steps on the TiB_2 grains due to dissolution (not shown). It has to be mentioned that dissolution steps on the overflowed TiB_2 grains are also observed in the $Ni_{40}Al_{60}/TiB_2$ and $Ni_{50}Al_{50}/TiB_2$ systems although the cross-sectioned interfaces are not curved.

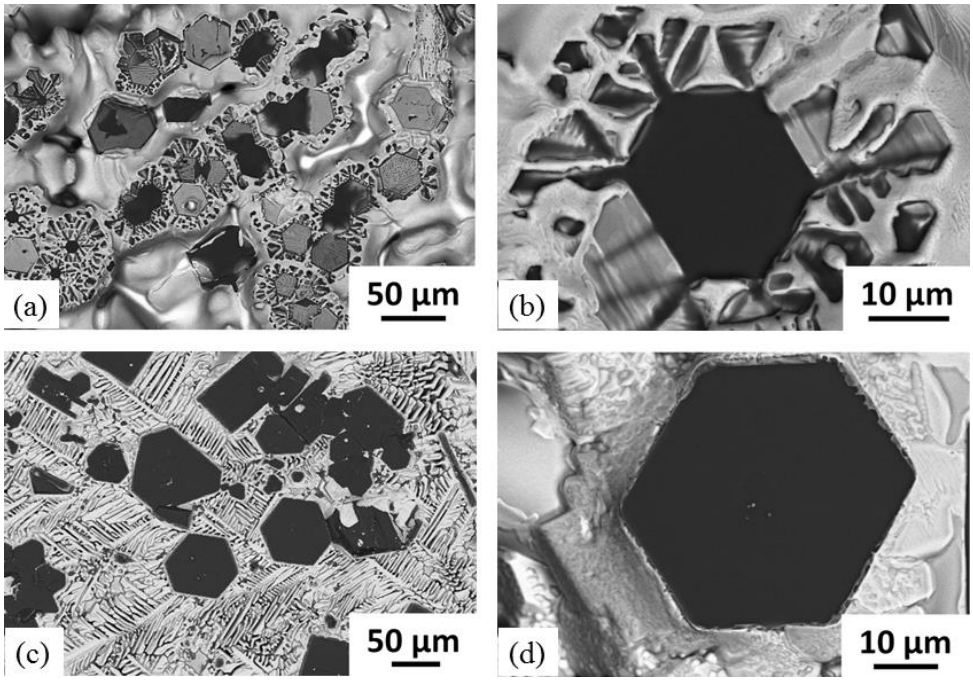

Fig. 6.1.9. Surface morphology of solidified drops after the sessile drop tests: (a)-(b) $Ni_{75}Al_{25}$ (1450 °C, 15 min); (c)-(d) $Ni_{90}Al_{10}$ (1488 °C, 15min). (b) and (d) showing the hexagonal TiB_2 crystals (black phase).

Similar to the observation in the Ni/TiB_2 couple, TiB_2 particles precipitated either on the surface (Figs. 6.1.9) or inside the Ni-Al drop (Fig. 6.1.10). It is worth noting that TiB_2 particles settle down and agglomerate on the surface of the $Ni_{75}Al_{25}$ drop as shown in Figs. 6.1.9a-b). The observed morphology of TiB_2 precipitates is characteristic for the particles distributed overall in the $Ni_{75}Al_{25}$ drop (Fig. 6.1.10a). Several TiB_2 contain core crystals whose chemical composition corresponds to TiC_x by EDX analysis, suggesting that these particles play a role of

heterogeneous nucleation seeds for TiB_2. The dissolution-precipitation mechanism for the TiB_2 and TiC_x phases can be summarized as following: Ni-rich melts exhibit a good capability of dissolving TiB_2 and TiC_x from the substrate during the wetting test. The formation of TiC_x is prior to the formation of TiB_2 due to kinetic factors, as reported in the studies on fabrication of TiC-TiB_2 composites [217-219]. TiC has a large number of facets to act as nucleating sites owing to its fcc structure unlike TiB_2, which nucleates only at the basal planes [220-221]. Upon cooling, small amounts of TiC_x precipitate firstly in the liquid solution and act as the nucleation sites for the TiB_2 particles and even modify the faceted TiB_2 grain shape. Our observations are quite consistent with the result of the dissolution-precipitation of HfB_2 grains in the liquid Ni [139], in which HfC particles acted as nucleation seeds for HfB_2.

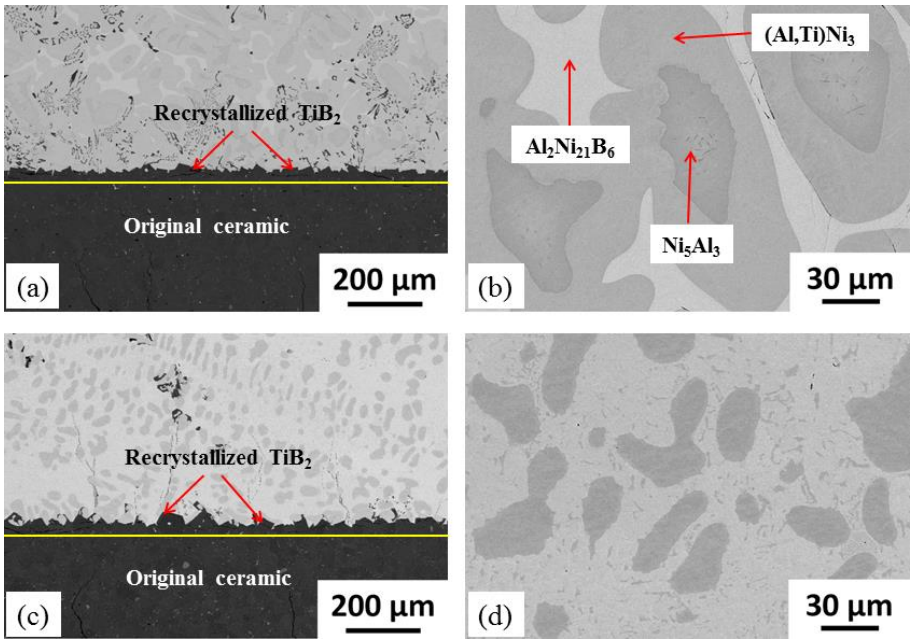

Fig. 6.1.10. Interfacial microstructure of the sessile drop samples with Ni-rich alloys: (a)-(b) $Ni_{75}Al_{25}/TiB_2$: *grey* – $(Al,Ti)Ni_3$, *dark* – Ni_5Al_3, *white* – $Al_2Ni_{21}B_6$; (c)-(d) $Ni_{90}Al_{10}/TiB_2$: *dark-grey* – $(Al,Ti)Ni_3$, *light-grey* – $(Al,Ti)_2Ni_{21}B_6$

The precipitation of ceramic particles on the drop top seems to depend mainly on the ratio of the densities of the ceramic and the melts. Taking account the difference in density (4.46 g/cm^3 for TiB_2, 4.93 g/cm^3 for TiC [222], 6.96 g/cm^3 for $Ni_{90}Al_{10}$ at 1488 °C, and 5.79 g/cm^3 for $Ni_{75}Al_{25}$ at 1450 °C), the density of heavy melts exceeds that of the ceramic particles and TiB_2

and/or TiC_x formed migrate to the upper part of the drops, causing intensive floatation as well as their collection on the top of the drop. This is in fairly good accordance with the observation on the surface of the drop (Fig. 6.1.9).

In comparison with the ceramic phases in the couples of pure Ni and Ni-rich alloys, an increase in Al content in Ni-Al alloys notably influences the precipitation of TiC_x and TiB_2 phases. With increasing Al addition in Ni, the precipitation of TiC_x particles will be supposedly suppressed either inside the drop or on their surface. This is well seen from the SEM images taken from the cross-sectioned couples (Figs. 6.1.3 and 6.1.10). In view of the morphology and distribution of TiB_2 precipitates, they are mainly formed during cooling-down while for pure Ni and $Ni_{90}Al_{10}$, there exists a more tendency of TiB_2 crystallizing and growing due to large dissolution.

$Ni_{90}Al_{10}$ drop shows a two-phase structure after the solidification, as seen in Fig. 6.1.10c-d. It is constituted of a dark-grey phase (Al,Ti)Ni_3 (Ni_3Al dissolves up to 15 at.% Ti [223] and Ti substitutes for Al) and a light-grey ternary phase with composition of $(Al,Ti)_2Ni_{21}B_6$. The XRD analysis has confirmed the presence of the $(Al,Ti)_2Ni_{21}B_6$, (Al,Ti)Ni_3 and TiB_2 phases in the solidified drop, as shown in Fig. 6.1.6. The cross-section of $Ni_{75}Al_{25}$ drop (Fig. 6.1.10a-b) exhibits a heterophase structure consisting of (Al,Ti)Ni_3 phase (grey), intermetallic phase Ni_5Al_3 (dark; composition determined by the EDX analysis) and ternary intermetallic $Al_2Ni_{21}B_6$ (white).

6.1.4 Conclusions

Liquid Ni-Al alloys are found to show different wetting behavior on the TiB_2 substrates, depending on both the alloy composition and processing conditions. The main findings of this study are as follows:

1. In the case of pure Ni and Ni-rich melts, TiB_2 and TiC_x are dissolved and precipitate inside the drops as well as on their surface upon cooling-down. An increase in Ni content in the Ni-Al alloys causes a noticeable dissolution of the substrate in the melt and the appearance of a sigmoidal interface profile.

2. Instantaneous spreading takes place when the drops of $Al_{50}Ni_{50}$ and $Al_{60}Ni_{40}$ alloys are dispensed onto the TiB_2 substrates at a temperature above 1600 °C. Minor recrystallized TiB_2 crystals in form of hexagonal and facet ones, precipitate in the $Al_{50}Ni_{50}/TiB_2$ couple.

3. Liquid Al-rich alloys wet well TiB_2 substrates and the interfaces remained macroscopically smooth and planar, providing evidence for the absence of any chemical reaction between the melt and the ceramic.

4. The wetting behavior of liquid Ni-Al alloys on TiB_2 ceramic changes from a non-reactive wetting on the Al-rich side to a dissolutive, reactive wetting on the Ni-rich side.

6.2 The Ni-B/TiB_2 system

6.2.1 Introduction

Ni-based alloy with addition of B are attractive for high-temperature applications. Wettability and interfacial interactions have been extensively studied for Ni-B alloys and ZrB_2 and HfB_2 ceramics [139, 224-226]. Those results showed that dissolution of these ceramic can be controlled by adjusting composition of Ni-B alloys. Also thermodynamic calculations for the Ni-B-X (X = Ti, Zr, Hf) ternary systems [195] demonstrated that alloying of Ni with B is very effective in reducing and even suppressing the dissolution of transition-metal diborides [227, 228]. To our knowledge, the wetting behavior and interfacial interactions between liquid Ni-B alloys and TiB_2 ceramic were not studied. We have therefore focus on this problem. A part of the results presented below has already been published in Journal of Materials Engineering and Performance [229].

6.2.2 Results and discussion

Wetting behavior

In the sessile drop tests, Ni-B samples with a weight of 200 - 300 mg were placed on the TiB_2 substrates from the beginning of the experiments. Due to a special shape of the solid alloys, both melting of Ni-B and wetting of TiB_2 ceramic were well observed as it is demonstrated by a series of digital images in Figs. 6.2.1 and 6.2.2. According to the Ni-B phase diagram [195], $Ni_{83}B_{17}$ eutectic composition melts at $T_{eut.}$ = 1088 °C. However, it has been observed to melt at 1048 °C upon contact heating on TiB_2 ceramic in the present study. Such a decrease of the melting temperature is supposed to be mainly caused by diffusion of Ti atoms from TiB_2 substrate into the $Ni_{83}B_{17}$ sample and compositional change from the binary to a ternary alloy with a relatively low melting temperature. Indeed, the melting temperature of 1048 °C very well agrees with the eutectic temperature of 1044 °C for the $Ni_{80.7}B_{16.3}Ti_3$ ternary alloy calculated using the TDB from Ref. [195]. A similar behavior (decreasing of the melting temperature) has been observed for pure Ni and Ti on TiB_2 ceramic discussed in previous chapters. The $Ni_{50}B_{50}$ alloy started melting at about 987 °C and became completely molten at 1002 °C within the

subsequent 1.5 min heating. This temperature is muh closer to the eutectic temperature for the compositions between Ni_4B_3 and NiB phases ($T_{eut.}$ = 1018 °C) than to the melting temperature of NiB compound (1033 °C) [195]. This suggests that the concentration of B in the master alloy might be somewhat less than 50 at.%.

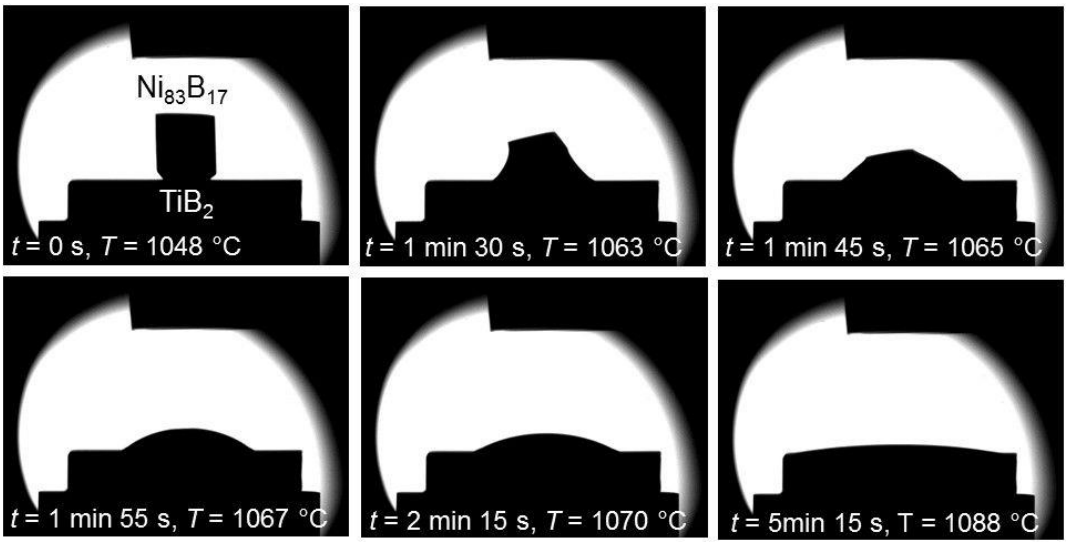

Fig. 6.2.1. $Ni_{83}B_{17}$ alloy on TiB_2 ceramic upon approaching temperature of 1105 °C. Time t = 0 sec corresponds to the solid state just before melting.

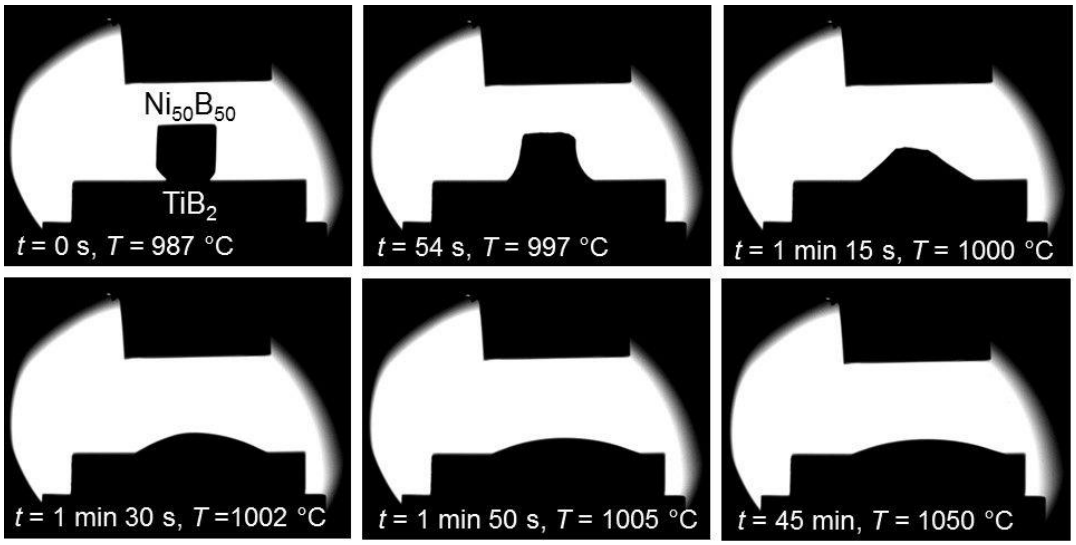

Fig. 6.2.2. $Ni_{50}B_{50}$ alloy on TiB_2 ceramic upon approaching temperature of 1050 °C and further isothermal heating. Time t = 0 sec corresponds to the solid state just before melting.

Figure 6.2.3 shows the evolution of the contact angle and the drop dimemsions with time for the $Ni_{83}B_{17}$ and $Ni_{50}B_{50}$ alloys on the TiB_2 substrates. For clarity of presentation, the time count has been set to zero at the moment when the Ni-B melt was visually observed by analysis of the digital photographs. The changes of the contact angle as well as of the drop dimensions shows three different stages for the $Ni_{83}B_{17}$ alloy on the TiB_2 substrate. Within the first 2 min from the beginning of melting, the contact angle decreased to about 20°. Then, it slowly decreased by about 10° in 10 min, and continued a very slow decrease during the next 30 min of isothermal heating at 1105 °C (Fig. 6.2.1 and Fig. 6.2.3a). The $Ni_{50}B_{50}$ melt also formed a contact angle of about 20° within the first 2 min. However, this angle remained virtually unchanged till the end of the test (Fig. 6.2.2 and Fig. 6.2.3b). Such a different behavior can be well understood after analysis of the microstructure and phases formed at the corresponding Ni-B/TiB_2 interfaces.

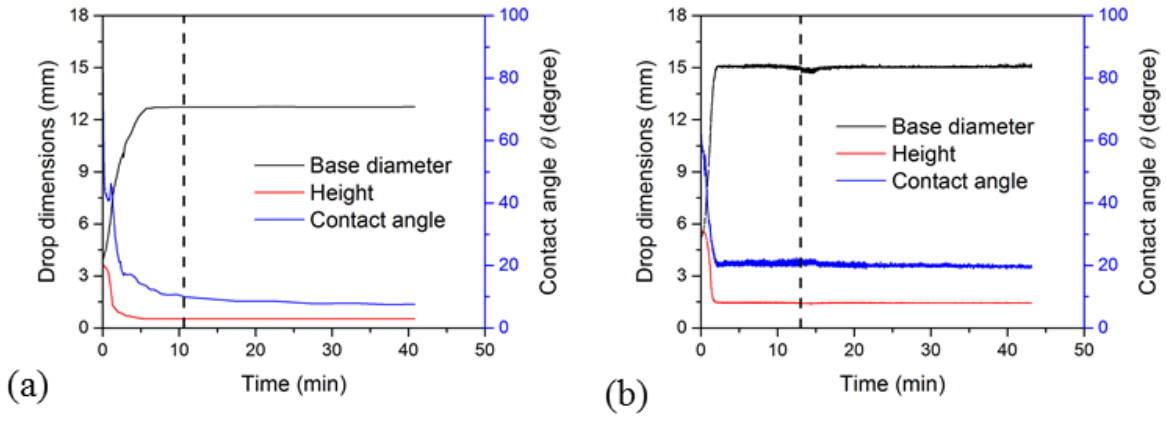

Fig. 6.2.3. Time dependence of the contact angle and corresponding drop dimensions for liquid $Ni_{83}B_{17}$ (a) and $Ni_{50}B_{50}$ (b) by heating to 1105 °C and 1050 °C, respectively. Time t = 0 corresponds to the very first moment of incipient melting visually observed on the digital photographs. Vertical *dash lines* mark the beginning of isothermal heating.

Interfacial microstructure

The SEM images taken from the cross sections of the solidified Ni-B/TiB_2 couples are presented in Figs. 6.2.4, 6.2.5 and 6.2.6. The $Ni_{50}B_{50}$/TiB_2 couple shows a macroscopically flat

and sharp interface (Fig. 6.2.4b), whereas the $Ni_{83}B_{17}/TiB_2$ interface is slightly curved (Fig. 6.2.4a). Such a sigmoidal interface profile is characteristic for reactive wetting through dissolutive mechanism, in which a competition between dissolution of substrate in a liquid phase and spreading of the liquid over the substrate takes place [139, 168, 195, 224-228].

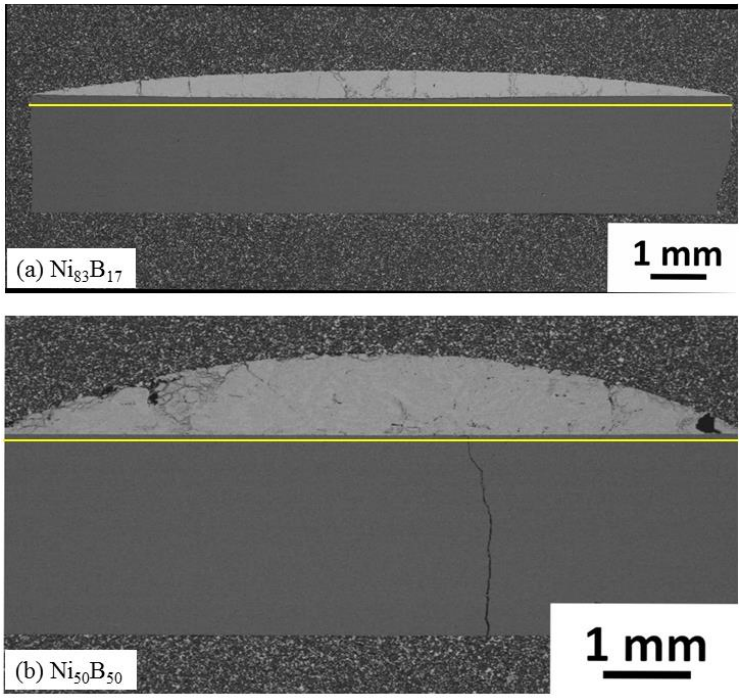

Fig. 6.2.4. SEM micrographs of the cross-sectioned couples: (a) $Ni_{83}B_{17}/TiB_2$; (b) $Ni_{50}B_{50}/TiB_2$. The *straight lines* are drawn near the interfaces to higlight dissolution of TiB_2 ceramic in the melts.

A closer examination of the cross-sectioned $Ni_{83}B_{17}/TiB_2$ couple by SEM/EDX analysis (Fig. 6.2.5) shows that the interface became rougher after the melt/ceramic interaction. The EDX maps of Ni and Ti (Figs. 6.2.5b, c) as well as the line-scan across the $Ni_{83}B_{17}/TiB_2$ interface (Fig. 6.2.7a) reveal Ti in the drop, while no Ni is detected in the TiB_2 ceramic. Supposedly, a small amount of TiB_2 was dissolved in a ternary liquid formed upon heating/melting of the $Ni_{83}B_{17}$ alloy on TiB_2 ceramic. As a consequence, the solidified drop is constituted, as shown in the optical micrograph in Fig. 6.2.5d, by Ni (phase A), Ni_3B (phase B) and a ternary compound $Ni_{21}Ti_2B_6$ (phase C). The presence of only these phases is also verified by the corresponding diffraction peaks on the XRD pattern in Fig. 6.2.8a. This result is in good agreement with the Ni-

Ti-B phase diagram calculated using the TDB from Ref. [195] and correlates with the study of $Ni_{83}B_{17}$/HfB_2 couple heated to 1520 °C in work [227].

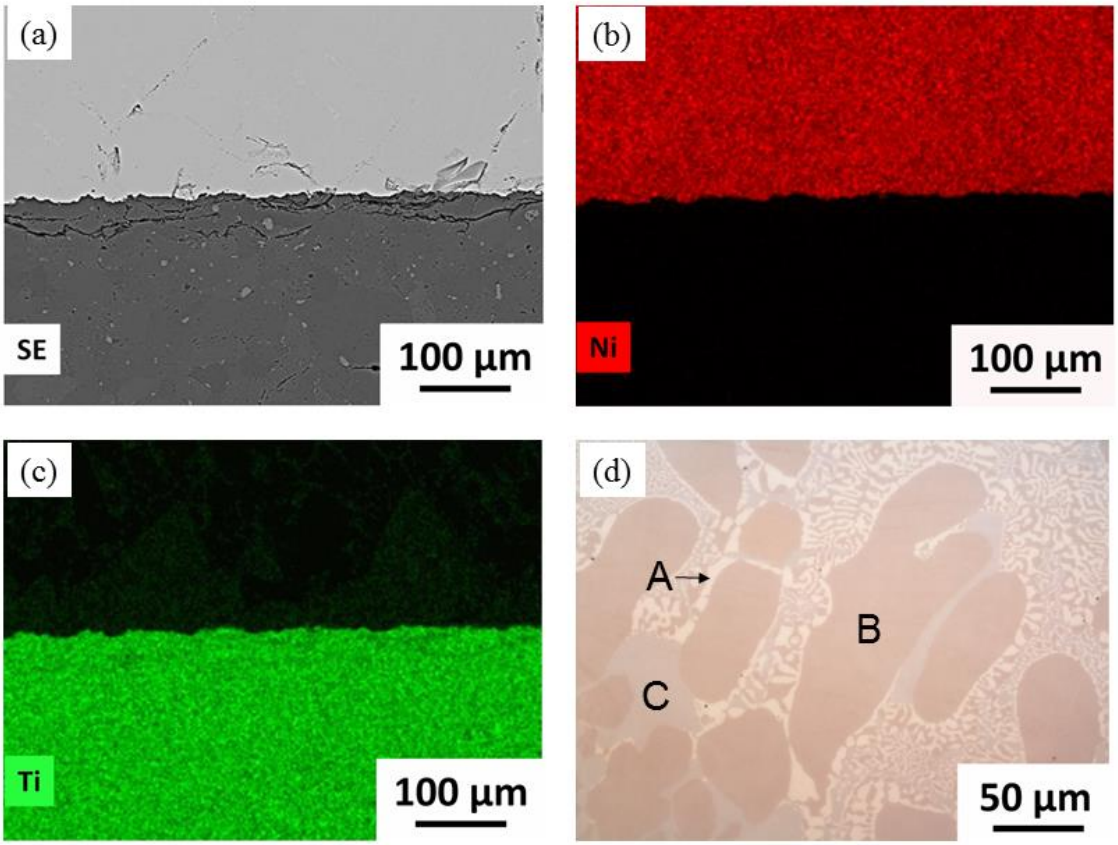

Fig. 6.2.5. $Ni_{83}B_{17}$/TiB_2 interface: (a) SEM image; (b) and (c) EDX mapping of Ni and Ti distribution in the interfacial region; (d) optical micrograph elucidating the constitution of the solidified drop: phase *A* – Ni, phase *B* – Ni_3B, phase *C* – $Ni_{21}Ti_2B_6$.

In contrast to the $Ni_{83}B_{17}$/TiB_2 case, there is no trace of substrate dissolution observed in the $Ni_{50}B_{50}$/TiB_2 couple. The interface is smooth and Ti is absent in the solidified drop, as it is seen from the SEM images and EDX mapping in Figs. 6.2.4 and 6.2.6. Also, the EDX line-scan shows a steep change of Ti concentration across the $Ni_{50}B_{50}$/TiB_2 interface (Fig. 6.2.7b). This finding suggests that $Ni_{50}B_{50}$ melt does not dissolve TiB_2 ceramic under the experimental conditions of this study, at least in the limit of EDX detection. It agrees with the thermodynamic calculations, showing almost zero solubility of TiB_2 in $Ni_{50}B_{50}$ at 1050 °C [195]. Similarly, absence of ZrB_2 solubility in $Ni_{50}B_{50}$ melt was reported in Ref. [226].

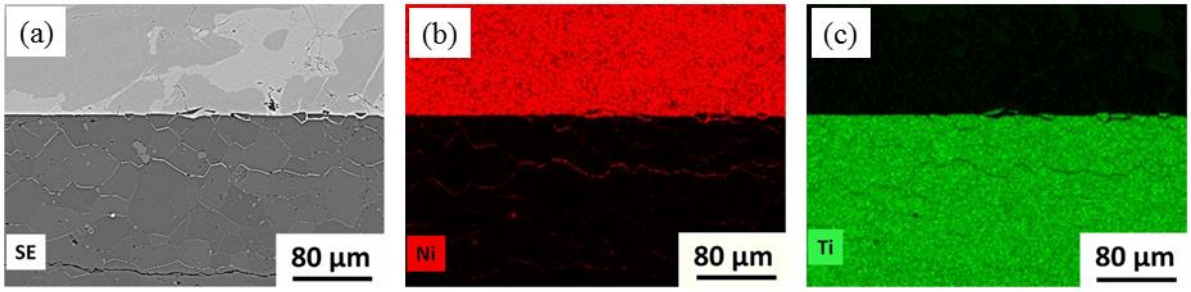

Fig. 6.2.6. $Ni_{50}B_{50}/TiB_2$ interface: (a) SEM image showing Ni_4B_3 (*grey*) and NiB (*light grey*) eutectic phases in the solidified drop and penetration of the $Ni_{50}B_{50}$ melt along grain boundaries in TiB_2 ceramic; (b) and (c) EDX mapping of Ni and Ti distribution in the interfacial region.

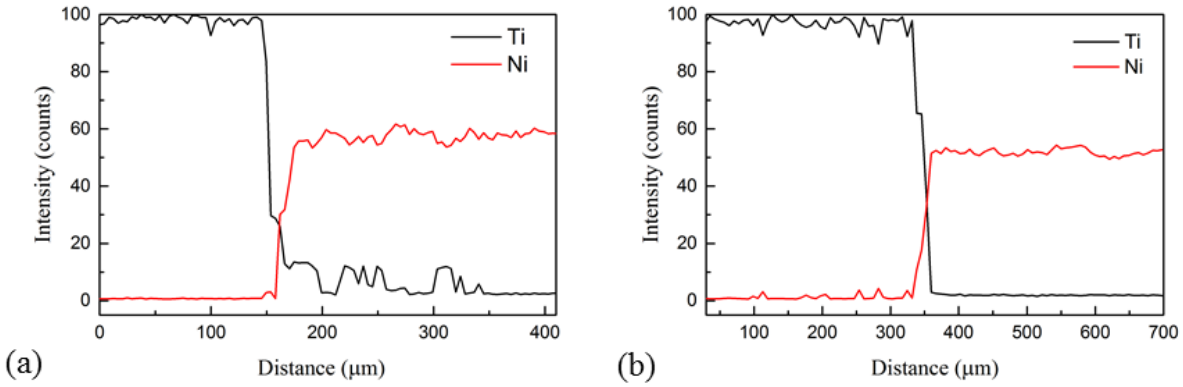

Fig. 6.2.7. EDX line analysis across the $Ni_{83}B_{17}/TiB_2$ (a) and $Ni_{50}B_{50}/TiB_2$ (b) intefaces. (Boron content is not analysed here).

Another remarkable feature of the $Ni_{50}B_{50}/TiB_2$ interface is penetration of the $Ni_{50}B_{50}$ melt along the grain boundaries in the TiB_2 ceramic (Fig. 6.2.6), as it was observed in the Ti-Al/TiB_2 interaction studied by the same technique recently [129, 168]. The $Ni_{50}B_{50}$ penetration in the TiB_2 ceramic extended up to a depth of about 200 µm from the interface (see SEM/EDX images in Fig. 6.2.6).

The XRD pattern taken from the near-interface area of the cross-sectioned $Ni_{50}B_{50}/TiB_2$ couple did not reveal any reaction product. All reflections correspond to the Ni_4B_3, NiB and TiB_2 phases (Fig. 6.2.8b). A similar drop structure was reported in the study of $Ni_{50}B_{50}/HfB_2$ system [225], where the metallic alloy was constituted by the eutectic Ni_4B_3 and NiB phases.

Thermo-mechanical compatibility of brazing alloys and joining materials is essential for the stability and performance of the joints [198]. In the $Ni_{83}B_{17}/TiB_2$ couple, multiple micro-cracks are found to develop at the interface (Fig. 6.2.5a). In this view, using $Ni_{83}B_{17}$ alloy as a filler material would result in unreliable and unfavorable bonding of TiB_2 ceramics. $Ni_{50}B_{50}$ alloy shows a much better performace as a potential candidate for joining of TiB_2 ceramics. Just one microscopic crack was found at a distance of about 160 μm from the $Ni_{50}B_{50}/TiB_2$ interface (Fig. 6.2.6a), while the interface remained intact. Furthermore, the grain boundaries penetration of the $Ni_{50}B_{50}$ melt in ceramic may provide an additional reinforcement of the interfacial structure and improvement of joint reliability.

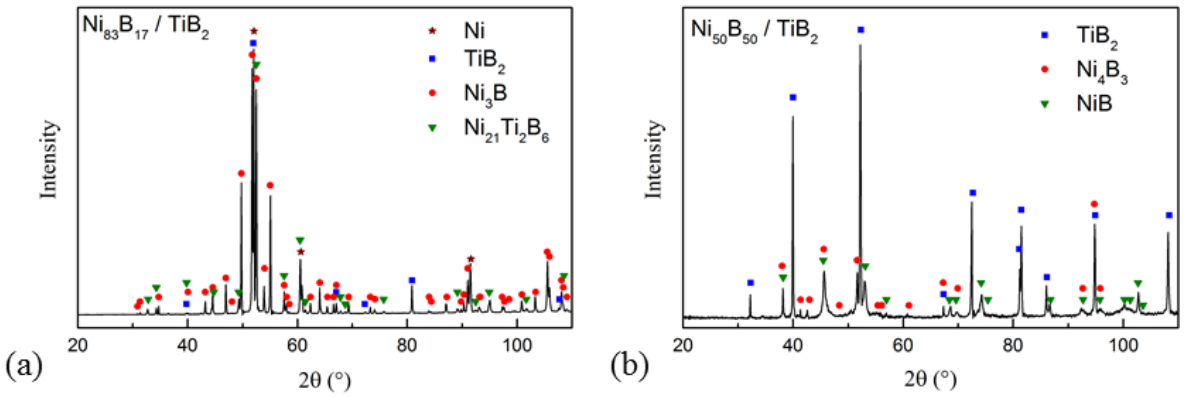

Fig. 6.2.8. XRD patterns measured from the cross-sectioned couples after the sessile-drop tests: (a) $Ni_{83}B_{17}/TiB_2$; (b) $Ni_{50}B_{50}/TiB_2$.

6.2.3 Joining

The above results of the wetting study suggest that $Ni_{50}B_{50}$ alloy could be suitable for joining of TiB_2 ceramics. In this view, a preliminary experiment of joining TiB_2 ceramics using $Ni_{50}B_{50}$ ribbons as an interlayer was performed. The $Ni_{50}B_{50}$ ribbons were prepared by melt spinning technique.

A certain amount of $Ni_{50}B_{50}$ ribbon was placed on the polished substrate and sandwiched as an interlayer between the TiB_2 substrates as shown schematically in Fig. 6.2.9a. A specific weight was applied to give a pressure of 20 MPa on the assembly. The assembly was placed in a

graphite furnace in vacuum and heated to 1050 °C, followed by holding for 30 min and cooled down to room temperature.

The cross-sectioned TiB_2/TiB_2 joint revealed an intimate contact and a good adhesion of the filler alloy to the ceramic parts. A filler alloy with a thickness of about 6.5 μm was observed as it is seen in Fig. 6.2.10. It is noteworthy that there was no pronounced change of the thickness observed at the overall interface. Similar to the $Ni_{50}B_{50}$/TiB_2 couple after the wetting test, the alloy melt penetrated along the grain boundaries in the ceramic, extending up to a depth of about 200 μm from the interface at the joining conditions.

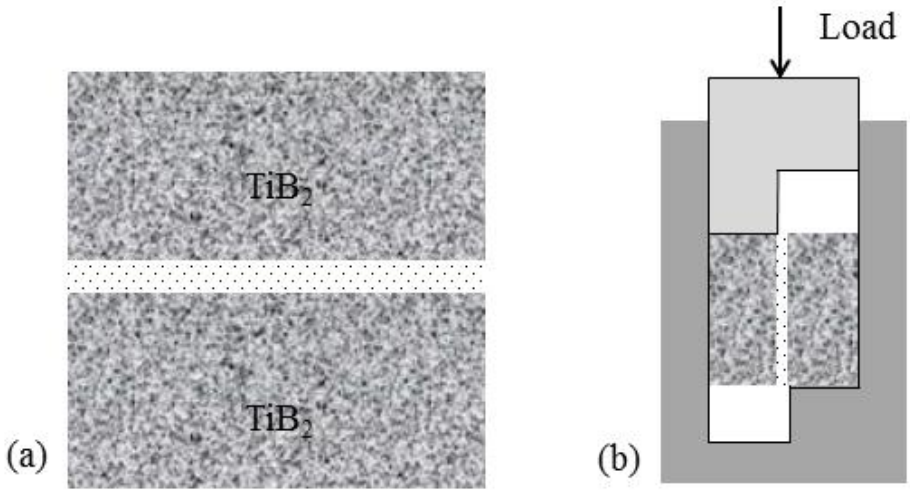

Fig. 6.2.9. Schematic illustrations of the sandwich structure for joining test (a) and the steel mould for shear test (b).

The quality of the joining was estimated by a shear test. The shear test was carried out at room temperature using a steel frame (Fig. 6.2.9b) attached to an INSTRON 5869 machine with a loading speed of 0.06 mm · min^{-1}. The shear strength was calculated from the value of load divided by the overlap area. In the shear tests, TiB_2/$Ni_{50}B_{50}$/TiB_2 joints showed a shear strength between 230 and 360 MPa. The values measured in this study are much higher than those obtained for ZrB_2/Ni/ZrB_2 and HfB_2/NiB50/HfB_2 specimens [34, 225]. Muolo *et al.* [225] studied the joining of HfB_2 ceramics using NiB50 alloy at 1300 °C and obtained a shear strength at room temperature ranging from 70 to 170 MPa.

The observation of the fractured surface (Fig. 6.2.11) revealed that cracks initiated and then propagated mainly along the ceramic part. A brittle failure in the shear test may be caused by thermal stress developed in the ceramic during cooling or weakly bonded TiB_2 grains. This suggests that the interface at the joint area between the alloy and TiB_2 ceramic was superior.

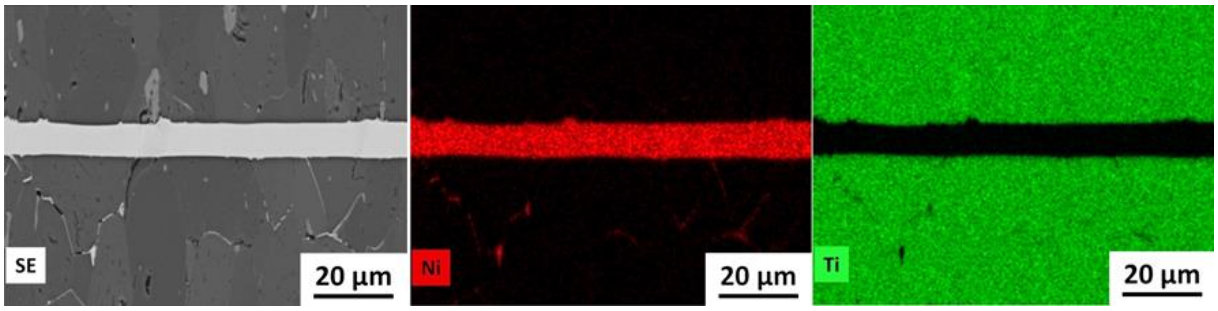

Fig. 6.2.10. Interfacial microstructure of $TiB_2/Ni_{50}B_{50}/TiB_2$ joint by SEM/EDX.

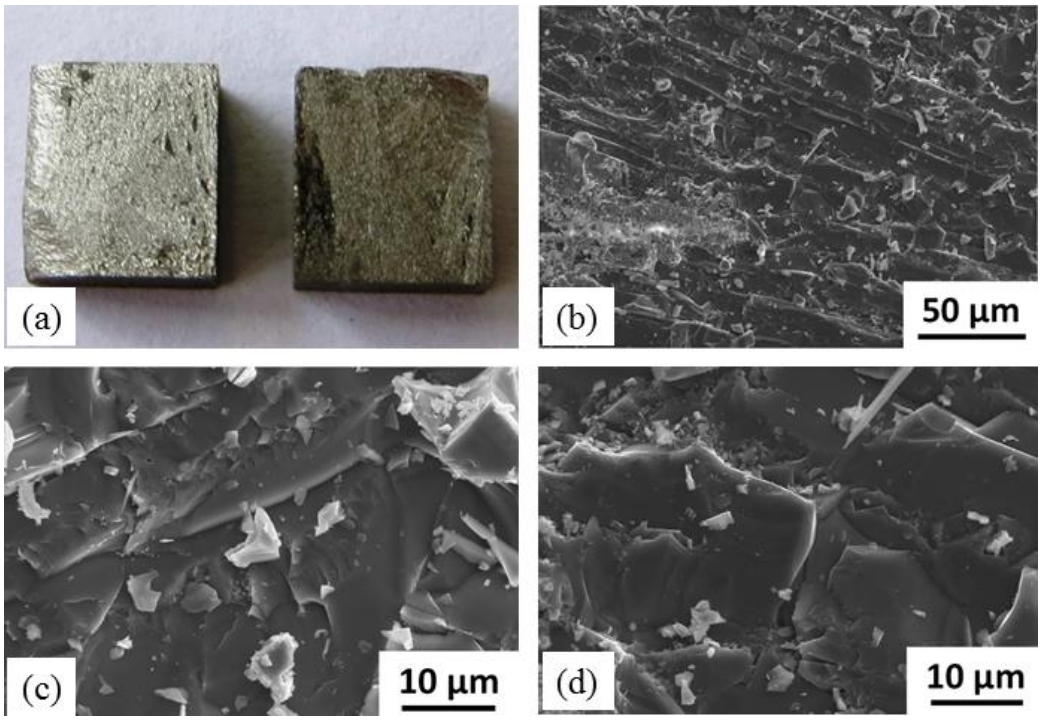

Fig. 6.2.11. Images of the fractured $TiB_2/Ni_{50}B_{50}/TiB_2$ sample: (a) digital photograph of a sample after failure; (b)-(d) SEM images taken from the fractured surface.

6.2.4 Conclusions

The sessile drop investigations of the melting and wetting behavior of $Ni_{83}B_{17}$ and $Ni_{50}B_{50}$ alloys on the TiB_2 substrates were carried out upon heating to 1105 °C and 1050 °C, respectively. The following conclusions are drawn from:

1. Liquid $Ni_{83}B_{17}$ and $Ni_{50}B_{50}$ alloys wet very well TiB_2 ceramic after an incipient melting.

2. A small amount of TiB_2 is dissolved when $Ni_{83}B_{17}$ alloy is contact-heated and molten on TiB_2 ceramic. This results in formation of a ternary $Ni_{21}Ti_2B_6$ phase.

3. Liquid $Ni_{50}B_{50}$ alloy does not dissolve TiB_2, but penetrates along the grain boundaries of the substrate, extending up to a depth of about 200 μm from the $Ni_{50}B_{50}/TiB_2$ interface.

4. TiB_2 ceramics have been successfully joined using $Ni_{50}B_{50}$ melt-spun ribbon as an interlayer and good mechanical performance was obtained for the $TiB_2/Ni_{50}B_{50}/TiB_2$ joint, showing a shear strength between 230 and 360 MPa.

Chapter 7: Summary and outlook

In this work, systematic investigations of the wetting and interfacial interactions of molten Al, Ti-Al, Ni-Al and Ni-B alloys with TiB_2 ceramic have been performed by the sessile drop method. The study considers both fundamental issues such as wettability kinetics and interfacial microstructure and application-oriented problems related to composite synthesis and joining of ceramics. Below is a summary of the results obtained:

1. The wetting behavior of TiB_2 ceramic by liquid Al in a wide temperature range from 700 to 1400 °C have been studied using classical sessile drop and dispensed drop techniques. The results showed that the wetting was significantly accelerated with an increase in temperature. A difference of the wetting temperature by these two techniques was about 300 °C due to the native oxide film present on the Al surface in classical sessile drop technique accompanied with contact heating. Starting from 1000 °C, when the oxide film is in situ destroyed or removed from the drop surface, liquid Al either filled the inter-grain pores or penetrated along the grain boundaries of the TiB_2 substrate but no reaction has been observed in the Al/TiB_2 system. These observations made a base for further investigations of high-temperature interactions of molten Al-containing metallic alloys with TiB_2 ceramic.

2. The high-temperature interactions of liquid Ti and Ti-Al alloys ($Ti_{74.3}Al_{25.7}$, $Ti_{49.3}Al_{50.7}$, $Ti_{26.5}Al_{73.5}$ and $Ti_{3.5}Al_{96.5}$, at.%) with TiB_2 ceramic were investigated using classical sessile drop technique. Molten Ti and Ti-Al alloys showed a very good wetting of TiB_2 ceramics. A homogenous TiB layer with a thickness of about 20 μm was formed at the Ti/TiB_2 interface while an approximately 200-μm-thick layer of densely packed TiB whiskers was observed at the interface of a $Ti_{74.3}Al_{25.7}$/TiB_2 couple. In contrast, no reaction product was detected from the solidified Al-rich/TiB_2 couples but liquid Al-rich alloys either penetrated the grain boundaries or filled the pores in the ceramic in the near-interface region. Micro- and macroscopic cracks were formed in the Ti-Al/TiB_2 couples after the wetting tests due to a thermal expansion coefficient mismatch and high solidification temperatures of the Ti-Al alloys.

3. For the Ni-Al/TiB_2 system, the wetting and interfacial interactions between Ni-Al melts and TiB_2 ceramic have been studied by a dispensed drop technique. In the case of pure Ni and Ni-rich melts, TiB_2 ceramic and minor TiC_x sintering aids were dissolved and precipitated

inside the drops as well as on their surface upon cooling. An increase in Ni content in the Ni-Al alloys caused notable substrate dissolution in the melts and a gradual appearance of a sigmoidal interface profile. Instantaneous spreading occurred when the drops of $Ni_{50}Al_{50}$ and $Ni_{40}Al_{60}$ alloys were dispensed onto the TiB_2 substrates at a temperature above 1600 °C. Minor recrystallized TiB_2 crystals in form of hexagonal and facet crystals, were found to precipitate in the $Ni_{50}Al_{50}/TiB_2$ system. Liquid Al-rich alloys wet well TiB_2 substrates and the interfaces remained macroscopically smooth and planar, confirming the absence of any chemical reaction between the alloy and the ceramic. It concludes that the behavior of liquid Ni-Al alloys on TiB_2 ceramic changes from a dissolutive, reactive wetting on the Ni-rich side to a non-reactive wetting on the Al-rich side.

4. The melting and wetting behavior of $Ni_{83}B_{17}$ and $Ni_{50}B_{50}$ alloys on TiB_2 ceramic were investigated in view of possible joining of TiB_2 ceramics. Both alloys wet very well TiB_2 ceramic immediately after an incipient melting. Liquid $Ni_{50}B_{50}$ alloy was revealed not to dissolve TiB_2 but penetrated along the grain boundaries into the ceramic. Upon melting of the $Ni_{83}B_{17}$ alloy on TiB_2, a small amount of TiB_2 was dissolved and the ternary $Ni_{21}Ti_2B_6$ phase was formed. Whereas multiple micro-cracks were observed at the $Ni_{83}B_{17}/TiB_2$ interface, the $Ni_{50}B_{50}/TiB_2$ couple was well-bonded and free of interfacial micro-cracks. TiB_2 ceramics have been successfully joined using $Ni_{50}B_{50}$ melt-spun ribbon as an interlayer and a good mechanical performance was obtained for the $TiB_2/Ni_{50}B_{50}/TiB_2$ joint, showing shear strength between 230 and 360 MPa.

This thesis yields an experimental evaluation of the wetting and interfacial interactions, and provide a better understanding of the interaction mechanism in the metal/ceramic systems. Two essential factors affecting the evolution of the wetting and metal/ceramic interface in these systems are testing conditions and chemical composition of the melt. On the one hand, the wetting in the Al/TiB_2 system is mainly affected by the sessile drop method and temperature. On the other hand, the Al content in either Ti-Al or Ni-Al alloys affects the development of the interfacial microstructure by either liquid penetration in the ceramic or substrate dissolution. These factors should be considered by fabrication of $Ti\text{-}Al/TiB_2$ and $Ni\text{-}Al/TiB_2$ composite materials and joining of TiB_2 ceramics.

Although the wetting and interfacial interactions in a variety of metal/ceramic systems have been already studied rather extendedly, some issues still remain challenging and further work is still needed in terms of the following aspects:

1. For the sessile drop method used in this study, further improvements are expected to be made in the near future. It includes the development of new devices where the sessile drop experiments can be coupled with high-temperature analysis techniques, in particular in-situ X-ray diffraction. This would be extremely useful for understanding the reaction steps and formation of the new phases at the metal/ceramic interface in reactive wetting.

2. Investigations on the wetting and interfacial interactions in one system by combination of experiments, theory and numerical simulations remain to be done.

3. For reactive systems, wetting and interfacial reactions are interrelated and the effects of interfacial reactions, diffusion of constituents, and substrate dissolution on the evolution of wetting kinetics are essential to be quantified.

4. For the TiB_2/NiB/TiB_2 joints, the jointing effects remain to be evaluated by tensile and bending tests.

References

[1] L. Leger and J. Joanny, Liquid spreading, Reports on Progress in Physics **55**, 431-86 (1992).

[2] G. Kumar and K. N. Prabhu, Review of non-reactive and reactive wetting of liquids on surfaces, Adv Colloid Interface Sci **133**, 61-89 (2007).

[3] B. He, J. Lee and N. A. Patankar, Contact angle hysteresis on rough hydrophobic surfaces, Colloid Surf A **248**, 101-4 (2004).

[4] J. Kijlstra, K. Reihs and A. Klamt, Roughness and topology of ultra-hydrophobic surfaces, Colloid Surf A **206**, 521-9 (2002).

[5] N. Eustathopoulos, Wetting by liquid metals-application in materials processing: The contribution of the grenoble group, Metals **5**, 350-70 (2015).

[6] R. Mitra and Y. Mahajan, Interfaces in discontinuously reinforced metal matrix composites: An overview, Bull Mater Sci **18**, 405-34 (1995).

[7] R. Israel, R. Voytovych, P. Protsenko, B. Drevet, D. Camel and N. Eustathopoulos, Capillary interactions between molten silicon and porous graphite, J Mater Sci **45**, 2210-7 (2010).

[8] C. Huguet, C. Dechamp, R. Voytovych, B. Drevet, D. Camel and N. Eustathopoulos, Initial stages of silicon–crucible interactions in crystallisation of solar grade silicon: Kinetics of coating infiltration, Acta Mater **76**, 151-67 (2014).

[9] H. Schmidt, S. Langenfeld and R. Naß, A new corrosion protection coating system for pressure-cast aluminium automotive parts, Mater Des **18**, 309-13 (1997).

[10] H. Holleck and V. Schier, Multilayer PVD coatings for wear protection, Surf Coat Technol **76–77, Part 1**, 328-36 (1995).

[11] D. P. Sekulić, Advances in brazing: science, technology and applications, Elsevier, 2013).

[12] E. Ghasali, A. Pakseresht, F. Safari-Kooshali, M. Agheli and T. Ebadzadeh, Investigation on microstructure and mechanical behavior of Al–ZrB_2 composite prepared by microwave and spark plasma sintering, Mater Sci Eng A **627**, 27-30 (2015).

[13] D. Kalinski, M. Chmielewski, K. Pietrzak and K. Choregiewicz, An influence of mechanical mixing and hot-pressing on properties of NiAl/Al_2O_3 composite, Archives of

Metallurgy and Materials **57**, 695-702 (2012).

[14] T. Lee and C. Lee, Microstructure and mechanical properties of TiB_2/TiAl composites produced by reactive sintering using a powder extrusion technique, J Mater Sci Lett **18**, 801-3 (1999).

[15] K. Panda and K. R. Chandran, Titanium-titanium boride (Ti-TiB) functionally graded materials through reaction sintering: Synthesis, microstructure, and properties, Metall Mater Trans A **34**, 1993-2003 (2003).

[16] H. Attar, M. Bönisch, M. Calin, L. Zhang, K. Zhuravleva, A. Funk, S. Scudino, C. Yang and J. Eckert, Comparative study of microstructures and mechanical properties of in situ Ti–TiB composites produced by selective laser melting, powder metallurgy, and casting technologies, J Mater Res **29**, 1941-50 (2014).

[17] R. M. Wang, C. H. Tao, L. Chen and Y. F. Han, Microstructure and mechanical properties of NiAlCo–TiB_2 composites, Mater Lett **38**, 54-7 (1999).

[18] Y.-X. Qin, W.-J. Lu, X.-F. Sheng, Z.-F. Yang and D. Zhang, Mechanical properties of in situ synthesized titanium matrix composites at elevated temperature, Mater Trans **44**, 2282-7 (2003).

[19] C. Yeh and S. Su, In situ formation of TiAl–TiB_2 composite by SHS, J Alloys Compd **407**, 150-6 (2006).

[20] E. Alexander, S. Christopher and M. Andreas, Metal matrix composites in industry: an introduction and a survey, Nor well: Kluwer Academic Publishers (2003).

[21] A. Mortensen, Melt infiltration of metal matrix composites, Comprehensive composite materials **3**, 521-4 (2000).

[22] D. Gu, H. Wang, F. Chang, D. Dai, P. Yuan, Y.-C. Hagedorn and W. Meiners, Selective laser melting additive manufacturing of TiC/AlSi10Mg bulk-form nanocomposites with tailored microstructures and properties, Phys Procedia **56**, 108-16 (2014).

[23] Y. Chen and H. Wang, Laser melted TiC reinforced nickel aluminide matrix in situ composites, J Alloys Compd **391**, 49-54 (2005).

[24] K. Trumble, Spontaneous infiltration of non-cylindrical porosity: close-packed spheres, Acta Mater **46**, 2363-7 (1998).

[25] G. Kaptay and T. Bárczy, On the asymmetrical dependence of the threshold pressure of infiltration on the wettability of the porous solid by the infiltrating liquid, J Mater Sci **40**, 2531-5

(2005).

[26] A. Joshi, H. Hu, L. Jesion, J. Stephens and J. Wadsworth, High-temperature interactions of refractory metal matrices with selected ceramic reinforcements, Metall Trans A **21**, 2829-37 (1990).

[27] A. G. Metcalfe, ed. Interfaces in metal matrix composites, New York, Academic Press (1974).

[28] C. Ward-Close, R. Minor and P. Doorbar, Intermetallic-matrix composites-a review, Intermetallics **4**, 217-29 (1996).

[29] B. Basu and K. Balani, Advanced structural ceramics, John Wiley & Sons, (2011).

[30] J. F. Justin and A. Jankowiak, Ultra high temperature ceramics: densification, properties and thermal stability, Aerospace Lab **3** 1-11 (2011).

[31] N. Gupta, B. Basu, V. B. Prasad and M. Vemuri, Ballistic studies on TiB_2-Ti functionally graded armor ceramics, Def Sci J **62**, 382-9 (2012).

[32] A. V. Smith and D. D. L. Chung, Titanium diboride particle-reinforced aluminium with high wear resistance, J Mater Sci **31**, 5961-73 (1996).

[33] E. Bayraktar, D. Katundi, F. Ayari, J. Chevalier and F. Bonnet, Damage analysis of the ceramic reinforced steel matrix composites sheets: experimental and numerical study, Experimental and Applied Mechanics, Volume 6, Springer, (2011).

[34] B. Yuan and G.-J. Zhang, Microstructure and shear strength of self-joined ZrB_2 and ZrB_2–SiC with pure Ni, Scripta Mater **64**, 17-20 (2011).

[35] N. Saito, H. Ikeda, Y. Yamaoka, A. M. Glaeser and K. Nakashima, Wettability and transient liquid phase bonding of hafnium diboride composite with Ni–Nb alloys, J Mater Sci **47**, 8454-63 (2012).

[36] R. Asthana and M. Singh, Joining of ZrB_2-based ultra-high-temperature ceramic composites using Pd-based braze alloys, Scripta Mater **61**, 257-60 (2009).

[37] W. R. Pinc, M. Di Prima, L. S. Walker, Z. N. Wing and E. L. Corral, Spark plasma joining of ZrB_2–SiC composites using zirconium–boron reactive filler layers, J Am Ceram Soc **94**, 3825-32 (2011).

[38] X. Huang, Z. Zhao and L. Zhang, Fusion bonding of solidified TiC–TiB_2 ceramic to Ti–6Al–4V alloy achieved by combustion synthesis in high-gravity field, Mater Sci Eng A **564**, 400-7 (2013).

[39] Y. Peng, Z. Y. Fu, W. M. Wang, H. Wang, Y. C. Wang, J. Y. Zhang and Q. J. Zhang, Joining TiB_2-Ni cermets with Ti6Al4V by pulse current heating, Key Eng Mater **368**, 1609-11 (2008).

[40] American Welding Society C3 Committee on Brazing Soldering, Brazing Handbook Fifth Edition, (AWS2007), Chapter 1,2., (2007).

[41] I. A. Aksay, C. E. Hoge and J. A. Pask, Wetting under chemical equilibrium and nonequilibrium conditions, J Phys Chem **78**, 1178-83 (1974).

[42] J. V. Naidich, The wettability of solids by liquid metals In: D. A. Cadenhead and J. F. Danielli, eds, Progress in surface and membrane science, New York, Academic Press, (1981).

[43] M. Nicholas, Interactions at oxide-metal interfaces, Mater Sci Forum, Trans Tech Publ, p. 127-50.

[44] P. Scott, M. Nicholas and B. Dewar, The wetting and bonding of diamonds by copper-base binary alloys, J Mater Sci **10**, 1833-40 (1975).

[45] K. C. Russell, S. Oh and A. Figueredo, Theoretical and experimental studies of ceramic: metal wetting, MRS Bulletin **16**, 46-52 (1991).

[46] A. Tomsia, Ceramic/metal joining for structures and materials, Le Journal de Physique IV **3**, C7-1317-C7-26 (1993).

[47] F. Yost and A. Romig, Thermodynamics of wetting by liquid metals, MRS Proceedings, Cambridge Univ Press, **108**, 385-90 (1987).

[48] B. Dalgleish, E. Saiz, A. Tomsia, R. Cannon and R. Ritchie, Interface formation and strength in ceramic-metal systems, Scr Metall Mater **31**, 1109-14 (1994).

[49] N. Sobczak, M. Ksiazek, W. Radziwill, L. Stobierski and B. Mikulowski, Wetting-bond strength relationship in Al-AlN system, Trans JWRI **30** 125-30 (2001).

[50] N. Sobczak, M. Ksiazek, W. Radziwill, R. Asthana and B. Mikulowski, The effect of temperature, matrix alloying and substrate coatings on wettability and shear strength of Al/Al_2O_3 couples, Metall Mater Trans A **35**, 911-23 (2004).

[51] N. Sobczak and R. Asthana, The role of interfacial phenomena in wetting-bonding relationship in Al/ceramic couples, Surfaces, Interfaces, and the Science of Ceramic Joining, Volume 158 1-17 (2004).

[52] N. Sobczak, R. Asthana, W. Radziwill, R. Nowak and A. Kudyba, The role of aluminium oxidation in the wetting-bonding relationship of Al oxide couples, Arch Metall Mater **52**, 55-65

(2007).

[53] www.substech.com,

[54] F. Harding and D. Rossington, Wetting of ceramic oxides by molten metals under ultrahigh vacuum, J Am Ceram Soc **53**, 87-90 (1970).

[55] S. Ip, M. Kucharski and J. Toguri, Wetting behaviour of aluminium and aluminium alloys on Al_2O_3 and CaO, J Mater Sci Lett **12**, 1699-702 (1993).

[56] J. Wojewoda-Budka, N. Sobczak, B. Onderka, J. Morgiel and R. Nowak, Interaction between liquid aluminum and yttria substrate: microstructure characterization and thermodynamic considerations, J Mater Sci **45**, 2042-50 (2010).

[57] A. Durov, Y. Naidich and B. Kostyuk, Investigation of interaction of metal melts and zirconia, J Mater Sci **40**, 2173-8 (2005).

[58] M. Ueki, M. Naka and I. Okamoto, Wettability of some metals against zirconia ceramics, J Mater Sci Lett **5**, 1261-2 (1986).

[59] A. Greer, A. Bunn, A. Tronche, P. Evans and D. Bristow, Modelling of inoculation of metallic melts: Application to grain refinement of aluminium by Al–Ti–B, Acta Mater **48**, 2823-35 (2000).

[60] D. Gosslar, R. Günther, U. Hecht, C. Hartig and R. Bormann, Grain refinement of TiAl-based alloys: The role of TiB_2 crystallography and growth, Acta Mater **58**, 6744-51 (2010).

[61] I. Kaban, M. Köhler, L. Ratke, W. Hoyer, N. Mattern, J. Eckert and A. Greer, Interfacial tension, wetting and nucleation in Al–Bi and Al–Pb monotectic alloys, Acta Mater **59**, 6880-9 (2011).

[62] L. Wang and R. Arsenault, Interfaces in XD processed TiB_2/NiAl composites, Metall Trans A **22**, 3013-8 (1991).

[63] S. Rhee, Wetting of ceramics by liquid aluminum, J Am Ceram Soc **53**, 386-9 (1970).

[64] G. Samsonov, A. Panasyuk and M. Borovikova, Investigation of the wetting process of metallikeborides by liquid metals, Poroshk Metall **5**, 61-7 (1973).

[65] D. Weirauch, W. Krafick, G. Ackart and P. Ownby, The wettability of titanium diboride by molten aluminum drops, J Mater Sci **40**, 2301-6 (2005).

[66] R. Dorward, Aluminum penetration and fracture of titanium diboride, J Am Ceram Soc **65**, C-6 (1982).

[67] W. A. Zdaniewski, Role of microstructure and intergranular phases in stress corrosion of

TiB_2 exposed to liquid aluminum, J Am Ceram Soc **68**, C-309-C-12 (1985).

[68] K. Nord-Varhaug, TEM investigation of impurity phases and the penetration of liquid aluminum in hot isostatically pressed TiB_2 compacts, J Am Ceram Soc **79**, 1147-54 (1996).

[69] H. Heidari, H. Alamdari, D. Dubé and R. Schulz, Interaction of molten aluminum with porous TiB_2-based ceramics containing Ti–Fe additives, J Eur Ceram Soc **32**, 937-45 (2012).

[70] S. Devyatkin and G. Kaptay, Chemical and electrochemical behavior of titanium diboride in cryolite-alumina melt and in molten aluminum, J Solid State Chem **154**, 107-9 (2000).

[71] N. Eustathopoulos and L. Coudurier, Wettability and Thermodynamic Adhesion in Aluminum--Aluminum Oxide System: Effect of a Coating of Titanium Diboride or Titanium Nitride, Ann Chim **10**, 1-6 (1985).

[72] G. Yasinskaya, The wetting of refractory carbides, borides, and nitrides by molten metals, Sov Powder Metall+ **5**, 557-9 (1966).

[73] G. Samsonov, A. Panasyuk and M. Borovikova, Contact reaction between refractory compounds and liquid metals, Sov Powder Metall+ **12**, 476-80 (1973).

[74] H. Kotsch, Materials for crucibles and volatilization of metals in powder metallurgy, Neue Hütte **12** 350-5 (1967).

[75] V. I. Tumanov, A. E. Gorbunov and G. M. Kondratenko, Wetting and properties of group IV and VI, metal mono- and di-borides, Russ J Phys Chem+ **44** 304 (1970).

[76] V. N. Eremenko and Y. V. Naidich, Wetting of borides and carbides with liquid metals, Russ J Inorg Chem+ **4**, 931-4 (1959).

[77] S. Sahay, K. Ravichandran, R. Atri, B. Chen and J. Rubin, Evolution of microstructure and phases in in situ processed Ti–TiB composites containing high volume fractions of TiB whiskers, J Mater Res **14**, 4214-23 (1999).

[78] P. Nandwana, Titanium boride formation and its subsequent influence on morphology and crystallography of alpha precipitates in titanium alloys, University of North Texas, Ph.D. thesis, (2013).

[79] G. C. Walther and R. Loehman, Kinetics of TiB formation, Springer, (1977).

[80] S. Gorsse, J. Chaminade and Y. Le Petitcorps, In situ preparation of titanium base composites reinforced by TiB single crystals using a powder metallurgy technique, Composites Part A: Applied Science and Manufacturing **29**, 1229-34 (1998).

[81] H.-B. Feng, D.-C. Jia, Y. Zhou and J. Huo, Microstructural characterisation of in situ

TiB/Ti matrix composites prepared by mechanical alloying and hot pressing, Mater Sci Technol **20**, 1205-10 (2004).

[82] E. Wuchina, E. Opila, M. Opeka, W. Fahrenholtz and I. Talmy, Ultra-high temperature ceramic materials for extreme environment applications, Electrochem Soc Interface **16**, 30-6 (2007).

[83] D. M. Van Wie, D. G. Drewry, Jr., D. E. King and C. M. Hudson, The hypersonic environment: Required operating conditions and design challenges, J Mater Sci **39**, 5915-24 (2004).

[84] M. M. Opeka, I. G. Talmy and J. A. Zaykoski, Oxidation-based materials selection for 2000°C + hypersonic aerosurfaces: Theoretical considerations and historical experience, J Mater Sci **39**, 5887-904 (2004).

[85] V. T. Witusiewicz, A. A. Bondar, U. Hecht, S. Rex and T. Y. Velikanova, The Al–B–Nb–Ti system: I. Re-assessment of the constituent binary systems B–Nb and B–Ti on the basis of new experimental data, J Alloys Compd **448**, 185-94 (2008).

[86] T. Hegenscheidt, Möglichkeiten und Grenzen des Röntgen-Beugungsexperiments, aufgezeigt am Beispiel dreier" einfacher" Strukturen. Universität Karlsruhe, Ph.D. thesis, (1998).

[87] R. G. Munro, Material properties of titanium diboride, J Res Natl Inst Stand Technol **105**, 709-20 (2000).

[88] ESK Ceramics GmbH & Co. KG. Titanium diboride technical data. Kempten, Germany., (2007).

[89] M. Ramachandran and R. G. Reddy, Production of nanoscale titanium diboride powders, IJMSP **11**, 15-22 (2011).

[90] I. Barin, F. Sauert, E. Schultze-Rhonhof and W. S. Sheng, Thermochemical data of pure substances, Weinheim: VCH, (1995).

[91] J. J. Moore and H. J. Feng, Combustion synthesis of advanced materials: Part I. Reaction parameters, Prog Mater Sci **39**, 243-73 (1995).

[92] S. Baik and P. F. Becher, Effect of oxygen contamination on densification of TiB_2, J Am Ceram Soc **70**, 527-30 (1987).

[93] W. Wang, Z. Fu, H. Wang and R. Yuan, Influence of hot pressing sintering temperature and time on microstructure and mechanical properties of TiB 2 ceramics, J Eur Ceram Soc **22**, 1045-9 (2002).

[94] L.-H. Li, H.-E. Kim and E. S. Kang, Sintering and mechanical properties of titanium diboride with aluminum nitride as a sintering aid, J Eur Ceram Soc **22**, 973-7 (2002).

[95] J. H. Park, Y. H. Lee, Y. H. Koh, H. E. Kim and S. Su Baek, Effect of hot-pressing temperature on densification and mechanical properties of titanium diboride with silicon nitride as a sintering aid, J Am Ceram Soc **83**, 1542-4 (2000).

[96] S. H. Kang, D. J. Kim, E. S. Kang and S. S. Baek, Pressureless sintering and properties of titanium diboride ceramics containing chromium and iron, J Am Ceram Soc **84**, 893-5 (2001).

[97] M. A. Einarsrud, E. Hagen, G. Pettersen and T. Grande, Pressureless sintering of titanium diboride with nickel, nickel boride, and iron additives, J Am Ceram Soc **80**, 3013-20 (1997).

[98] A. Petukhov, I. Khobta, A. Ragulya, A. Derevyanko, A. Raichenko, L. Isaeva and A. Koval'chenko, Reactive electric-discharge sintering of TiN-TiB_2, Powder Metall Met Ceram **46**, 525-32 (2007).

[99] J.-S. Kim, Y.-S. Kwon, O. Lomovsky, M. Korchagin, V. Mali and D. Dudina, A synthetic route for metal–ceramic interpenetrating phase composites, Mater Lett **60**, 3723-6 (2006).

[100] M. Yoshida, Influence of sintering temperature on the microstructure of TiB_2 sintered with Al_3Ti additive, Mater Trans **53**, 1648-51 (2012).

[101] J. H. Moore and N. D. Spencer, eds, Encyclopedia of chemical physics and physical chemistry: Ceramic processing, Taylor & Francis, (2001).

[102] G. B. Raju and B. Basu, Densification, sintering reactions, and properties of titanium diboride with titanium disilicide as a sintering aid, J Am Ceram Soc **90**, 3415-23 (2007).

[103] G. Pettersen, Development of microstructure during sintering and aluminium exposure of titanium diboride ceramics, Department of physics, NTNU, Norway 138 (1997).

[104] B. Basu, G. Raju and A. Suri, Processing and properties of monolithic TiB_2 based materials, Int Mater Rev **51**, 352-74 (2006).

[105] F. Monteverde and R. Savino, ZrB_2–SiC sharp leading edges in high enthalpy supersonic flows, J Am Ceram Soc **95**, 2282-9 (2012).

[106] W. G. Fahrenholtz, G. E. Hilmas, I. G. Talmy and J. A. Zaykoski, Refractory diborides of zirconium and hafnium, J Am Ceram Soc **90**, 1347-64 (2007).

[107] H. Heidari, Development of wettable cathode for aluminium smelting. Citeseer, (2012).

[108] L. S. Sigl, K. A. Schwetz and U. Dworak, Continuous turning with TiB_2 cermets: Preliminary cutting tests, Int J Refract Met Hard Mater **12**, 95-9 (1993).

[109] T. Young, An essay on the cohesion of fluids, Philosophical Transactions of the Royal Society of London **95**, 65-87 (1805).

[110] M. Ferrari, L. Liggieri and R. Miller, Drops and bubbles in contact with solid surfaces, CRC Press, (2012).

[111] N. Sobczak, Improvement of wetting and bonding of dissimilar materials, Interfacial Science in Ceramic Joining, Springer, (1998).

[112] N. Eustathopoulos, M. G. Nicholas and B. Drevet, Wettability at high temperatures, Elsevier, (1999).

[113] F. Delannay, L. Froyen and A. Deruyttere, The wetting of solids by molten metals and its relation to the preparation of metal-matrix composites composites, J Mater Sci **22**, 1-16 (1987).

[114] B. Gallois, Wetting in nonreactive liquid metal-oxide systems, Jom-Us **49**, 48-51 (1997).

[115] A. Bellosi, T. Kosmac and A. P. Tomsia, Interfacial science in ceramic joining, Springer Science & Business Media, 2013).

[116] N. Sobczak, J. Sobczak, R. Asthana and R. Purgert, The mystery of molten metal, China Foundry **7**, 425-37 (2010).

[117] L. Liggieri and A. Passerone, An automatic technique for measuring the surface tension of liquid metals, High Temp Technol **7**, 80-6 (1989).

[118] A. Kalantarian, R. David, J. Chen and A. Neumann, Simultaneous measurement of contact angle and surface tension using axisymmetric drop-shape analysis-no apex (ADSA-NA), Langmuir **27**, 3485-95 (2011).

[119] J. Li, Kinetics of wetting and spreading of Cu-Ti alloys on alumina and glassy carbon substrates, J Mater Sci Lett **11**, 1551-4 (1992).

[120] M. Muolo, E. Ferrera, R. Novakovic and A. Passerone, Wettability of zirconium diboride ceramics by Ag, Cu and their alloys with Zr, Scripta Mater **48**, 191-6 (2003).

[121] N. Eustathopoulos, N. Sobczak, A. Passerone and K. Nogi, Measurement of contact angle and work of adhesion at high temperature, J Mater Sci **40**, 2271-80 (2005).

[122] R. N. Wenzel, Resistance of solid surfaces to wetting by water, Ind Eng Chem **28**, 988-94 (1936).

[123] E. Saiz, A. Tomsia and R. Cannon, Ridging effects on wetting and spreading of liquids on solids, Acta Mater **46**, 2349-61 (1998).

[124] W. W. Mullins, The effect of thermal grooving on grain boundary motion, Acta Metall **6**,

414-27 (1958).

[125] A. Cassie and S. Baxter, Wettability of porous surfaces, Trans Faraday Soc **40**, 546-51 (1944).

[126] M. Entezarian and R. Drew, Direct bonding of copper to aluminum nitride, Mater Sci Eng A **212**, 206-12 (1996).

[127] N. Sobczak, J. Sobczak, Z. Gorny, M. Ksiazek and W. Radziwill. Interaction at the liquid/ceramic interfaces as a factor affecting the formation of multimaterials. State Scientific Commitee of Poland, Cracow, Poland, (1995). Report No.: 7.7372.92.03.

[128] N. Sobczak, J. Sobczak, M. Ksiazek, W. Radziwill, P. Robatgi, T. Bm and S. Seal. Complex investigations of the interfacial phenomena of the liquid metals in contact with solid bodies. Polish-American Joint Fund named M. Sklodowska-Curie, (1995). Report No.: MPINIST-92-90.

[129] L. Xi, I. Kaban, R. Nowak, B. Korpała, G. Bruzda, N. Sobczak, N. Mattern and J. Eckert, High-temperature wetting and interfacial interaction between liquid Al and TiB_2 ceramic, J Mater Sci **50**, 2682-90 (2015).

[130] N. Sobczak, M. Singh and R. Asthana, High-temperature wettability measurements in metal/ceramic systems–Some methodological issues, Curr Opin Solid State Mater Sci **9**, 241-53 (2005).

[131] J. D. Bernardin, I. Mudawar, C. B. Walsh and E. I. Franses, Contact angle temperature dependence for water droplets on practical aluminum surfaces, Int J Heat Mass Transfer **40**, 1017-33 (1997).

[132] A. Marmur, Equilibrium contact angles: Theory and measurement, Colloid Surf A **116**, 55-61 (1996).

[133] S. G. Kandlikar and M. E. Steinke, Contact angles and interface behavior during rapid evaporation of liquid on a heated surface, Int J Heat Mass Transfer **45**, 3771-80 (2002).

[134] E. Saiz, M. Benhassine, J. De Coninck and A. Tomsia, Early stages of dissolutive spreading, Scripta Mater **62**, 934-8 (2010).

[135] N. Eustathopoulos and R. Voytovych, The role of reactivity in wetting by liquid metals: a review, J Mater Sci **51**, 425-37 (2016).

[136] K. Landry and N. Eustathopoulos, Dynamics of wetting in reactive metal/ceramic systems: linear spreading, Acta Mater **44**, 3923-32 (1996).

[137] N. Eustathopoulos, Dynamics of wetting in reactive metal/ceramic systems, Acta Mater **46**, 2319-27 (1998).

[138] R. Voytovych, A. Koltsov, F. Hodaj and N. Eustathopoulos, Reactive vs non-reactive wetting of ZrB_2 by azeotropic Au–Ni, Acta Mater **55**, 6316-21 (2007).

[139] A. Passerone, M. L. Muolo, F. Valenza, F. Monteverde and N. Sobczak, Wetting and interfacial phenomena in Ni–HfB_2 systems, Acta Mater **57**, 356-64 (2009).

[140] J. A. Warren, W. Boettinger and A. Roosen, Modeling reactive wetting, Acta Mater **46**, 3247-64 (1998).

[141] N. Eustathopoulos, Progress in understanding and modeling reactive wetting of metals on ceramics, Curr Opin Solid State Mater Sci **9**, 152-60 (2005).

[142] O. Dezellus, S. Jacques, F. Hodaj and N. Eustathopoulos, Wetting and infiltration of carbon by liquid silicon, J Mater Sci **40**, 2307-11 (2005).

[143] S. Kalogeropoulou, C. Rado and N. Eustathopoulos, Mechanisms of reactive wetting: The wetting to non-wetting case, Scripta Mater **41**, 723-8 (1999).

[144] K. Landry, C. Rado, R. Voitovich and N. Eustathopoulos, Mechanisms of reactive wetting: the question of triple line configuration, Acta Mater **45**, 3079-85 (1997).

[145] Y. Plevachuk, I. Egry, J. Brillo, D. Holland-Moritz and I. Kaban, Density and atomic volume in liquid Al–Fe and Al–Ni binary alloys, Int J Mater Res **98**, 107-11 (2007).

[146] P. D. Desai, Thermodynamic properties of selected binary aluminum alloy systems, J Phys Chem Ref Data **16**, 109-24 (1987).

[147] V. T. Witusiewicz, A. A. Bondar, U. Hecht, S. Rex and T. Y. Velikanova, The Al–B–Nb–Ti system: III. Thermodynamic re-evaluation of the constituent binary system Al–Ti, J Alloys Compd **465**, 64-77 (2008).

[148] F. Cardarelli, Materials handbook: a concise desktop reference, Springer Science & Business Media, (2013).

[149] W. Huang and Y. Chang, A thermodynamic analysis of the NiAl system, Intermetallics **6**, 487-98 (1998).

[150] M. Köhler, Aufbau und Erprobung eines Messplatzes zur Untersuchung der Oberflächenspannung flüssiger Metalllegierungen nach der Methode des liegenden Tropfens. Chemnitz University of Technology, Chemnitz, Germany, Diploma thesis, (2008).

[151] N. Sobczak, R. Nowak, W. Radziwill, J. Budzioch and A. Glenz, Experimental complex

for investigations of high temperature capillarity phenomena, Mater Sci Eng A **495**, 43-9 (2008).

[152] B. Cullity, Elements of X-ray diffraction, Massachusetts, Addison-Wesley, (1978).

[153] T. Degen, M. Sadki, E. Bron, U. König and G. Nénert, The HighScore suite, Powder Diffr **29**, S13-S8 (2014).

[154] PDF-4+ database, International Centre for Diffraction Data, Newtown Square, PA, USA (2014).

[155] H. Cichy and E. Fromm, Oxidation kinetics of metal films at 300 K studied by the piezoelectric quartz crystal microbalance technique, Thin Solid Films **195**, 147-58 (1991).

[156] M. Martin and E. Fromm, Kinetics of aluminium film oxidation measured by a modified quartz crystal microbalance, Thin Solid Films **236**, 199-203 (1993).

[157] L. Coudurier, J. Adorian, D. Pique and N. Eustathopoulos, Etude de la mouillabilité par l'aluminium liquide de l'alumine et de l'alumine recouverte d'une couche de métal ou de composé réfractaire, Revue internationale des hautes températures et des réfractaires **21**, 81-93 (1984).

[158] W. Hehn and E. Fromm, Anfangsstadium der Oxidation von Alumini-umschmelzen bei Drücken unterhalb von 10− 6 bar, Aluminium **64**, 180-5 (1988).

[159] Y. H. Koh, S. Y. Lee and H. E. Kim, Oxidation behavior of titanium boride at elevated temperatures, J Am Ceram Soc **84**, 239-41 (2001).

[160] S. Avraham and W. Kaplan, Reactive wetting of rutile by liquid aluminium, J Mater Sci **40**, 1093-100 (2005).

[161] N. Sobczak, L. Stobierski, W. Radziwill, M. Ksiazek and M. Warmuzek, Wettability and interfacial reactions in Al/TiO_2, Surf Interface Anal **36**, 1067-70 (2004).

[162] C. Feng and L. Froyen, Formation of Al_3Ti and Al_2O_3 from an Al–TiO_2 system for preparing in-situ aluminium matrix composites, Composites Part A: Applied Science and Manufacturing **31**, 385-90 (2000).

[163] I. Gheorghe and H. Rack, Reactive infiltration of 25 vol pct TiO_2/Al composites, Metall Mater Trans A **33**, 2155-62 (2002).

[164] L. Dake and R. Lad, Electronic and chemical interactions at aluminum/TiO_2 (110) interfaces, Surf Sci **289**, 297-306 (1993).

[165] I. Gotman, M. Koczak and E. Shtessel, Fabrication of Al matrix in situ composites via self-propagating synthesis, Mater Sci Eng A **187**, 189-99 (1994).

[166] N. Frage, M. Polak, M. Dariel, N. Frumin and L. Levin, High-temperature phase

equilibria in the Al-rich corner of the Al-Ti-C system, Metall Mater Trans A **29**, 1341-5 (1998).

[167] N. Froumin, N. Frage, M. Polak and M. Dariel, Wettability and phase formation in the TiC_x/Al systems, Scripta Mater **37**, 1263-6 (1997).

[168] L. Xi, I. Kaban, R. Nowak, G. Bruzda, N. Sobczak and J. Eckert, Interfacial interactions between liquid Ti–Al alloys and TiB_2 ceramic, J Mater Sci **51**, 1779-87 (2016).

[169] R. Boyer, Materials properties handbook: titanium alloys, **3**, 1-55 (1994).

[170] Y.-W. Kim, Gamma titanium aluminides: their status and future, Jom-Us **47**, 39-42 (1995).

[171] R. Boyer, An overview on the use of titanium in the aerospace industry, Mater Sci Eng A **213**, 103-14 (1996).

[172] R. Schutz and H. Watkins, Recent developments in titanium alloy application in the energy industry, Mater Sci Eng A **243**, 305-15 (1998).

[173] P. A. Bartolotta and D. L. Krause, Titanium aluminide applications in the high speed civil transport, (1999).

[174] T. Tetsui, Gamma Ti aluminides for non-aerospace applications, Curr Opin Solid State Mater Sci **4**, 243-8 (1999).

[175] R.E. Schafrik. A perspective on intermetallic commercialization for aero-turbine applications. In: K. J. Hemker, D. M. Dimiduk, H. Clemens, R. Darolia, H. Inui, J. M. Larsen, et al., eds. Structural Intermetallics 2001, Proceedings of the 3rd International Symposium on Structural Intermetallics 2001, p. 13-7.

[176] S. Djanarthany, J.-C. Viala and J. Bouix, An overview of monolithic titanium aluminides based on Ti_3Al and TiAl, Mater Chem Phys **72**, 301-19 (2001).

[177] M. Thomas and M. P. Bacos, Processing and characterization of TiAl-based alloys: towards an industrial scale, J Aerospace Lab **3**, 1-11 (2011).

[178] D. Chandley, Use of gamma titanium aluminide for automotive engine valves, Metall Sci Tecnol **18**, 8-11 (2000).

[179] C. Leyens and M. Peters, Titanium and titanium alloys, Wiley Online Library, (2003).

[180] B. Cherukuri, R. Srinivasan, S. Tamirisakandala and D. B. Miracle, The influence of trace boron addition on grain growth kinetics of the beta phase in the beta titanium alloy Ti–15Mo–2.6 Nb–3Al–0.2Si, Scripta Mater **60**, 496-9 (2009).

[181] Y.-W. Kim, Ordered intermetallic alloys, part III: Gamma titanium aluminides, Jom-Us

46, 30-9 (1994).

[182] F. Froes, C. Suryanarayana and D. Eliezer, Synthesis, properties and applications of titanium aluminides, J Mater Sci **27**, 5113-40 (1992).

[183] J. Doychak, Metal-and intermetallic-matrix composites for aerospace propulsion and power systems, Jom-Us **44**, 46-51 (1992).

[184] P. Schumacher, A. Greer, J. Worth, P. Evans, M. Kearns, P. Fisher and A. Green, New studies of nucleation mechanisms in aluminium alloys: Implications for grain refinement practice, Mater Sci Technol **14**, 394-404 (1998).

[185] A. Kartavykh, M. Gorshenkov, V. Tcherdyntsev and D. Podgorny, On the state of boride precipitates in grain refined TiAl-based alloys with high Nb content, J Alloys Compd **586**, S153-S8 (2014).

[186] T. Quested and A. Greer, The effect of the size distribution of inoculant particles on as-cast grain size in aluminium alloys, Acta Mater **52**, 3859-68 (2004).

[187] L. Lu, M. Lai and H. Wang, Synthesis of titanium diboride TiB_2 and Ti-Al-B metal matrix composites, J Mater Sci **35**, 241-8 (2000).

[188] N. Thadhani, N. Chawla and W. Kibbe, Explosive shock-compression processing of titanium aluminide/titanium diboride composites, J Mater Sci **26**, 232-40 (1991).

[189] A. Liu, B. Li, H. Nan, Y. Sui, J. Guo and H. Fu, Interaction between γ-TiAl alloy and zirconia, China Foundry **5**, 44-46 (2008).

[190] Q. Jia, Y. Cui and R. Yang, Intensified interfacial reactions between gamma titanium aluminide and CaO stabilised ZrO_2, Int J Cast Met Res **17**, 23-8 (2004).

[191] B. Li, A. Liu, N. Hai, W.-S. Bi, J. Guo and H. Fu, Wettability of TiAl alloy melt on ceramic moulds in electromagnetic field, Trans Nonferrous Met Soc China **18**, 518-22 (2008).

[192] N. Sobczak, Effects of titanium on wettability and interfaces in aluminum/ceramic systems, Characterization and Control of Interfaces for High Quality Advanced Materials: Proceedings of the International Conference on ICCCI 2003, Kurashiki, Japan, 2003, Ceramic Transactions, John Wiley & Sons, p. 83-91.

[193] N. Sobczak, R. Nowak, A. Passerone, F. Valenza, M. L. Muolo, L. Jaworska, F. Barberis and M. Capurro, Wetting and joining of HfB_2 and Ta with Ni, Prace Instytutu Odlewnictwa **50**, 5-14 (2010).

[194] J. Murray, P. Liao and K. Spear, The B−Ti (Boron-Titanium) system, Bull alloy phase

diagr **7**, 550-5 (1986).

[195] G. Cacciamani, P. Riani and F. Valenza, Equilibrium between MB2 (M= Ti, Zr, Hf) UHTC and Ni: A thermodynamic database for the B–Hf–Ni–Ti–Zr system, Calphad **35**, 601-19 (2011).

[196] Z. Fan, Z. Guo and B. Cantor, The kinetics and mechanism of interfacial reaction in sigma fibre-reinforced Ti MMCs, Composites Part A: Applied Science and Manufacturing **28**, 131-40 (1997).

[197] K. Panda and K. R. Chandran, Synthesis of ductile titanium-titanium boride (Ti-TiB) composites with a beta-titanium matrix: The nature of TiB formation and composite properties, Metall Mater Trans A **34**, 1371-85 (2003).

[198] Ceramic/metal bonding, In: Y.N. Zhou, ed. Microjoining and nanojoining, Cambridge, England, Woodhead publishing, (2008).

[199] V. Cazajus, S. Seguy, H. Welemane and M. Karama, Residual stresses in a ceramic-metal composite, Applied Mechanics and Materials, Trans Tech Publ, p. 185-96.

[200] Titanium alloy guide. RMI Titanium Company, An RTI International Metals, Inc. Company. Niles, OH, USA, (2000).

[201] R. E. Schafrik, Dynamic elastic moduli of the titanium aluminides, Metall Mater Trans A **8**, 1003-6 (1977).

[202] Y. N. Berdovsky, Intermetallics research progress, Nova Publishers, (2008).

[203] W. Frazier and M. Koczak. Ambient temperature properties of PM aluminum-titanium alloys. Naval Air Development Center, Warminster, PA, USA; 1988.

[204] NPCS Board of Consultants & Engineers. The complete technology book on aluminium and aluminium products, Asia Pacific Business Press Inc., Delhi, India, (2007).

[205] M. Bauccio, ASM Engineered materials reference book, 2nd ed., ASM International, Materials Park, OH, (1994).

[206] A. K. Misra, Theoretical analysis of compatibility of several reinforcement materials with NiAl and FeAl matrices, NASA Contractor Report **1**, 1-20 (1989).

[207] J. T. Guo and Z. P. Xing, Investigation of NiAl–TiB_2 in situ composites, J Mater Res **12**, 1083-90 (1997).

[208] L. Zhou and J. Guo, Preliminary investigation of NiAl-TiB_2 composite prepared by reaction milling, J Mater Sci Technol **15** 427-30 (1999).

[209] S. Deevi and V. Sikka, Nickel and iron aluminides: An overview on properties, processing, and applications, Intermetallics **4**, 357-75 (1996).

[210] D. B. Miracle and R. Darolia, NiAl and its alloys, Intermetallic compounds **2**, 53-72 (1994).

[211] T. Iida and R. I. Guthrie, The physical properties of liquid metals, Clarendon Press, Walton Street, Oxford OX 26 DP, UK, (1988).

[212] V. I. Dybkov. An introduction to interfacial reaction kinetics. Amazon Kindle Direct Publishing 2016.

[213] P. Li, Y. Wu and X. Liu, Controlled synthesis of different morphologies of TiB_2 microcrystals by aluminum melt reaction method, Mater Res Bull **48**, 2044-8 (2013).

[214] Ľ. Bača and N. Stelzer, Adapting of sol–gel process for preparation of TiB_2 powder from low-cost precursors, J Eur Ceram Soc **28**, 907-11 (2008).

[215] D. P. Sekulic, Wetting and spreading of liquid metals through open microgrooves and surface alterations, Heat Transfer Eng **32**, 648-57 (2011).

[216] C. Lau, A. Mukasyan, A. Pelekh and A. Varma, Mechanistic studies in combustion synthesis of NiAl–TiB_2 composites: Effects of gravity, J Mater Res **16**, 1614-25 (2001).

[217] M. W. Barsoum and B. Houng, Transient plastic phase processing of titanium–boron–carbon composites, J Am Ceram Soc **76**, 1445-51 (1993).

[218] L. Contreras, X. Turrillas, G. Vaughan, Å. Kvick and M. Rodrıguez, Time-resolved XRD study of TiC–TiB_2 composites obtained by SHS, Acta Mater **52**, 4783-90 (2004).

[219] L. Klinger, I. Gotman and D. Horvitz, In situ processing of TiB_2/TiC ceramic composites by thermal explosion under pressure: experimental study and modeling, Mater Sci Eng A **302**, 92-9 (2001).

[220] G. Vinod Kumar, B. Murty and M. Chakraborty, Development of Al–Ti–C grain refiners and study of their grain refining efficiency on Al and Al–7Si alloy, J Alloys Compd **396**, 143-50 (2005).

[221] C. Sorrell, H. Beratan, R. Bradt and V. Stubican, Directional Solidification of (Ti, Zr) Carbide-(Ti, Zr) Diboride Eutectics, J Am Ceram Soc **67**, 190-4 (1984).

[222] W. Lengauer, Transition metal carbides, nitrides, and carbonitrides, Handbook of ceramic hard materials 202-52 (2000).

[223] A. Taylor and R. W. Floyd, The constitution of nickel-rich alloys of the nickel-chromium-

aluminum system, J Inst Met **81**, 451-64 (1952).

[224] F. Valenza, C. Artini, A. Passerone, P. Cirillo and M. Muolo, Joining of ZrB_2 ceramics to Ti6Al4V by Ni-based interlayers, J Mater Eng Perform **23**, 1555-60 (2014).

[225] M. Muolo, F. Valenza, N. Sobczak and A. Passerone, Overview on wetting and joining in transition metals diborides, Adv Scie Technol **64**, 98-107 (2010).

[226] F. Valenza, M. Muolo, A. Passerone, G. Cacciamani and C. Artini, Control of interfacial reactivity between ZrB_2 and Ni-based brazing alloys, J Mater Eng Perform **21**, 660-6 (2012).

[227] A. Passerone, M. Muolo, F. Valenza and L. Kaufman, Wettability of HfB_2 by molten Ni (B) alloys interpreted by CALPHAD methods, Part 2: Wetting and interfacial reactivity, Calphad **34**, 6-14 (2010).

[228] C. Artini, M. Muolo, A. Passerone, G. Cacciamani and F. Valenza, Isothermal solid–liquid transitions in the (Ni, B)/ZrB_2 system as revealed by sessile drop experiments, J Mater Sci **48**, 5029-35 (2013).

[229] L. Xi, I. Kaban, R. Nowak, G. Bruzda, N. Sobczak, M. Stoica and J. Eckert, Investigation of Ni-B Alloys for Joining of TiB_2 Ultra-High-Temperature Ceramic, J Mater Eng Perform **25**, 3204–10 (2016).

Acknowledgement

I would like to express my gratitude to all of them who helped me during my PhD study. Without their support, I would not have been able to accomplish the doctoral dissertation. First and foremost, I would like to express my deep gratitude to Prof. Dr.- Ing. habil. Dr. h.c. J. Eckert for providing the invaluable opportunity to do my PhD work at the Leibnitz Institute for Solid State and Materials Research Dresden (IFW Dresden). I also express my sincere thanks for encouraging me to present my work at scientific conferences and workshops.

I equally express my sincere gratitude to my research supervisor Dr. I. Kaban who always gives me constant supports and valuable suggestions. I also would like to express my special thanks to his immense patience on me throughout the past four years. I also would like to express my special thanks to Prof. Dr. Sci. N. Sobczak and her team for a great collaboration and for providing the opportunity to carry out the sessile drop experiments at the Center for High Temperature Studies at the Foundry Research Institute Cracow in Poland. I would like to express my great thanks to her patient supervision and constant support and advice of my experiments, research papers and dissertation. Otherwise, I would have never progressed smoothly without the help.

I express my sincere thanks to all the colleagues from the Institute for Complex Materials at the IFW Dresden, especially to Dr. N. Mattern, Assoc. Prof. M. Stoica, Dr. O. Shuleshova, Dr. Matthias Bönisch, Dr. K.G. Prashanth, Prof. J. He, Dr. J. Han, B. Präßler-Wüstling for their great support. I also equally give my thanks to Dr. H. Wendrock, Dr. S. Oswald, Assoc. Prof. K. Song, S. Donath, M. Frey, B. Bartusch, B. Opitz, A. Funk, Dr. N. Zheng, Dr. P. Ma, Dr. G. Ma, Dr. L. Zhang, M. Li for their technical support. I express my sincere gratitude to all the colleagues, who patiently responded without any reservations to my questionnaire during the overall work. I also would like to give great thanks to Dr. R. Nowak, Dr. A. Kudyba, G. Bruzda and B. Korpała from Foundry Research Institute (Cracow, Poland) for their technical support and advices during the sessile drop experiments.

Thanks to my office colleagues P. Ramasamy, H. Weber, P. Wang, Dr. S. Bera for providing the friendly atmosphere to my dissertation.

I also give my thanks to my friends in Dresden, Dr. W. Si, Dr. Y. Jia, X. Sun, Y. Fu, K. Deng, B. Yin, J. Zhang, Dr. S. Feng, Y. Liu, Y. Sui, H. Li, L. Deng, J. Wang, Assoc. Prof. S. Wang. Thank you very much for your support and much fun about the life in Germany. My special thanks for your help, encouragement and memory in the past four years.

I express my great thanks to the financial support by Chinese Scholarship Council (CSC).

Last but not least, I would like to give my special thanks to my parents and my sisters for their great support and encouragement. The completion of this long journey would have been impossible without your support for my daily life.

Lixia Xi

03.11.2016

Erklärung

Hiermit versichere ich, dass ich die vorliegende Arbeit ohne die unzulässige Hilfe Dritter und ohne Benutzung anderer als der angegebenen Hilfsmittel angefertigt habe. Die aus fremden Quellen direkt oder indirekt übernommenen Gedanken sind als solche kenntlich gemacht. Bei der Auswahl und Auswertung des Materials sowie bei der Herstellung des Manuskripts habe ich Unterstützungsleistungen von folgenden Personen erhalten: Prof. Dr. J. Eckert und Dr. I. Kaban. Weitere Personen waren an der geistigen Herstellung der vorliegenden Arbeit nicht beteiligt. Insbesondere habe ich nicht die Hilfe eines kommerziellen Promotionsberaters in Anspruch genommen. Dritte haben von mir keine geldwerten Leistungen für Arbeiten erhalten, die in Zusammenhang mit dem Inhalt der vorgelegten Dissertation stehen. Die Arbeit wurde bisher weder im Inland noch im Ausland in gleicher oder ähnlicher Form einer anderen Prüfungsbehörde vorgelegt und ist auch noch nicht veröffentlicht worden. Die vorliegende Dissertation wurde an der TU Dresden am Institut für Werkstoffwissenschaft der Fakultät Maschinenwesen unter der wissenschaftlichen Betreuung durch Prof. Dr.-Ing. habil. Dr. h.c. Jürgen Eckert angefertigt. Die Promotionsordnung der Fakultät Maschinenwesen der TU Dresden aus dem Jahre 2001 erkenne ich an.

.....

Lixia Xi

Dresden, 14.03.2017